

[Click here to view linked References](#)

1  
2  
3  
4  
5  
6  
7  
8  
9  
10  
11  
12  
13  
14  
15  
16  
17  
18  
19  
20  
21  
22  
23  
24  
25  
26  
27  
28  
29  
30  
31  
32  
33  
34  
35  
36  
37  
38  
39  
40  
41  
42  
43  
44  
45  
46  
47  
48  
49  
50  
51  
52  
53  
54  
55  
56  
57  
58  
59  
60  
61  
62  
63  
64  
65

1 **Redox state of the Dharwar craton root as inferred from eclogite and peridotite**  
2 **sourced mantle cargo, with implications for kimberlite and lamproite magma**  
3 **formation**

4  
5 Azhar M. Shaikh<sup>1,2,3</sup>\*, Yannick Bussweiler<sup>4</sup>, Fanus Viljoen<sup>2</sup>, Robert Bolhar<sup>3</sup>, S. Ravi<sup>5</sup>, Dominik  
6 C. Hezel<sup>6</sup>, Henriëtte Ueckermann<sup>2</sup>, Sebastian Tappe<sup>2,7</sup>

7  
8  
9 <sup>1</sup> Department of Earth and Environmental Sciences, Indian Institute of Science Education and  
10 Research Berhampur, India

11 <sup>2</sup> Department of Geology, University of Johannesburg, Auckland Park, South Africa

12 <sup>3</sup> School of Geosciences, University of the Witwatersrand, Braamfontein, South Africa

13 <sup>4</sup> Institute for Geology and Mineralogy, University of Cologne, Germany

14 <sup>5</sup> Geological Survey of India, Bengaluru, India

15 <sup>6</sup> Institut für Geowissenschaften, Goethe-Universität Frankfurt, Frankfurt am Main, Germany

16 <sup>7</sup> Department of Geosciences, UiT The Arctic University of Norway, Tromsø, Norway

17  
18 \*Corresponding author: Telephone: +918879524349.

19 E-mail: [azharms@iiserbpr.ac.in](mailto:azharms@iiserbpr.ac.in), ORCID ID: [0000-0002-7327-5414](https://orcid.org/0000-0002-7327-5414)

20  
21 **ABSTRACT**

22 Despite over 400 occurrences of kimberlites and related rocks in India, mantle-derived xenoliths  
23 are known only from a few occurrences. This paucity of mantle-derived xenoliths in Indian

1  
2  
3  
4  
5  
6  
7  
8  
9  
10  
11  
12  
13  
14  
15  
16  
17  
18  
19  
20  
21  
22  
23  
24  
25  
26  
27  
28  
29  
30  
31  
32  
33  
34  
35  
36  
37  
38  
39  
40  
41  
42  
43  
44  
45  
46  
47  
48  
49  
50  
51  
52  
53  
54  
55  
56  
57  
58  
59  
60  
61  
62  
63  
64  
65

kimberlites has hampered investigations of the subcontinental lithospheric mantle (SCLM). Using a valuable selection of the rare xenolith inventory, we here report  $Fe^{3+}/\Sigma Fe$  measurements for garnets using the electron microprobe (EPMA) flank method, targeting six mantle eclogite xenoliths (KL2 pipe) and fourteen peridotitic garnet xenocrysts (P9 and P10 hypabyssal intrusions) from the Wajrakarur kimberlite field (WKF) on the Eastern Dharwar craton (EDC). These data provide some of the first direct constraints on the oxygen fugacity ( $fO_2$ ) of the lithospheric mantle beneath the Indian subcontinent.

The measured  $Fe^{3+}/\Sigma Fe$  ratios vary between 0.02 and 0.05 ( $\pm 0.01$ ) for the eclogite xenoliths and between 0.02 and 0.10 ( $\pm 0.01$ ) for the peridotitic garnets. Calculated  $\Delta \log fO_2$  values for the KL2 eclogites show a wide range from FMQ-3.9 to FMQ-0.9 ( $\pm 0.6$ ), straddling the boundary between the diamond and carbonate stability fields. In terms of redox compositions, it appears that the KL2 eclogites are able to host diamond, which is consistent with the diamondiferous nature of this particular WKF locality and the presence of eclogitic garnet inclusions in diamonds from the nearby TK4 kimberlite body.

The peridotitic garnet xenocrysts from the P9 and P10 kimberlite bodies, which were entrained between ~125 and 170 km depth, reveal  $\Delta \log fO_2$  values between FMQ-4.5 and FMQ-2.6 ( $\pm 0.9$ ). Garnet xenocrysts with 'normal' REE patterns exhibit higher  $Fe^{3+}/\Sigma Fe$  ratios compared to garnets with 'sinusoidal' REE patterns. Importantly, the  $Fe^{3+}/\Sigma Fe$  ratios of garnet xenocrysts with 'normal' REE patterns (~125–160 km depth) correlate with metasomatic Ti-Y-Zr-V enrichment, which suggests metasomatism-driven oxidation of the cratonic mantle at mid-lithospheric depths. Such melt-related mantle metasomatism was probably diamond-destructive within the otherwise diamond-fertile lithospheric keel.

1  
2  
3  
4  
5  
6  
7  
8  
9  
10  
11  
12  
13  
14  
15  
16  
17  
18  
19  
20  
21  
22  
23  
24  
25  
26  
27  
28  
29  
30  
31  
32  
33  
34  
35  
36  
37  
38  
39  
40  
41  
42  
43  
44  
45  
46  
47  
48  
49  
50  
51  
52  
53  
54  
55  
56  
57  
58  
59  
60  
61  
62  
63  
64  
65

46           The observed wide range of  $\Delta\log fO_2$  values for the Dharwar cratonic mantle lithosphere  
47 allows for stabilization of various metasomatic phases (e.g., amphiboles, micas, carbonates) that  
48 may have formed (or concentrated in) distinctly different metasome assemblages within the  
49 continental root that underpins Peninsular India. Changing the relative contributions from such  
50 highly diverse volatile-rich metasomes may explain the spatiotemporal association of kimberlites  
51 and various diamond-bearing potassic magma types such as orangeites, ultramafic lamprophyres  
52 and lamproites, a scenario that is influenced by the redox composition of the Dharwar craton root.

53  
54 *Keywords: Continental lithospheric mantle, Eclogite, Garnet, Oxygen fugacity, Mantle redox,*  
55 *Wajrakarur kimberlites, Southern India*

57 **Introduction**

58 Oxygen fugacity ( $fO_2$ ) has significant implications for the speciation of CHONS-volatiles and the  
59 stability of diamond/graphite in the Earth's mantle (Stagno, 2019). Oxygen fugacity also  
60 influences (i) melting and metasomatism of mantle rocks, thereby influencing fluxes of various  
61 magma types, and (ii) recycling of volatiles, thereby affecting global volatile cycles (Yaxley et al.,  
62 2017). Therefore, understanding  $fO_2$  in Earth's mantle is crucial for comprehending terrestrial  
63 magmatism and volatile cycles (Foley, 2011; Tappe et al., 2018). The  $fO_2$  compositions of the  
64 subcontinental lithospheric mantle (SCLM) have been shown to vary with depth and time  
65 (Woodland and Koch, 2003; Creighton et al., 2009, 2010; Yaxley et al., 2017; Tappe et al., 2021;  
Aulbach et al., 2022), which has the potential to shift melting regimes over geological timescales  
(Foley, 2011). The  $fO_2$  values can be estimated for mantle-derived peridotite (Ballhaus et al., 1991;

1  
2  
3  
4 68 Stagno et al., 2013) and eclogite (Stagno et al., 2015) xenoliths by measuring the  $\text{Fe}^{3+}/\Sigma\text{Fe}$  ratios  
5  
6  
7 69 of their constituting garnet fractions.  
8

9 70 This contribution presents the first measurements of  $\text{Fe}^{3+}/\Sigma\text{Fe}$  in garnets from six eclogite  
10  
11 71 xenoliths from the KL2 hypabyssal intrusion and fourteen peridotitic garnet xenocrysts from the  
12  
13  
14 72 P9 and P10 intrusions of the Wajrakarur Kimberlite Field (WKF) located on the Eastern Dharwar  
15  
16 73 craton (EDC) in southern India. We aim to constrain the redox state of the regional SCLM that  
17  
18  
19 74 underpinned Peninsular India at ca. 1.1 Ga. The KL2 intrusion forms part of the Kalyandurga  
20  
21 75 cluster, which consists of seven minor kimberlite intrusions (KL1 to KL7) and is located in the  
22  
23  
24 76 southern part of the WKF (Fig. 1). The P9 and P10 minor intrusions form part of the Wajrakarur-  
25  
26 77 Lattavaram cluster, situated in the north. Shaikh et al. (2020) constrained the architecture and  
27  
28  
29 78 thermal state of the regional SCLM using major and trace element compositions of garnets from  
30  
31 79 P9 and P10, some of which were re-analyzed here for their  $\text{Fe}^{3+}/\Sigma\text{Fe}$  compositions. According to  
32  
33  
34 80 Shaikh et al. (2020), lithospheric thinning beneath the Dharwar craton, from ~190 km depth at 1.1  
35  
36 81 Ga to ~120 km depth at present, was aided by extensive melt metasomatism at the bottom of the  
37  
38 82 SCLM.  
39  
40

41 83 The ca. 1.1 Ga Kalyandurga kimberlites are special in several ways. For instance, (i) the  
42  
43 84 diamondiferous KL2 minor intrusion is distinguished by an overabundance of eclogite xenoliths  
44  
45 85 (>95% of the mantle xenolith population are eclogite nodules: Rao et al., 2001; Neelakantam,  
46  
47  
48 86 2001; Patel et al., 2006); (ii) the KL4 minor intrusion exhibits an exceptional abundance of mantle-  
49  
50  
51 87 derived ilmenite macrocrysts (Sastry et al., 2005); (iii) the Kalyandurga kimberlites intruded the  
52  
53 88 2.6–2.5 Ga Closepet granite in close proximity to the Chitradurga Boundary Fault, which presents  
54  
55  
56 89 an important structure for the understanding of the evolution of the Dharwar craton (e.g., Chadwick  
57  
58 90 et al., 2000). KL2 eclogite nodules have previously been investigated for petrography, in-situ  
59  
60  
61  
62  
63  
64  
65

1  
2  
3  
4  
5  
6  
7  
8  
9  
10  
11  
12  
13  
14  
15  
16  
17  
18  
19  
20  
21  
22  
23  
24  
25  
26  
27  
28  
29  
30  
31  
32  
33  
34  
35  
36  
37  
38  
39  
40  
41  
42  
43  
44  
45  
46  
47  
48  
49  
50  
51  
52  
53  
54  
55  
56  
57  
58  
59  
60  
61  
62  
63  
64  
65

91 mineral major and trace element contents, and oxygen isotopic compositions to constrain their  
92 origins (Ganguly and Bhattacharya, 1987; Rao et al., 2001; Patel et al., 2006, 2009; Griffin et al.,  
93 2009; Dongre et al., 2015). Four eclogite xenoliths were examined by Ganguly and Bhattacharya  
94 (1987), while two eclogite nodules were examined by Rao et al. (2001) to determine mineral major  
95 element compositions. The first detailed petrographic observations and mineral major element data  
96 for a suite of eleven KL2 eclogite xenoliths were provided by Patel et al. (2006). In order to review  
97 the P-T conditions and origins of eclogites and pyroxenites from the WKF, Patel et al. (2009)  
98 combined published xenolith data with nine newly analyzed xenoliths and argued against the  
99 involvement of subducted ancient oceanic crust in the formation of KL2 eclogites. These authors  
100 used textural and mineral compositional evidence to support a magmatic cumulate origin for the  
101 KL2 eclogites. Babu et al. (2008) presented a much larger eclogite dataset (35 xenoliths) at the 9<sup>th</sup>  
102 International Kimberlite Conference, and Griffin et al. (2009) utilized these results to argue that  
103 this eclogite xenolith suite originated from mafic melts that ponded and crystallized at lithospheric  
104 mantle depths. Mineral major and trace element compositions, as well as the lateral distribution of  
105 mantle-derived xenoliths and xenocrysts, were used to support this interpretation (Griffin et al.,  
106 2009). In opposition to this notion, Dongre et al. (2015) examined 28 KL2 eclogite xenoliths and  
107 reported the first  $\delta^{18}\text{O}$  data (+5.3 to +7.8‰), which are best explained by a subduction-recycling  
108 model. Recently, a few more KL2 eclogite nodules were studied by Chatterjee et al. (2023)  
109 supporting the subduction model. However, no attempt has been made so far to use the eclogites  
110 and other mantle-derived materials to determine the oxidation state of the SCLM beneath southern  
111 India.

112           Herein, we apply the calibration of Stagno et al. (2015), which estimates eclogite  $f\text{O}_2$  using  
113 the major element compositions of garnet and clinopyroxene, together with  $\text{Fe}^{3+}/\Sigma\text{Fe}$  ratio

1  
2  
3  
4 114 measurements for garnet, an approach taken in several previous eclogite xenolith studies from  
5  
6 115 cratons worldwide (e.g., Smart et al., 2017, 2021a; Aulbach et al., 2019, 2022; Burness et al., 2020;  
7  
8  
9 116 Mikhailenko et al., 2020). Our garnet  $\text{Fe}^{3+}/\Sigma\text{Fe}$  measurements are complemented by in-situ major  
10  
11 117 and trace element data for garnet crystals from the KL2 eclogites. For peridotitic garnet xenocrysts,  
12  
13  
14 118 we used the calibration of Stagno et al. (2013) and combined garnet  $\text{Fe}^{3+}/\Sigma\text{Fe}$  data with their  
15  
16 119 modeled  $\text{Fe}^{2+}/(\text{Fe}^{2+}+\text{Mg})$  compositions, assuming equilibrium with olivine and orthopyroxene in  
17  
18  
19 120 the original peridotite host rock (O'Neil and Wood, 1979; Harley, 1984; Ryan et al., 1996; Gaul  
20  
21 121 et al., 2000) at estimated equilibrium P-T conditions (Canil et al., 1999). Our results provide the  
22  
23  
24 122 first  $f\text{O}_2$  estimates for eclogites and peridotitic garnets from southern India entrained by ca. 1.1 Ga  
25  
26 123 old Mesoproterozoic kimberlites that represent one of the earliest global emplacement events of  
27  
28  
29 124 diamond-bearing deep-sourced magmas (Tappe et al., 2018).

30  
31 125

## 32 33 126 **Analytical techniques**

34  
35  
36 127 Seven eclogite xenoliths (KL2A to KL2G), measuring 3 to 5 cm in diameter, were collected from  
37  
38  
39 128 the KL2 kimberlite body by S. Ravi. They were cut and polished into a total of 18 standard  
40  
41 129 petrographic thin sections for this study. The eclogite xenoliths are commonly rounded to  
42  
43  
44 130 subrounded (oval) nodules with medium-grained textures. Honey brown pyrope garnet crystals are  
45  
46 131 embedded in a light green to white matrix formed mainly by altered omphacitic clinopyroxene.

47  
48 132 A CAMECA SX100 electron microprobe housed in the Spectrum lab at the University of  
49  
50  
51 133 Johannesburg was used for quantitative in-situ mineral analyses of major and minor elements. The  
52  
53 134 analyses were conducted with a nominal beam size of 1  $\mu\text{m}$ , an accelerating voltage of 20 kV, and  
54  
55  
56 135 a beam current of 20 nA. Trace elements were measured for garnet, clinopyroxene and kyanite in  
57  
58 136 representative eclogite thin sections at the University of Johannesburg using a Thermo Scientific

1  
2  
3  
4  
5  
6  
7  
8  
9  
10  
11  
12  
13  
14  
15  
16  
17  
18  
19  
20  
21  
22  
23  
24  
25  
26  
27  
28  
29  
30  
31  
32  
33  
34  
35  
36  
37  
38  
39  
40  
41  
42  
43  
44  
45  
46  
47  
48  
49  
50  
51  
52  
53  
54  
55  
56  
57  
58  
59  
60  
61  
62  
63  
64  
65

137 iCAP RQ inductively coupled plasma mass spectrometer (ICP-MS) coupled to a 193 nm ArF  
138 RESOLUTION SE155 excimer laser. NIST SRM 612 was used as the calibration reference material,  
139 and  $^{29}\text{Si}$  was used for internal standardization. To verify accuracy of the data, various USGS  
140 basaltic glasses (BCR-2G, BHVO-2, BIR-1G) and the in-house GHR1 megacrystic garnet from  
141 the Monastery kimberlite were analyzed as secondary standards, similar to the setup reported in  
142 Tappe et al. (2023). Data quality is documented in Supp. Table 1. When compared to  
143 recommended values for the USGS glasses and the GHR1 garnet (e.g., Jochum et al., 2016; Tappe  
144 et al., 2021), the majority of trace elements analyzed reproduced with a variance of less than 10 to  
145 15%. To avoid any potential contamination from the host kimberlite during laser ablation, we  
146 rejected ICP-MS trace element measurements with  $>1$  ppm Ba (see Shaikh et al., 2020). The  
147 analytical techniques and data are described in more detail in the Appendix 1 and Supp. Table 1,  
148 respectively. The analytical techniques applied to measure the major and trace element  
149 concentrations for fourteen peridotitic garnet xenocrysts from Wajrakarur kimberlites P9 and P10  
150 are given in Shaikh et al. (2020).

151         The atomic  $\text{Fe}^{3+}/\Sigma\text{Fe}$  proportions in garnet crystals from six eclogite nodules and fourteen  
152 xenocrysts of peridotitic affinity were determined with the flank method as developed by Höfer et  
153 al. (1994) and further refined by Höfer and Brey (2007). Measurements were conducted with a  
154 JEOL JXA-8530F Plus electron microprobe at Goethe University Frankfurt, Germany. The flank  
155 method and the quantitative elemental analyses were conducted simultaneously using WDS at 15  
156 kV and 120 nA, with a beam diameter of 1  $\mu\text{m}$ . Two spectrometers with TAPL crystals for high  
157 intensities and the smallest detector slit (300  $\mu\text{m}$ ) were used, with 100 s counting time for  $\text{Fe}L_{\alpha}$   
158 and  $\text{Fe}L_{\beta}$ . The  $\text{Fe}^{3+}/\Sigma\text{Fe}$  ratios for garnets were determined by applying the correction for self-  
159 absorption using natural and synthetic garnet crystals with variable total Fe and  $\text{Fe}^{3+}/\Sigma\text{Fe}$ , as

1  
2  
3  
4  
5  
6  
7  
8  
9  
10  
11  
12  
13  
14  
15  
16  
17  
18  
19  
20  
21  
22  
23  
24  
25  
26  
27  
28  
29  
30  
31  
32  
33  
34  
35  
36  
37  
38  
39  
40  
41  
42  
43  
44  
45  
46  
47  
48  
49  
50  
51  
52  
53  
54  
55  
56  
57  
58  
59  
60  
61  
62  
63  
64  
65

independently determined by Mössbauer spectroscopy (Höfer and Brey, 2007). We used  
Damknonle garnet megacrysts from Nigeria (Rankenburg et al., 2004) and the McGuire almandine  
from the U.S.A. (McGuire et al., 1992) along with three in-house Cr-pyrope standards (UA5,  
UA10, UA17) as reference materials. The Cr-pyrope crystals have a wide range of total Fe, which  
is ideal for calibration (Supp. Table 1) to obtain fit parameters derived exclusively from these three  
natural garnets. The other three spectrometers, not involved in flank method measurements, carried  
out elemental analysis of Si, Ti, Al, Cr, Fe, Mn, Ni, Mg, Ca, Na, K and P during the same  
measurement cycle. Appropriate silicate minerals [pyrope (Mg, Al, Si), albite (Na), CaSiO<sub>3</sub> (Ca)]  
and a phosphate mineral [KTiOPO<sub>4</sub>(Ti,K,P)], as well as metals or metal oxides [iron metal (Fe),  
NiO (Ni), MnTiO<sub>3</sub> (Mn), Cr<sub>2</sub>O<sub>3</sub> (Cr)] were used as calibration standards. A PRZ routine was used  
for matrix correction. The analytical uncertainty in Fe<sup>3+</sup>/ΣFe ratio measurements by the EPMA  
flank method is approximately ± 0.01 (1σ), and it is noted that in general the uncertainty is  
inversely correlated with garnet FeO content. A recent discussion about the applicability of the  
flank method for determining ferric-ferrous iron ratios can be found in Rzehak et al. (2020).

## Results

### Petrography

#### *KL2 Eclogites*

Secondary alteration is prominent in the KL2 eclogite nodules, with a general decrease in the level  
of alteration from omphacite to kyanite to garnet (Fig. 2, 3), which was also observed previously  
(Sastry et al., 2005; Patel et al., 2006; Dongre et al., 2015). Garnet crystals are least altered but  
show minor secondary carbonate and hydro-garnet replacement along grain boundaries and  
fractures. Despite the alteration of several of our KL2 eclogite samples, the secondary minerals

1  
2  
3  
4  
5  
6  
7  
8  
9  
10  
11  
12  
13  
14  
15  
16  
17  
18  
19  
20  
21  
22  
23  
24  
25  
26  
27  
28  
29  
30  
31  
32  
33  
34  
35  
36  
37  
38  
39  
40  
41  
42  
43  
44  
45  
46  
47  
48  
49  
50  
51  
52  
53  
54  
55  
56  
57  
58  
59  
60  
61  
62  
63  
64  
65

183 preserve the original rock textures, such as elongation texture with substantial micro-fracturing in  
184 garnet and clinopyroxene relics (e.g., Fig. 2, 3). Among the examined eclogite nodules, substantial  
185 clinopyroxene and kyanite alteration was observed in five samples (KL2C, KL2D, KL2E, KL2F,  
186 KL2G), whereas these phases were completely altered in sample KL2B. The freshest sample  
187 KL2A does not contain kyanite.

188 Subhedral to spherical garnet grains are interlocked with anhedral clinopyroxene and  
189 bladed kyanite in relatively fresh samples with minor alteration along grain boundaries. Inclusions  
190 of garnet and clinopyroxene are frequent in kyanite (Fig. 3 d, e, f). A few eclogite nodules (KL2D,  
191 KL2F) contain needles of corundum, which are generally spatially associated with kyanite (Fig.  
192 4a). Rutile is preserved as an inclusion in kyanite within the KL2A eclogite nodule (e.g., Fig. 4b).  
193 In the majority of samples analyzed, the relative modal proportions of garnet, omphacite and  
194 kyanite are ~45:45:10, and ~50:50 in bimineralic kyanite-free eclogite nodules with only very  
195 minor kyanite and corundum in a few samples. Carbonate and chlorite are the most prevalent  
196 alteration products of all primary minerals. Omphacite is typically replaced by hornblende and  
197 diopside, kyanite by celsian feldspar (along grain boundaries and fractures), and garnet by chlorite,  
198 epidote, celsian and grossular. The matrix of the eclogites contains rare sulfides (NiFeS) and pure  
199 nickel oxide (NiO). Mukherjee et al. (2021) reported native gold particles and Au-Pt alloys from  
200 KL2 eclogite xenoliths. A very detailed petrographic report for KL2 eclogites is given by Patel et  
201 al. (2006).

202  
203 *Peridotitic garnet xenocrysts*  
204 Fourteen peridotitic garnet xenocrysts (3-7 mm in size) from the P9 and P10 minor intrusions were  
205 mounted on thin sections and polished for in-situ mineral chemical examination of major and trace

1  
2  
3  
4  
5  
6  
7  
8  
9  
10  
11  
12  
13  
14  
15  
16  
17  
18  
19  
20  
21  
22  
23  
24  
25  
26  
27  
28  
29  
30  
31  
32  
33  
34  
35  
36  
37  
38  
39  
40  
41  
42  
43  
44  
45  
46  
47  
48  
49  
50  
51  
52  
53  
54  
55  
56  
57  
58  
59  
60  
61  
62  
63  
64  
65

206 elements. Garnet grains exhibit micro-fracturing and host rare inclusions of Cr-diopside consistent  
207 with their peridotitic mantle origins.

## 209 **Major and trace element compositions of minerals**

### 210 *KL2 eclogites*

211 The five primary minerals in KL2 eclogites (garnet, clinopyroxene, kyanite, corundum, rutile)  
212 were analyzed for major and trace elements. Secondary phases such as celsian, andradite,  
213 grossular, serpentine and carbonates were also analyzed for major elements. Supp. Table 1 lists  
214 representative major, minor and trace element compositions of primary phases essential for this  
215 work, as well as the compositions of secondary phases for documentation purposes. We only  
216 address the compositions of primary phases here, and readers are referred to Patel et al. (2006) for  
217 a detailed description of secondary phases in the KL2 eclogite xenoliths.

218 Despite the secondary alteration along grain boundaries and fractures, garnets in KL2  
219 eclogites show relatively uniform compositions (Supp. Table 1). The eclogitic garnet compositions  
220 determined here vary between  $\text{Alm}_{24-27}\text{Gr}_{825-58}\text{Pyp}_{18-48}$  falling within the range of published data  
221 for KL2 (e.g., Patel et al., 2006; Dongre et al., 2015). Garnets have low  $\text{Na}_2\text{O}$  and  $\text{TiO}_2$  contents  
222 ( $<0.3$  wt.%; Supp. Table 1), which is typical for low-pressure eclogites (Gurney and Moore, 1993).  
223 Chondrite-normalized (after Sun and McDonough, 1989) REE patterns of garnets from KL2  
224 eclogites show LREE-depletion, a positive Eu anomaly, and flat MREE-HREE distributions (Fig.  
225 5c), which is characteristic for garnets from cratonic eclogites worldwide (e.g., Jacob, 2004;  
226 Aulbach and Jacob, 2016; Aulbach and Smart, 2023). Garnets show variable trace element  
227 concentrations: Sc (29–35 ppm), Ti (828–1135 ppm), V (48–71 ppm), Cr (109–518 ppm), Ni (15–

1  
2  
3  
4  
5  
6  
7  
8  
9  
10  
11  
12  
13  
14  
15  
16  
17  
18  
19  
20  
21  
22  
23  
24  
25  
26  
27  
28  
29  
30  
31  
32  
33  
34  
35  
36  
37  
38  
39  
40  
41  
42  
43  
44  
45  
46  
47  
48  
49  
50  
51  
52  
53  
54  
55  
56  
57  
58  
59  
60  
61  
62  
63  
64  
65

228 84 ppm), Zr (2–6 ppm), and Y (5–8 ppm). They have low Sr contents (4–10 ppm) and U-Th  
229 concentrations at sub-ppm levels.

230 Clinopyroxenes are omphacitic in nature ( $Ae_{7-10}Jd_{31-43}Di_{50-61}$ ) similar to the known  
231 compositions of KL2 eclogitic clinopyroxene ( $Ae_{3-17}Jd_{13-52}Di_{41-79}$ ). Contents of  $Na_2O$  and  $Al_2O_3$   
232 range from 2.9-8.2 wt.% and 5.8-16.2 wt.%, respectively.  $Cr_2O_3$  content is low at 0.1 wt.%, rarely  
233 approaching 1.6 wt.%. Clinopyroxene shows a clear negative correlation between  $MgO$  and  $Na_2O$   
234 (inset in Fig. 5b), typical for kimberlite-borne eclogites. Their chondrite-normalized REE patterns  
235 exhibit high LREE/HREE with a notable positive Eu anomaly (Fig. 5d).

236 Kyanite in KL2 eclogite xenoliths contains trace amounts of  $FeO$  (<0.5 wt.%) and  $Cr_2O_3$   
237 (<0.9 wt.%) (Supp. Table 1). Most trace elements have concentrations below the EPMA detection  
238 limit (<30 ppm), except for Ti (106-294 ppm), V (35-70 ppm), Cr (157-604 ppm) and Ga (7-10  
239 ppm). Corundum is a pure aluminous phase with a mean  $Al_2O_3$  content of ~99 wt.% and minor  
240 amounts of  $FeO$  (<0.5 wt.%) and  $Cr_2O_3$  (<0.16 wt.%). Rutile is a pure Ti-oxide phase (~99 wt.%  
241  $TiO_2$ ) with minor amounts of  $FeO$  (<0.12 wt.%) and  $Cr_2O_3$  (<0.18 wt.%).

242  
243 *Peridotitic garnet xenocrysts*

244 Major and trace element compositions of peridotitic garnet xenocrysts were discussed in detail by  
245 Shaikh et al. (2020). For this redox study, we included 11 lherzolithic G9 grains, two harzburgitic  
246 G10 grains, and a single Ti-metasomatic G11 grain (garnet classification of Grütter et al., 2004;  
247 Fig. 6a). Overall, these garnet crystals show a wide range of  $Cr_2O_3$  (1.8–11.8 wt.%), moderate  $CaO$   
248 (4.3–5.9 wt.%) and very low  $TiO_2$  contents (<0.35 wt.%). Most of these garnets show ‘normal’  
249 chondrite-normalized REE patterns, however, xenocrysts with >5 wt.%  $Cr_2O_3$  are characterized

1  
2  
3  
4  
5  
6  
7  
8  
9  
10  
11  
12  
13  
14  
15  
16  
17  
18  
19  
20  
21  
22  
23  
24  
25  
26  
27  
28  
29  
30  
31  
32  
33  
34  
35  
36  
37  
38  
39  
40  
41  
42  
43  
44  
45  
46  
47  
48  
49  
50  
51  
52  
53  
54  
55  
56  
57  
58  
59  
60  
61  
62  
63  
64  
65

250 by ‘sinusoidal’ REE patterns (Fig. 6b). Clinopyroxene inclusions in the garnet xenocrysts are Cr-  
251 diopsides (1.1–2.1 wt.% Cr<sub>2</sub>O<sub>3</sub>; En<sub>50–55</sub>Wo<sub>41–46</sub>Fs<sub>4</sub>) with consistently high Mg# values (0.92–0.94).

### 252 **Bulk eclogite reconstruction and fO<sub>2</sub> estimates based on redox-sensitive elements**

254 Due to pervasive alteration and kimberlite melt infiltration of the KL2 eclogite nodules (see Fig.  
255 3), bulk-rock compositions were reconstructed from the measured chemical compositions of the  
256 primary minerals (clinopyroxene, garnet, corundum, rutile, ± kyanite) in combination with their  
257 estimated modal mineral abundances. This method of bulk-rock reconstruction has been widely  
258 used in the past and continues to be a valuable tool in the study of xenolithic eclogites (e.g., Jacob,  
259 2004; Tappe et al., 2011; Smart et al., 2016; Aulbach and Smart, 2023). EPMA data were used for  
260 the major elements and LA-ICP-MS data for the trace elements. The calculations were performed  
261 taking into account the specific gravities (Deer et al., 2013) of the primary minerals (3.3 g/cm<sup>3</sup> for  
262 clinopyroxene, 3.6 g/cm<sup>3</sup> for garnet, 3.3 g/cm<sup>3</sup> for kyanite, 4.04 g/cm<sup>3</sup> for rutile, 4.02 g/cm<sup>3</sup> for  
263 corundum) and for bulk eclogite (3.45 g/cm<sup>3</sup>). The specific gravity was utilized to calculate the  
264 relative weight proportions. Given that the variability of the average chemical compositions of the  
265 samples studied is low (generally <10% RSD), the major source of uncertainty in the bulk-rock  
266 reconstructions stems from the estimates of the modal mineral abundances. For biminerally  
267 kyanite-free samples, we assumed 49 vol.% for clinopyroxene and garnet each, and 1 vol.% for  
268 rutile and corundum each. For kyanite-bearing eclogite nodules, we assumed 44 vol.% for  
269 clinopyroxene and garnet each, 1 vol.% for rutile and corundum each, and 10 vol.% for kyanite.  
270 Bulk eclogite reconstruction results for the major elements (normalized to 100 wt.%) and the trace  
271 elements (in ppm) are given in Supp. Table 1. The results are plotted in Fig. 7a-c to classify the  
272 eclogites (see Discussion), which show low MgO, high Na<sub>2</sub>O, and Eu/Eu\* anomalies.

1  
2  
3  
4  
5  
6  
7  
8  
9  
10  
11  
12  
13  
14  
15  
16  
17  
18  
19  
20  
21  
22  
23  
24  
25  
26  
27  
28  
29  
30  
31  
32  
33  
34  
35  
36  
37  
38  
39  
40  
41  
42  
43  
44  
45  
46  
47  
48  
49  
50  
51  
52  
53  
54  
55  
56  
57  
58  
59  
60  
61  
62  
63  
64  
65

As shown in Figure 8a, the estimated modal abundance of rutile has a significant effect on the overall budget of Ti, which in combination with the concentration of V, provides an estimate for  $fO_2$  (e.g., Aulbach and Stachel, 2022). Based on previous analyses of mantle eclogites and our own petrographic observations, we conclude that a modal rutile abundance between 0.5 and 1 vol.% is realistic. Regardless of the exact choice of rutile abundance, our KL2 eclogite samples fall just below FMQ-2 in Figure 8a. In terms of Lu/Gd versus Ce/Yb ratios, our reconstructed bulk eclogite compositions agree with mantle eclogites from cratons worldwide, partly overlapping with metasomatized eclogites (Fig. 8b). In terms of V/Sc versus MgO systematics, our reconstructed bulk eclogite compositions suggest a  $fO_2$  value of around FMQ-2 (Fig. 8c), similar to the Ti-V based estimate (Fig. 8a).

**Thermobarometer choice**

Nimis (2022) presented an overview of geothermobarometers applicable to eclogites. Older thermometer calibrations based on garnet-clinopyroxene Fe-Mg exchange developed by Ellis and Green (1979) and Powell (1985) have been demonstrated to be unreliable because the effect of Ca was not considered (e.g., Brey and Köhler, 1990; Nimis and Grütter, 2010). Pressure estimates by Beyer et al. (2015) for eclogite xenoliths show systematically lower values (by ~10 kbar) when compared to pressures calculated using orthopyroxene-garnet assemblages at the same temperatures (Nimis, 2022). Furthermore, due to the high sensitivity of the equation to slight inaccuracies in clinopyroxene major element compositions, the Beyer et al. (2015) eclogite barometer is prone to produce significant errors.

In this study, temperatures were determined for six KL2 eclogite xenoliths (at an assumed pressure of 40 kbar) based on Fe-Mg exchange between garnet and clinopyroxene (Krogh, 1988;

1  
2  
3  
4  
5  
6  
7  
8  
9  
10  
11  
12  
13  
14  
15  
16  
17  
18  
19  
20  
21  
22  
23  
24  
25  
26  
27  
28  
29  
30  
31  
32  
33  
34  
35  
36  
37  
38  
39  
40  
41  
42  
43  
44  
45  
46  
47  
48  
49  
50  
51  
52  
53  
54  
55  
56  
57  
58  
59  
60  
61  
62  
63  
64  
65

T<sub>K</sub>). Temperatures for KL2B eclogite could not be calculated due to the complete alteration of clinopyroxene. In addition, published data for 34 KL2 eclogite nodules were reprocessed with the same thermometer equation. The eclogite equilibrium pressures (P<sub>HC40</sub>) were calculated by subsequently projecting the obtained temperatures onto the regional cratonic geotherm of 40 mW/m<sup>2</sup> (after Shaikh et al., 2020). Temperatures (T<sub>K</sub>) obtained for an assumed pressure of 40 kbar range from 945 to 1180 °C. Pressures obtained after geotherm projection range from 38 to 50 kbar (Fig. 9a), equivalent to 120-160 km depths. Alternative temperature estimates calculated after Ellis and Green (T<sub>EG</sub>; 1979), Powell (T<sub>PO</sub>; 1985), Ai (T<sub>AI</sub>; 1994), Ganguly et al. (T<sub>Gn</sub>; 1996), Krogh Ravna (T<sub>KR</sub>; 2000), and Nakamura (T<sub>NK</sub>; 2009) yielded very similar results for the KL2 eclogite xenoliths (Supp. Table 1). Overall, our P-T results compare well to those obtained by Patel et al. (2009) and Dongre et al. (2015) (i.e., 36–54 kbar).

The equilibration pressures (P<sub>HC40</sub>) for peridotitic garnet xenocrysts were calculated using Ni-in-garnet temperatures (970–1217 °C) (Canil, 1999) projected onto the regional 40 mW/m<sup>2</sup> geotherm (Fig. 9b). Pressure readings for two garnet xenocrysts (P9G51A, P9G52C) were corrected using a single-pyroxene thermobarometer applied to Cr-diopside inclusions (after Nimis and Taylor, 2000). The peridotitic garnet xenocrysts studied equilibrated at 40 to 53 kbar corresponding to ~125-170 km depth, similar to the depths of origin of the KL2 eclogite xenoliths.

**Measured ferric iron contents in garnet, and calculated fO<sub>2</sub>**

Table 1 and Table 2 list the Fe<sup>3+</sup>/ΣFe ratios for garnets from KL2 eclogite xenoliths and peridotitic garnet xenocrysts, respectively. Fe<sup>3+</sup>/ΣFe ratios for our eclogitic garnets vary from 0.02 to 0.05 (±0.01), which is within the global range of mantle-derived eclogitic garnets (0.02–0.09; Stagno et al., 2015; Smart et al., 2017, 2021a, 2021b; Aulbach et al., 2019, 2022). The Fe<sup>3+</sup>/ΣFe ratios for

1  
2  
3  
4 319 our peridotitic garnet xenocrysts range from 0.02 to 0.10 ( $\pm 0.01$ ), extending to higher values than  
5  
6  
7 320 those measured for KL2 eclogites.

8  
9 321 We calculated  $\Delta \log fO_2$  values (relative to the FMQ buffer) for the KL2 eclogite xenoliths  
10  
11 322 using the oxybarometer of Stagno et al. (2015), which was calibrated using coesite/quartz-bearing  
12  
13  
14 323 eclogites. By applying the calculated pressure–temperature values and measured chemical  
15  
16 324 compositions for garnet and clinopyroxene, the KL2 eclogites yielded  $\Delta \log fO_2$  values between  
17  
18  
19 325 FMQ-2.5 and FMQ-0.9, with uncertainties of  $\pm 0.6$  log units for corundum-free eclogites (Fig. 10).  
20  
21 326 These redox compositions fall closer to the carbonate stability field compared with the  $fO_2$   
22  
23  
24 327 systematics of other xenolithic eclogite suites from cratons worldwide (Stagno et al., 2015;  
25  
26 328 Burness et al., 2020; Smart et al., 2021a, b; Aulbach et al., 2022). The above  $fO_2$  range for the KL2  
27  
28  
29 329 eclogite xenoliths is in good agreement with our less-precise reconstructed bulk eclogite  $fO_2$   
30  
31 330 estimate of  $< \text{FMQ}-2$  (see Fig. 8). As per Smart et al. (2021), a correction is required for the  $fO_2$   
32  
33  
34 331 calculations for corundum-bearing silica-undersaturated eclogites. The correction involves the  
35  
36 332 incorporation of silica activity using corundum +  $\text{SiO}_2$  (coesite) = kyanite equilibrium. Application  
37  
38 333 of this correction to the KL2D and KL2F corundum-bearing silica-undersaturated eclogite  
39  
40  
41 334 xenoliths shifts their  $\Delta \log fO_2$  values by 1.5 log units toward more reduced redox compositions  
42  
43 335 (FMQ-3.9 and FMQ-3.6), more similar to eclogite xenoliths from the Kaapvaal craton root (Fig.  
44  
45  
46 336 10). There is a weak correlation between  $\Delta \log fO_2$  values and contents of MgO and CaO for garnet,  
47  
48 337 with  $\Delta \log fO_2$  increasing with decreasing MgO at increasing CaO (Fig. 11). No correlation is  
49  
50  
51 338 observed between the trace element concentrations of eclogitic garnets and their  $\Delta \log fO_2$  values.

52  
53 339 For the peridotitic garnet xenocrysts, we used the Stagno et al. (2013) equation, which  
54  
55 340 requires input for pressure and temperature (see above), as well as the Fe# values for coexisting  
56  
57  
58 341 olivine and orthopyroxene. The Fe# values for orthopyroxene in equilibrium with garnet were  
59  
60  
61  
62  
63  
64  
65

1  
2  
3  
4  
5  
6  
7  
8  
9  
10  
11  
12  
13  
14  
15  
16  
17  
18  
19  
20  
21  
22  
23  
24  
25  
26  
27  
28  
29  
30  
31  
32  
33  
34  
35  
36  
37  
38  
39  
40  
41  
42  
43  
44  
45  
46  
47  
48  
49  
50  
51  
52  
53  
54  
55  
56  
57  
58  
59  
60  
61  
62  
63  
64  
65

342 calculated using Equation 7 in Ryan et al. (1996) and Equation 11 in Harley (1984). The Fe# values  
343 for olivine in equilibrium with garnet were calculated by inverting the garnet-olivine thermometer  
344 of O'Neill and Wood (1979), as demonstrated by Gaul et al. (2000). The obtained Fe# values range  
345 from 0.06 to 0.08 for olivine and 0.03 to 0.04 for orthopyroxene (variance is <1%; Gaul et al.,  
346 2000; Ryan et al., 1996), corresponding to Mg# values of 0.92-0.94 and 0.96-0.97, respectively.  
347 These inferred values are similar to the Mg# values reported for olivine and orthopyroxene from  
348 rare peridotite xenoliths from the Dharwar craton root (0.90-0.94 for olivine; 0.90-0.95 for  
349 orthopyroxene; Ganguly and Bhattacharya, 1987; Nehru and Reddy, 1989; Pattnaik et al., 2020),  
350 and also overlap with the compositions of mantle-derived olivine xenocrysts from Wajrakarur  
351 kimberlites (0.90-0.94 Mg#; Shaikh et al., 2019, 2018). This complex procedure enabled us to  
352 calculate  $\Delta \log f_{O_2}$  values between FMQ-4.5 and FMQ-2.6 ( $\pm 0.9$ ) for the peridotitic garnet  
353 xenocrysts (Fig. 10).

## 355 Discussion

### 356 Nomenclature and origin of the KL2 eclogites

357 Mantle-derived eclogite xenoliths are generally thought to be formed by either (i) subduction of  
358 gabbroic or basaltic oceanic crust (e.g., Taylor and Neal, 1989; Barth et al., 2001; Jacob, 2004),  
359 (ii) emplacement of basaltic melt at depths within cratonic mantle lithosphere with high-pressure  
360 cumulate formation (e.g., Viljoen et al., 1996; Barth et al., 2002), or (iii) extraction of tonalitic  
361 melt from basaltic oceanic crust during subduction leaving behind an eclogitic residue (e.g., Jacob  
362 and Foley, 1999; Barth et al., 2002; Tappe et al., 2011a). Each of these genetic types of cratonic  
363 eclogites is supported by textural, mineralogical, geochemical, and isotopic evidence (Aulbach and  
364 Smart, 2023). Accordingly, mantle-derived eclogites have been classified into several types based

1  
2  
3  
4  
5  
6  
7  
8  
9  
10  
11  
12  
13  
14  
15  
16  
17  
18  
19  
20  
21  
22  
23  
24  
25  
26  
27  
28  
29  
30  
31  
32  
33  
34  
35  
36  
37  
38  
39  
40  
41  
42  
43  
44  
45  
46  
47  
48  
49  
50  
51  
52  
53  
54  
55  
56  
57  
58  
59  
60  
61  
62  
63  
64  
65

365 on major and trace element compositions of garnet and clinopyroxene (McCandless and Gurney,  
366 1989; Taylor and Neal, 1989; Jacob et al., 2009) and reconstructed bulk compositions (e.g.,  
367 Aulbach and Jacob, 2016; Smart et al., 2017).

368         The KL2 eclogites studied here contain clinopyroxene that is enriched in Na<sub>2</sub>O (typically  
369 4-7 wt.%) and has moderate MgO contents (typically 6-11 wt.%). These clinopyroxene  
370 compositions are characteristic for Type B and Type C eclogites of Taylor and Neal (1989; Fig.  
371 5a, b), interpreted to originate from subducted ancient oceanic crust protoliths. The relatively low  
372 K<sub>2</sub>O contents of clinopyroxene (<0.1 wt.%, or below detection limit), together with the low Na<sub>2</sub>O  
373 (0.15 wt.%) and TiO<sub>2</sub> (0.5 wt.%) contents in garnets (Supp. Table 1), are similar to the mineral  
374 compositions of Group II non-metasomatized eclogite xenoliths described by McCandless and  
375 Gurney (1989). KL2 eclogites contain garnets with moderate Mg# values (typically between 0.4-  
376 0.7) and high Ca# values (0.2-0.6) (Fig. 5; 7), similar to the high-Ca eclogites as defined by  
377 Aulbach and Jacob (2016). KL2 eclogitic garnets and clinopyroxenes exhibit Eu anomalies in their  
378 REE patterns, which are also mirrored in the reconstructed bulk eclogite compositions (Fig. 5c, d;  
379 7c). The reconstructed bulk eclogite compositions are relatively high in Na<sub>2</sub>O (2-3.5 wt.%; Fig.  
380 7a). These geochemical features indicate that the protolith of the KL2 eclogite xenoliths was a  
381 plagioclase-rich gabbroic lithology as part of ancient oceanic crust. This finding is consistent with  
382 the model by Dongre et al. (2015), who presented evidence for low-temperature alteration of the  
383 eclogite protolith near the Earth's surface based on significantly elevated  $\delta^{18}\text{O}$  values for garnet  
384 (up to +7.8‰) from some KL2 eclogite xenoliths. However, features such as interlocking garnet-  
385 clinopyroxene textures, rutile blebs in clinopyroxene and garnet, the presence of corundum and  
386 Na<sub>2</sub>O-poor garnet and K<sub>2</sub>O-poor clinopyroxene, and Eu-anomalies are more similar to Type II<sub>L</sub>  
387 eclogite xenoliths from the Roberts Victor orangeite in South Africa (Hardman et al., 2021). These

1  
2  
3  
4  
5  
6  
7  
8  
9  
10  
11  
12  
13  
14  
15  
16  
17  
18  
19  
20  
21  
22  
23  
24  
25  
26  
27  
28  
29  
30  
31  
32  
33  
34  
35  
36  
37  
38  
39  
40  
41  
42  
43  
44  
45  
46  
47  
48  
49  
50  
51  
52  
53  
54  
55  
56  
57  
58  
59  
60  
61  
62  
63  
64  
65

388 eclogite nodules are considered to represent cumulates of magmas sourced from a depleted mantle  
389 reservoir that had undergone prior extraction of MORB-like melts (Hardman et al., 2021), but  
390 subducted oceanic crustal origins have also been put forward for the classic Roberts Victor eclogite  
391 xenolith suite (e.g., Jacob et al., 2005). For KL2 eclogites, Patel et al. (2009) proposed a high-  
392 pressure cumulate origin, which is supported by textural features such as graded layering and  
393 garnet necklaces as well as garnet-kyanite clusters, plus evidence from mineral compositions such  
394 as similar clinopyroxene geochemistry in the eclogite xenoliths and cumulate pyroxenites. In  
395 contrast, Griffin et al. (2009) suggested KL2 eclogite formation by solidification of mafic melts  
396 near the base of the SCLM. Clearly, there are ‘eclogites and eclogites’, and considering the scope  
397 of our study (mantle redox), we refrain from further speculations as to the nature and origin of the  
398 KL2 eclogite protolith.

399  
400 **Redox state of KL2 eclogite xenoliths**

401 Using compositions of eclogitic garnets from the southern region of the WKF (Kalyandurga  
402 kimberlite cluster), we calculated  $\Delta\log fO_2$  values between FMQ-2.5 and FMQ-0.9 ( $\pm 0.6$ ), with  
403 two eclogite nodules (KL2C and KL2E) recording more reduced oxidation states (FMQ-3.9 and  
404 FMQ-3.6). On the basis of these  $\Delta\log fO_2$  values and their depth distribution, the KL2 eclogites  
405 straddle the boundary between diamond and carbonate stability fields in terms of carbon speciation  
406 (Fig. 10). The peridotitic garnet xenocrysts from the P9 and P10 kimberlite bodies of the northern  
407 region of the WKF (Wajrakarur-Lattavaram kimberlite cluster) yielded  $\Delta\log fO_2$  values ranging  
408 from FMQ-4.5 to FMQ-2.6 ( $\pm 0.9$ ), at the low end of eclogitic  $\Delta\log fO_2$  values determined here.  
409 This observation suggests that the majority of KL2 mantle eclogites have experienced more  
410 oxidizing conditions compared to cratonic peridotites at similar depths prior to entrainment into

1  
2  
3  
4  
5  
6  
7  
8  
9  
10  
11  
12  
13  
14  
15  
16  
17  
18  
19  
20  
21  
22  
23  
24  
25  
26  
27  
28  
29  
30  
31  
32  
33  
34  
35  
36  
37  
38  
39  
40  
41  
42  
43  
44  
45  
46  
47  
48  
49  
50  
51  
52  
53  
54  
55  
56  
57  
58  
59  
60  
61  
62  
63  
64  
65

411 erupting kimberlite magmas at ca. 1.1 Ga. The KL2 eclogite xenoliths studied have  $\Delta\log fO_2$  values  
412 that overlap with those of many kimberlite-borne eclogite nodules from cratons worldwide (FMQ-  
413 1 to FMQ-5; Stagno et al., 2015; Burness et al., 2020; Smart et al., 2021a, b; Aulbach et al., 2022).

414 Depth related redox heterogeneity has been observed for eclogites from different intervals  
415 within cratonic SCLM worldwide (e.g., Burness et al., 2020). For example, Kaapvaal cratonic  
416 eclogites from mid-lithospheric depths show more reducing redox conditions ( $\Delta\log fO_2 = \text{FMQ-}$   
417 5.3 to FMQ-3.3) compared to eclogites from the lowermost lithosphere (FMQ-3.9 to FMQ-1.5)  
418 (Burness et al., 2020). However, this apparent relationship was not observed in the data produced  
419 for other localities on the Kaapvaal craton or elsewhere (Smart et al., 2017, 2021a, b; Aulbach et  
420 al., 2022). Based on our data for KL2 eclogites, we observe notable variations in their oxidation  
421 state over a relatively narrow depth interval, but large-scale redox variations with depths cannot  
422 be discerned. Further work is required to explore such a potential relationship. We can conclude,  
423 however, that the KL2 eclogites present a suitable diamond host rock given their P-T- $fO_2$   
424 systematics (Fig. 10). This conclusion is supported by the diamondiferous nature of the KL2  
425 kimberlite body and mineral inclusion data from the WKF (Ravi et al., 2013).

### 427 **Redox state of mantle peridotites and metasomatism of the Dharwar craton root**

428 Garnet xenocrysts of peridotitic affinity from the P9 and P10 kimberlites revealed a wide range of  
429  $\Delta\log fO_2$  values between FMQ-4.5 and FMQ-2.6 ( $\pm 0.9$  log units). Griffin et al. (2009) and Shaikh  
430 et al. (2020) presented extensive trace element data for garnet and clinopyroxene xenocrysts from  
431 Wajrakarur kimberlites, which allows us to explore any possible relationship between melt  
432 metasomatism of the SCLM and its redox composition. Shaikh et al. (2020) proposed the presence  
433 of a mid-lithospheric discontinuity between ~145 and 160 km depth.

1  
2  
3  
4  
5  
6  
7  
8  
9  
10  
11  
12  
13  
14  
15  
16  
17  
18  
19  
20  
21  
22  
23  
24  
25  
26  
27  
28  
29  
30  
31  
32  
33  
34  
35  
36  
37  
38  
39  
40  
41  
42  
43  
44  
45  
46  
47  
48  
49  
50  
51  
52  
53  
54  
55  
56  
57  
58  
59  
60  
61  
62  
63  
64  
65

434 The Dharwar craton root is strongly metasomatized at the very bottom, a trend known from  
435 many lithospheric mantle profiles beneath cratons worldwide (e.g., Griffin et al., 1999b; Kopylova  
436 et al., 1999; Kargin et al., 2016; Smart et al., 2017; Aulbach et al., 2007, 2013, 2017; Tappe et al.,  
437 2021). However, unlike the Kaapvaal craton, the Dharwar SCLM shows concomitant enrichment  
438 in Zr and Y in garnet (Shaikh et al., 2020). This feature has been interpreted to result from high-  
439 temperature mantle metasomatism by mixed silicate-carbonate melts (Shaikh et al., 2020) or by  
440 basaltic melts (Griffin et al., 2009). Although, the Ti/Eu versus Zr/Hf systematics of peridotitic  
441 garnets, suggest a kimberlitic to carbonatitic nature of the metasomatic agents (Shaikh et al., 2020).

442 According to global datasets, the oxidation state of mantle peridotite varies laterally and  
443 vertically across the SCLM (e.g., Woodland and Koch, 2003; Creighton et al., 2009; Yaxley et al.,  
444 2017; Stagno et al., 2013; Tappe et al., 2021). For example, in the garnet stability field, the  
445 Kaapvaal SCLM shows a progressively more reducing trend with increasing depth ( $\Delta\log fO_2$  FMQ-  
446 2 at 110 km to FMQ-4 at 210 km; Luth, 1990; Woodland and Koch, 2003; Creighton et al., 2009,  
447 2010; Tappe et al., 2021). This crystal chemistry-controlled depth- $fO_2$  trend has been masked by  
448 oxidative metasomatism beneath the Kimberley area on the Kaapvaal craton, where many  
449 peridotite xenoliths are offset to higher-than-expected  $fO_2$  values (Creighton et al., 2009; Hanger  
450 et al., 2015). This is also consistent with observed  $Fe^{3+}$  variations in metasomatic growth zones on  
451 mantle-derived garnet crystals (McCammon et al., 2001). The peridotitic garnet xenocrysts from  
452 the WKF studied here show variations in  $\Delta\log fO_2$  and they fall within the Kaapvaal peridotite P-  
453  $fO_2$  array, with a few samples showing slightly higher  $\Delta\log fO_2$  values approaching the carbonate  
454 stability field (Fig. 10). The  $Fe^{3+}/\Sigma Fe$  ratios measured for trace element enriched garnet xenocrysts  
455 with normal REE patterns show a positive correlation with incompatible trace element  
456 concentrations (Ti, Zr, Y, V; Fig. 12), possibly indicating a metasomatic control on cratonic mantle

1  
2  
3  
4  
5  
6  
7  
8  
9  
10  
11  
12  
13  
14  
15  
16  
17  
18  
19  
20  
21  
22  
23  
24  
25  
26  
27  
28  
29  
30  
31  
32  
33  
34  
35  
36  
37  
38  
39  
40  
41  
42  
43  
44  
45  
46  
47  
48  
49  
50  
51  
52  
53  
54  
55  
56  
57  
58  
59  
60  
61  
62  
63  
64  
65

457 redox (Creighton et al., 2009). These garnet xenocrysts were sampled from ~125–160 km depths,  
458 an SCLM interval that was identified as a modally metasomatized mid-lithospheric discontinuity  
459 by Shaikh et al. (2020). Overall, the link between carbonated silicate melt metasomatism and  
460 mantle redox in the Dharwar craton root may be responsible for local diamond destruction, as  
461 reported for other cratons worldwide (Creighton et al., 2009; Fedortchouk et al., 2019).

462

### 463 **Linking mantle redox and the diversity of 1.1 Ga kimberlitic magmatism in India**

464 The WKF comprises a diverse range of diamondiferous magma types, including archetypal  
465 kimberlites, lamproites, orangeites, and ultramafic lamprophyres (see compilation in Shaikh et al.,  
466 2017; Pandey and Chalapathi Rao, 2020). To date, 48 minor intrusions of exclusively  
467 Mesoproterozoic age (ca. 1.1 Ga) are known to occur within a relatively small area that is 80 × 70  
468 km in size. The coeval emplacement of diverse volatile-rich ultramafic magma types reflects  
469 prominent mineralogical heterogeneity in the Dharwar craton root (e.g., Sarkar et al., 2021), as  
470 was also demonstrated for cratonic regions and their primitive potassic magmatism on either side  
471 of the North Atlantic (Tappe et al., 2008, 2011b; Dalton et al., 2019).

472         The correlation between metasomatic overprint and redox state of the Dharwar craton root,  
473 as demonstrated in this study, appears to have important implications for the petrogeneses of  
474 kimberlites, lamproites and closely related primitive potassic rocks. Progressive oxidative  
475 metasomatism along conduits in the SCLM was caused by infiltrating carbonated silicate melts  
476 that probably originated from low-degree partial melting of the underlying convecting mantle  
477 including its recycled crustal components (e.g., Nowell et al., 2004; Malkovets et al., 2007). The  
478 resultant  $fO_2$  heterogeneities in the SCLM allowed for stabilization of distinctly different  
479 metasomatic assemblages that may be dominated by either amphiboles, micas, or carbonates

1  
2  
3  
4  
5  
6  
7  
8  
9  
10  
11  
12  
13  
14  
15  
16  
17  
18  
19  
20  
21  
22  
23  
24  
25  
26  
27  
28  
29  
30  
31  
32  
33  
34  
35  
36  
37  
38  
39  
40  
41  
42  
43  
44  
45  
46  
47  
48  
49  
50  
51  
52  
53  
54  
55  
56  
57  
58  
59  
60  
61  
62  
63  
64  
65

480 (Foley et al., 1986; Foley, 2011; Tappe et al., 2008; Yaxley et al., 2017). The highly variable nature  
481 of SCLM metasomes, and also local lack of metasomes, may explain the close spatiotemporal  
482 association of diverse types of primitive K-rich magmas (lamproites, orangeites, ultramafic  
483 lamprophyres) and kimberlites in the WKF.

Shaikh et al. (2017) suggested a model for the origin of various types of diamond-bearing  
485 magmas in the WKF, following concepts developed in Tappe et al. (2008, 2011b), where  
486 carbonated silicate melts from the asthenosphere interacted with variably metasomatized  
487 lithologies of the SCLM to produce the diversity of ca. 1.1 Ga old volatile-rich ultramafic rocks  
488 known from southern India. According to this model, metasomatic phlogopite–carbonate  
489 dominated veins were reactivated by infiltrating asthenosphere-derived melts (proto-kimberlitic  
490 melts), which gave rise to ultramafic lamprophyre, orangeite and lamproite magmas as a function  
491 of increasingly higher proportions of micas in the cratonic mantle source (Shaikh et al., 2017).  
Sarkar et al. (2021) compared the compositions of magmatic and xenocrystic olivine populations  
493 from Wajrakarur kimberlites and lamproites. These authors suggested that both magma types have  
494 a common asthenospheric mantle source, with lamproites revealing a larger extent of assimilation  
495 of Fe-rich lithospheric metasomes.

**On the ‘overabundance’ of eclogite xenoliths in the KL2 kimberlite**

498 Despite the general xenolith deficiency, the WKF minor intrusions reveal contrasting mantle  
499 sampling patterns. For example, the KL2 kimberlite is marked by an overabundance of eclogite  
500 xenoliths, whereas kimberlites and related rocks from the Wajrakarur-Lattavaram cluster contain  
501 more peridotite xenoliths (Rao et al., 2001; Patel et al., 2006). This apparent bias is also mirrored

1  
2  
3  
4  
5  
6  
7  
8  
9  
10  
11  
12  
13  
14  
15  
16  
17  
18  
19  
20  
21  
22  
23  
24  
25  
26  
27  
28  
29  
30  
31  
32  
33  
34  
35  
36  
37  
38  
39  
40  
41  
42  
43  
44  
45  
46  
47  
48  
49  
50  
51  
52  
53  
54  
55  
56  
57  
58  
59  
60  
61  
62  
63  
64  
65

502 by the diamond occurrences (Ravi et al., 2013) and distributions of eclogitic versus peridotitic  
503 garnet xenocrysts (Griffin et al., 2009; Shaikh et al., 2020).

504         Although kimberlites and related rocks with an overabundance of eclogite xenoliths are  
505 very rare, they occur on most cratons worldwide such as the Kaapvaal craton (e.g., Roberts Victor,  
506 Bellsbank), the Slave craton (e.g., Jericho, Voyageur), the North Atlantic craton (e.g., Nunatak  
507 1390) and the Siberian craton (e.g., Zagadochnaya) (Schulze, 1989; Jacob, 2004; Smart et al.,  
508 2009, 2017, 2021a; Tappe et al., 2011a; Kopylova et al., 2016; Hardman et al., 2021; Aulbach and  
509 Smart, 2023). Eclogite xenolith overabundance has been linked to localized enrichment of the  
510 peridotite-dominated cratonic mantle column with eclogite components (e.g., Nixon and Davies,  
511 1987) or biased preservation of xenoliths during entrainment into kimberlitic magmas (e.g.,  
512 Schulze, 1989). Kopylova et al. (2016) inferred lateral continuity of eclogites within the Slave  
513 craton SCLM, where an eclogite-rich layer may represent the remnant of an imbricated oceanic  
514 lithosphere slab. The abundance of eclogite components has great economic significance because  
515 they contribute up to 30% of lithospheric diamonds in global statistics (Stachel and Luth, 2015),  
516 which can be even higher on a regional scale. The overall abundance of eclogitic components in  
517 peridotite-dominated SCLM has been estimated at <1 vol.% (Schulze, 1989); however, higher  
518 abundances of up to 4-10 vol.% have been suggested for the Slave craton (Griffin et al., 1999;  
519 Kopylova et al., 2016). The combined petrological-geophysical approach by Garber et al. (2018)  
520 devised an even higher eclogite abundance within the SCLM beneath cratons (up to 20 vol.%).  
521 Regardless of the exact amount of eclogites within the cratonic mantle lithosphere, the KL2  
522 occurrence on the Eastern Dharwar craton adds to the kimberlite localities that have a somewhat  
523 inexplicable abundance of xenolithic eclogites, which may influence the redox distribution within  
524 the local SCLM and, by inference, also its volatile element and diamond inventory.

1  
2  
3  
4  
5  
6  
7  
8  
9  
10  
11  
12  
13  
14  
15  
16  
17  
18  
19  
20  
21  
22  
23  
24  
25  
26  
27  
28  
29  
30  
31  
32  
33  
34  
35  
36  
37  
38  
39  
40  
41  
42  
43  
44  
45  
46  
47  
48  
49  
50  
51  
52  
53  
54  
55  
56  
57  
58  
59  
60  
61  
62  
63  
64  
65

525

## 526 **Summary and Conclusions**

527 The  $\text{Fe}^{3+}/\Sigma\text{Fe}$  compositions of garnets were determined by the EPMA flank method for six eclogite  
528 xenoliths from the KL2 kimberlite and fourteen peridotite-derived xenocrysts from the P9 and P10  
529 kimberlites on the Eastern Dharwar craton in southern India. KL2 eclogites are characterized by  
530 low  $\Delta\log f\text{O}_2$  values between FMQ-3.9 and FMQ-0.9 ( $\pm 0.6$ ), which suggests that they could have  
531 acted as diamond host rocks within the deeper Dharwar craton root. The peridotite-derived garnet  
532 xenocrysts reveal a wide range of  $\Delta\log f\text{O}_2$  values between FMQ-4.5 and FMQ-2.6 ( $\pm 0.9$ ), firmly  
533 within the well-studied Kaapvaal lithospheric mantle array. At mid-lithospheric depths beneath  
534 the Dharwar craton, redox compositions of the garnet xenocrysts correlate with geochemical  
535 proxies for melt-rock interactions, which provides evidence for the operation of oxidative mantle  
536 metasomatism that was likely diamond-destructive. Strong redox variability at relatively confined  
537 SCLM intervals would promote stability of diverse volatile-rich metasomatic mineral assemblages  
538 (e.g., roles of carbonates versus phlogopite and amphibole), which helps to explain the  
539 spatiotemporal association of ca. 1.1 Ga kimberlites, lamproites, orangeites and ultramafic  
540 lamprophyres in southern India.

541

## 542 **Acknowledgments**

543 AMS and ST acknowledge financial support from CIMERA and the UJ Faculty of Science for the  
544 research presented here. The research presented in this paper was also supported by funds provided  
545 to FV under the South African Department of Science and Innovation Research Chairs Initiative  
546 (SARChI), as administered by the National Research Foundation (grant number 64779). The  
547 RESOLUTION laser instrumentation at the University of Johannesburg was funded by NRF-NEP

1  
2  
3  
4  
5  
6  
7  
8  
9  
10  
11  
12  
13  
14  
15  
16  
17  
18  
19  
20  
21  
22  
23  
24  
25  
26  
27  
28  
29  
30  
31  
32  
33  
34  
35  
36  
37  
38  
39  
40  
41  
42  
43  
44  
45  
46  
47  
48  
49  
50  
51  
52  
53  
54  
55  
56  
57  
58  
59  
60  
61  
62  
63  
64  
65

548 grant #93208, and its up-keeping is supported by DSI-NRF CIMERA. We warmly thank Christian  
549 Reinke for assisting with the EPMA data collection at UJ. Bill Griffin is thanked for his guidance  
550 in modeling the Mg-numbers of ‘ghost’ olivine in equilibrium with peridotitic garnet xenocrysts.  
551 Sonja Aulbach is thanked for interesting discussions. We are grateful to Vincenzo Stagno and  
552 Katie Smart for their helpful comments on this manuscript. Othmar Müntener is gratefully  
553 acknowledged for consummate editorial handling.

555 **References**

556 Ai Y (1994) A revision of the garnet-clinopyroxene  $Fe^{2+}$ -Mg exchange geothermometer.  
557 *Contrib Mineral Petrol*, 115:467–473

558 Aulbach S, Stachel T (2022) Evidence for oxygen-conserving diamond formation in redox-  
559 buffered subducted oceanic crust sampled as eclogite. *Nature Commun* 13:1924

560 Aulbach S, Jacob DE (2016) Major- and trace-elements in cratonic mantle eclogites and  
561 pyroxenites reveal heterogeneous sources and metamorphic processing of low-pressure  
562 protoliths. *Lithos* 262:586–605

563 Aulbach S, Viljoen KS (2015) Eclogite xenoliths from the Lacey kimberlite, Kaapvaal craton:  
564 From convecting mantle source to palaeo-ocean floor and back. *Earth Planet Sci Lett* 431:274–  
565 286

566 Aulbach S, Griffin WL, Pearson NJ, O’Reilly SY (2013) Nature and timing of metasomatism in  
567 the stratified mantle lithosphere beneath the central Slave craton (Canada). *Chem Geol*  
568 352:153–169

569 Aulbach S, Griffin WL, Pearson NJ, O’Reilly SY, Doyle BJ (2007) Lithosphere formation in the  
570 Central Slave Craton (Canada): plume accretion or lithosphere accretion. *Contrib Mineral Petrol*  
571 154:409–428

572 Aulbach S, Sun J, Tappe S, Höfer HE, Gerdes A (2017) Volatile-rich metasomatism in the  
573 cratonic mantle beneath SW Greenland: Link to kimberlites and mid-lithospheric  
574 discontinuities. *J Petrol* 58(12):2311–2338

575 Aulbach S, Woodland AB, Stagno V, Korsakov AV, Mikhailenko D, Golovin A (2022)  $Fe^{3+}$   
576 Distribution and  $Fe^{3+}/\Sigma Fe$ -Oxygen Fugacity Variations in Kimberlite-Borne Eclogite Xenoliths,  
577 with Comments on Clinopyroxene-Garnet Oxy-Thermobarometry. *J Petrol* 63(8): egac076

1  
2  
3  
4 578 Aulbach S, Woodland AB, Stern RA, Vasilyev P, Heaman LM, Viljoen KS (2019) Evidence for  
5 579 a dominantly reducing Archaean ambient mantle from two redox proxies, and low oxygen  
6 580 fugacity of deeply subducted oceanic crust. *Sci Reports*, 9(1):1–11  
7  
8  
9 581 Babu EVSSK, Griffin WL, Panda S, O'Reilly SY (2008) Eclogite xenoliths from the kimberlites  
10 582 of the Eastern Dharwar Craton, south India: material representing ancient crust of the Western  
11 583 Dharwar Craton? 9th International Kimberlite Conference, Frankfurt, Extended Abstract 9IKC-  
12 584 A-00161  
13  
14  
15 585 Ballhaus C, Berry RF, Green DH (1991) High pressure experimental calibration of the olivine-  
16 586 orthopyroxene-spinel oxygen geobarometer: implications for the oxidation state of the upper  
17 587 mantle. *Contrib Miner Petrol* 107:27–40  
18  
19  
20 588 Barth MG, Rudnick RL, Horn I, McDonough WF, Spicuzza M, Valley JR, Haggerty SE (2001)  
21 589 Geochemistry of xenolithic eclogites from West Africa: Part I. A link between low MgO  
22 590 eclogites and Archean crust formation. *Geochim Cosmochim Acta* 65:1499–1527  
23  
24  
25 591 Barth MG, Rudnick RL, Horn I, McDonough WF, Spicuzza M, Valley JR, Haggerty SE (2002)  
26 592 Geochemistry of xenolithic eclogites from West Africa: Part II. Origins of the high MgO  
27 593 eclogites. *Geochim Cosmochim Acta* 66, 4325–4345  
28  
29  
30 594 Beyer C, Frost DJ, Miyajima N (2015) Experimental calibration of a garnet–clinopyroxene  
31 595 geobarometer for mantle eclogites. *Contrib Mineral Petrol* 169(2)  
32  
33  
34 596 Brey GP, Kohler T (1990) Geothermobarometry in four-phase lherzolites II. New  
35 597 thermobarometers, and practical assessment of existing thermometers. *J Petrol* 31:1353–1378  
36  
37 598 Burness S, Smart KA, Tappe S, Stevens G, Woodland AB, Cano E (2020) Sulphur-rich mantle  
38 599 metasomatism of Kaapvaal craton eclogites and its role in redox-controlled platinum group  
39 600 element mobility. *Chem Geol* 542:119476  
40  
41  
42 601 Canil D (1999) The Ni-in-garnet geothermometer: Calibration at natural abundances. *Contrib*  
43 602 *Mineral Petrol* 136(3):240–246  
44  
45  
46 603 Chadwick B, Vasudev VN, Hegde GV (2000) The Dharwar craton, southern India, interpreted  
47 604 as the result of Late Archean oblique convergence. *Precambri Res* 99:91–111  
48  
49  
50 605 Chatterjee A, Chalapathi Rao N, Pandey R, Pandey A (2023) Mantle transition zone-derived  
51 606 eclogite xenolith entrained in a diamondiferous Mesoproterozoic (~1.1 Ga) kimberlite from the  
52 607 Eastern Dharwar Craton, India: Evidence from a coesite, K-omphacite, and majoritic garnet  
53 608 assemblage. *Geol Mag* 1–14  
54  
55  
56 609 Creighton S, Stachel T, Eichenberg D, Luth RW (2010) Oxidation state of the lithospheric  
57 610 mantle beneath Diavik diamond mine, central Slave craton, NWT, Canada. *Contrib Mineral*  
58 611 *Petrol* 159:645–657  
59  
60  
61  
62  
63  
64  
65

1  
2  
3  
4 612 Creighton S, Stachel T, Matveev S, Höfer H, McCammon C, Luth RW (2009) Oxidation of the  
5 613 Kaapvaal lithospheric mantle driven by metasomatism. *Contrib Mineral Petrol* 157, 491–504  
6  
7 614 Dalton H, Giuliani A, O’Brien H, Phillips D, Hergt J, Maas R (2019) Petrogenesis of a hybrid  
8 615 cluster of evolved kimberlites and ultramafic lamprophyres in the Kuusamo area, Finland. *J Pet*  
9 616 *60*, 2025–2050  
10  
11 617 Day HW (2012) A revised diamond-graphite transition curve. *American Mineralogist*, 97(1),  
12 618 52–62  
13  
14 619 Deer WA, Howie FRS, Zussman J (2013) *An Introduction to the Rock-Forming Minerals*.  
15 620 Mineralogical Society of Great Britain and Ireland, doi:10.1180/DHZ  
16  
17 621 Dongre AN, Jacob DE, Stern RA (2015) Subduction related origin of eclogite xenoliths from the  
18 622 Wajrakarur kimberlite field, Eastern Dharwar craton, Southern India: Constraints from  
19 623 petrology and geochemistry. *Geochim Cosmochim Acta* 166:165–188  
20  
21 624 Ellis DJ, Green DH (1979) An experimental study of the effect of Ca upon garnet clinopyroxene  
22 625 Fe–Mg exchange equilibria. *Contrib Mineral Petrol* 71:13–22  
23  
24 626 Fedortchouk Y, Liebske C, McCammon C (2019) Diamond destruction and growth during  
25 627 mantle metasomatism: an experimental study of diamond resorption features. *Earth Planet Sci*  
26 628 *Lett*, 506, 493–506  
27  
28 629 Foley SF (2011) A reappraisal of redox melting in the Earth's mantle as a function of tectonic  
29 630 setting and time. *J Pet* 52, 1363–1391  
30  
31 631 Foley SF, Taylor WR, Green DH (1986) The role of fluorine and oxygen fugacity in the genesis  
32 632 of the ultrapotassic rocks. *Contrib Mineral Petrol* 94, 183–192  
33  
34 633 Ganguly J, Bhattacharya PK (1987) Xenoliths in Proterozoic Kimberlites from Southern India:  
35 634 petrology and Geophysical Implications. In: Nixon, P. H. (ed.) *Mantle Xenoliths*. John Wiley  
36 635 and Sons, pp 249–265  
37  
38 636 Ganguly J, Cheng W, Tirone M (1996) Thermodynamics of aluminosilicate garnet solid  
39 637 solution: new experimental data, an optimized model, and thermometric applications. *Contrib*  
40 638 *Mineral Petrol* 126:137–151  
41  
42 639 Garber JM, Maurya S, Hernandez JA, Duncan MS, Zeng L, Zhang HL, Faul U, McCammon C,  
43 640 Montagner JP, Moresi L, Romanowicz BA, Rudnick RL, Stixrude L (2018) Multidisciplinary  
44 641 Constraints on the Abundance of Diamond and Eclogite in the Cratonic Lithosphere. *Geochem*  
45 642 *Geophys Geosys* 19(7):2062–2086  
46  
47 643 Gaul OF, Griffin WL, O’Reilly SY, Pearson NJ (2000) Mapping olivine composition in the  
48 644 lithospheric mantle. *Earth Planet Sci Lett* 182(3–4):223–235  
49  
50  
51  
52  
53  
54  
55  
56  
57  
58  
59  
60  
61  
62  
63  
64  
65

- 1  
2  
3  
4 645 Griffin WL, Doyle BJ, Ryan CG, Pearson NJ, Suzanne YO, Davies R, Kivi K, Van Achterbergh  
5 646 E, Natapov LM (1999). Layered mantle lithosphere in the Lac de Gras area, Slave craton:  
6 647 composition, structure and origin. *J Petrol* 40:705–727  
8  
9 648 Griffin WL, Kobussen AF, Babu EVSSK, O’Reilly SY, Norris R, Sengupta P (2009) A  
10 649 translithospheric suture in the vanished 1-Ga lithospheric root of South India: evidence from  
11 650 contrasting lithosphere sections in the Dharwar Craton. *Lithos* 112:1109–1119  
13  
14 651 Grütter HS, Gurney JJ, Menzies AH, Winter F (2004) An updated classification scheme for  
15 652 mantle-derived garnet, for use by diamond explorers. *Lithos* 77:841–857  
17  
18 653 Gurney JJ, Moore RO (1993) Geochemical correlations between kimberlitic indicator minerals  
19 654 and diamonds. In: *Diamonds: Exploration, Sampling and Evaluation*. Proceedings of PDAC  
20 655 Short Course, 147:149–171  
22  
23 656 Hanger BJ, Yaxley GM, Berry AJ, Kamenetsky VS (2015) Relationships between oxygen  
24 657 fugacity and metasomatism in the Kaapvaal subcratonic mantle, represented by garnet peridotite  
25 658 xenoliths in the Wesselton kimberlite, South Africa. *Lithos* 212, 443–452  
27  
28 659 Hardman MF, Stachel T, Pearson DG, Cano EJ, Stern RA, Sharp ZD (2021) Characterising the  
29 660 Distinct Crustal Protoliths of Roberts Victor Type i and II Eclogites. *J Petrol* 62(12):1–19  
30  
31 661 Harley SL (1984) An experimental study of the partitioning of Fe and Mg between garnet and  
32 662 orthopyroxene. *Contrib Mineral Petrol* 86:359–373  
33  
34 663 Höfer HE, Brey GP (2007) The iron oxidation state of garnet by electron microprobe: its  
35 664 determination with the flank method combined with major-element analysis. *Am Mineral*  
37 665 92:873–885  
38  
39 666 Höfer HE, Brey GP, Schulz-Dobrick B, Oberhänsli R (1994) The determination of the oxidation  
40 667 state of iron by the electron microprobe. *Eur J Mineral* 6:407–418  
42  
43 668 Jacob DE (2004) Nature and origin of eclogite xenoliths from kimberlites. *Lithos*, 77:295-316  
44  
45 669 Jacob DE, Bizimis M, Salters VJM (2005) Lu-Hf and geochemical systematics of recycled  
46 670 ancient oceanic crust: Evidence from Roberts Victor eclogites. *Contributions to Mineral Petrol*  
48 671 148, 707–720  
49  
50 672 Jacob DE, Foley SF (1999) Evidence for Archean ocean crust with low high field strength  
51 673 element signature from diamondiferous eclogite xenolith. *Lithos* 48:317–336  
52  
53 674 Jacob DE, Viljoen KS, Grassineau NV (2009) Eclogite xenoliths from Kimberley, South Africa  
54 675 - A case study of mantle metasomatism in eclogites. *Lithos* 112:1002–1013  
56  
57 676 Jochum KP, Weis U, Schwager B, Stoll B, Wilson SA, Haug GH, Andreae MO, Enzweiler J  
58 677 (2016) Reference values following ISO guidelines for frequently requested rock reference  
59 678 materials. *Geostanda Geoana Res* 40, 333–350  
61  
62  
63  
64  
65

- 1  
2  
3  
4 679 Kargin AV, Sazonova LV, Nosova AA, Tretyachenko VV (2016) Composition of garnet and  
5 680 clinopyroxene in peridotite xenoliths from the Grib kimberlite pipe, Arkhangelsk diamond  
6 681 province, Russia: Evidence for mantle metasomatism associated with kimberlite melts. *Lithos*  
7 682 262:442–455
- 10 683 Kopylova MG, Beausoleil Y, Goncharov A, Burgess J, Strand P (2016) Spatial distribution of  
11 684 eclogite in the Slave cratonic mantle: The role of subduction. *Tectonophy* 672–673:87–103
- 14 685 Kopylova MG, Russell JK, Cookenboo H (1999) Petrology of peridotite and pyroxenite  
15 686 xenoliths from the Jericho kimberlite: implications for the thermal state of the mantle beneath  
16 687 the Slave craton, Northern Canada. *J Petrol* 40:79–104
- 19 688 Krogh Ravna E (2000) The garnet-clinopyroxene Fe<sup>2+</sup>–Mg geothermometer: an updated  
20 689 calibration. *Journal of Metamorphic Geology* 18, 211–219
- 22 690 Krogh, EJ (1988) The garnet-clinopyroxene Fe–Mg geothermometer – a reinterpretation of  
23 691 existing experimental data. *Contrib Mineral Petrol* 99:44–48
- 26 692 Luth RW, Virgo D, Boyd FR, Wood BJ (1990) Ferric iron in mantle derived garnets:  
27 693 implications for thermobarometry and for the oxidation state of the mantle. *Contrib Mineral*  
28 694 *Petrol* 104:56–72
- 31 695 McCammon CA, Griffin WL, Shee SR, O’Neill HSC (2001) Oxidation during metasomatism in  
32 696 ultramafic xenoliths from the Wesselton kimberlite, South Africa: implications for the survival  
33 697 of diamond. *Contrib Mineral Petrol* 141:287–296
- 36 698 McCandless T, Gurney J (1989) Sodium in garnet and potassium in clinopyroxene: criteria for  
37 699 classifying mantle eclogites. In: Ross J, Jaques AL, Ferguson J, Green DH, O’Reilly SY,  
38 700 Danchin RV, Janse AJA (eds) *Kimberlite and related rocks*. Special publication—Geological  
39 701 Society of Australia, Perth
- 42 702 McGuire AV, Francis CA, Dyar MD (1992) Mineral standards for microprobe analysis of  
43 703 oxygen. *Am Mineral*, 77, 1087–1091
- 46 704 Mikhailenko DS, Stagno V, Korsakov AV, Andreozzi GB, Marras G, Cerantola V, Malygina  
47 705 EV (2020) Redox state determination of eclogite xenoliths from Udachnaya kimberlite pipe  
48 706 (Siberian craton), with some implications for the graphite/diamond formation. *Contrib Mineral*  
49 707 *Petrol* 175(11):1–17
- 52 708 Mukherjee A, Tiwari P, Verma CB, Babu EVSSK, Sarathi JP (2021) Native Gold and Au-Pt  
53 709 Alloy in Eclogite Xenoliths of Kalyandurg KL-2 Kimberlite, Anantapur District, South India. *J*  
54 710 *Geolog Soc India* 97(6):567–570
- 57 711 Nakamura D (2009) A new formulation of garnet–clinopyroxene geothermometer based on  
58 712 accumulation and statistical analysis of a large experimental data set. *Journal of Metamorphic*  
59 713 *Geology* 27(7):495–508

- 1  
2  
3  
4 714 Neelakantam S (2001) Exploration for diamonds in southern India. *Geol Surv India Spec Publ*  
5 715 58:521–555  
6  
7  
8 716 Nimis P (2022) Pressure and Temperature Data for Diamonds. *Rev Mineral Geochem*  
9 717 88(1):533–565  
10  
11 718 Nimis P, Grütter H (2010) Internally consistent geothermometers for garnet peridotites and  
12 719 pyroxenites. *Contrib Mineral Petrol* 159(3):411–427  
13  
14  
15 720 Nimis P, Taylor WR (2000) Single clinopyroxene thermobarometry for garnet peridotites. Part  
16 721 I. Calibration and testing of a Cr-in-Cpx barometer and an enstatite-in-Cpx thermometer.  
17 722 *Contrib Mineral Petrol* 139:541–554  
18  
19  
20 723 Nixon PH, Davies GR (1987) Mantle xenolith perspectives. In: Nixon PH (ed) *Mantle xenoliths*.  
21 724 Wiley, New York, pp 742–756  
22  
23 725 Nowell GM, Pearson DG, Bell DR, Carlson RW, Smith CB, Kempton PD, Noble SR (2004) Hf  
24 726 isotope systematics of kimberlites and their megacrysts: New constraints on their source  
25 727 regions. *J Petrol* 45(8):1583–1612  
26  
27  
28 728 O’Neill HSC, Wood BJ (1979) An experimental study of Fe-Mg partitioning between garnet  
29 729 and olivine and its calibration as a geothermometer. *Contrib Mineral Petrol* 70:59–70  
30  
31  
32 730 Pandey A, Chalapathi Rao NV (2020) Supercontinent transition as a trigger for ~1.1 Gyr  
33 731 diamondiferous kimberlites and related magmatism in India. *Lithos* 370–371  
34  
35 732 Patel SC, Ravi S, Anil Kumar Y, Naik A, Thakur SS, Pati JK, Nayak SS (2009) Mafic xenoliths  
36 733 in proterozoic kimberlites from Eastern Dharwar Craton, India: mineralogy and P–T regime. *J*  
37 734 *Asian Earth Sci* 34:336–346  
38  
39  
40 735 Patel SC, Ravi S, Thakur SS, Rao TK, Subbarao KV (2006) Eclogite xenoliths from Wajrakarur  
41 736 kimberlites, southern India. *Mineral Petrol* 88(1–2):363–380  
42  
43  
44 737 Pattnaik J, Ghosh S, Dongre A (2020) Plume activity and carbonated silicate melt  
45 738 metasomatism in Dharwar cratonic lithosphere: Evidence from peridotite xenoliths in  
46 739 Wajrakarur kimberlites. *Lithos* 376–377  
47  
48  
49 740 Powell R (1985) Regression diagnostics and robust regression in geothermometer/ geobarometer  
50 741 calibration: the garnet-clinopyroxene geothermometer revisited. *J Metamor Geol* 3:231–243  
51  
52 742 Rao KRP, Nayak SS, Reddy TAK, Dhakate MV, Chowdary VS, Ravi S, Suresh G, Rao KS B  
53 743 (2001) Geology, petrology, geochemistry and mineral chemistry of new kimberlite finds in the  
54 744 Wajrakarur Kimberlite Field, Anantapur district, Andhra Pradesh. Geological Survey of India  
55 745 Special Publication 58:593–602  
56  
57  
58  
59  
60  
61  
62  
63  
64  
65

1  
2  
3  
4 746 Rankenburg K, Lassiter JC, Brey GP (2004) Origin of megacrysts in volcanic rocks of the  
5 747 Cameroon volcanic chain—constraints on magma genesis and crustal contamination. *Contrib*  
6 748 *Mineral Petrol*, 147, 129–144  
7  
8  
9 749 Ravi S, Sufija MV, Patel SC, Sheikh JM, Sridhar M, Kaminsky FV, Khachatryan GK, Nayak  
10 750 SS, Bhaskara Rao KS (2013) Diamond potential of the Eastern Dharwar Craton, Southern India,  
11 751 and a reconnaissance study of physical and infrared characteristics of the diamonds. In: Pearson,  
12 752 DG (eds) *Proceedings of 10th International Kimberlite Conference. Special Issue J Geol Soc*  
13 753 *India* 1:335–348  
14  
15  
16  
17 754 Ryan CG, Griffin WL, Pearson NJ (1996) Garnet geotherms: pressure-temperature data from  
18 755 Cr-pyrope garnet xenocrysts in volcanic rocks. *J Geophys Res: Solid Earth* 101:5611–5625  
19  
20 756 Rzehak LJ, Rohrbach A, Vollmer C, Höfer HE, Berndt J, Klemme S (2020) Ferric-ferrous iron  
21 757 ratios of experimental majoritic garnet and clinopyroxene as a function of oxygen fugacity.  
22 758 *American Mineralogist: J Earth Planet Mater* 105(12):1866–1874  
23  
24  
25 759 Sarkar S, Giuliani A, Ghosh S, Phillips D (2021) Petrogenesis of coeval lamproites and  
26 760 kimberlites from the Wajrakarur field, Southern India: New insights from olivine compositions.  
27 761 *Lithos* 406–407:106524  
28  
29  
30 762 Sastry CA, Rao GR, Prasad GJS, Reddy VA (2005) Electron probe microanalysis of indicator  
31 763 minerals from kimberlites of Andhra Pradesh and Karnataka – basic data. *Geol Surve India*  
32 764 *Bullet* 6:282  
33  
34  
35 765 Schulze DJ (1989) Constraints on the abundance of eclogite in the upper mantle. *J Geophys Res*  
36 766 94:4205–4212  
37  
38  
39 767 Shaikh AM, Patel SC, Ravi S, Behera D, Pruseth KL (2017) Mineralogy of the TK1 and TK4  
40 768 ‘kimberlites’ in the Timmasamudram cluster, Wajrakarur Kimberlite Field, India: Implications  
41 769 for lamproite magmatism in a field of kimberlites and ultramafic lamprophyres. *Chem Geol*  
42 770 455:208–230  
43  
44  
45 771 Shaikh AM, Kumar SP, Patel SC, Thakur SS, Ravi S, Behera D (2018) The P3 kimberlite and  
46 772 P4 lamproite, Wajrakarur kimberlite field, India: mineralogy, and major and minor element  
47 773 compositions of olivines as records of their phenocrystic vs xenocrystic origin. *Mineral Petrol*  
48 774 112:609–624  
49  
50  
51 775 Shaikh AM, Patel SC, Bussweiler Y, Kumar SP, Tappe S, Ravi S, Mainkar D (2019) Olivine  
52 776 trace element compositions in diamondiferous lamproites from India: Proxies for magma origins  
53 777 and the nature of the lithospheric mantle beneath the Bastar and Dharwar cratons. *Lithos* 324–  
54 778 325:501–518  
55  
56  
57 779 Shaikh AM, Tappe S, Bussweiler Y, Patel SC, Ravi S, Bolhar R, Viljoen F (2020)  
58 780 *Clinopyroxene and Garnet Mantle Cargo in Kimberlites as Probes of Dharwar Craton*

1  
2  
3  
4 781 Architecture and Geotherms, with Implications for Post-1.1 Ga Lithosphere Thinning Events  
5  
6 782 Beneath Southern India. *J Petrol* 61(9)  
7  
8 783 Smart KA, Heaman LM, Chacko T, Simonetti A, Kopylova M, Mah D, Daniels D (2009) The  
9 784 origin of high-MgO diamond eclogites from the Jericho kimberlite, Canada. *Earth Planet Sci*  
10 785 *Lett* 284, 527–537  
11  
12 786 Smart KA, Tappe S, Simonetti A, Simonetti SS, Woodland AB, Harris C (2017) Tectonic  
13 787 significance and redox state of Paleoproterozoic eclogite and pyroxenite components in the  
14 788 Slave cratonic mantle lithosphere, Voyageur kimberlite, Arctic Canada. *Chem Geol* 455:98–119  
15  
16 789 Smart KA, Tappe S, Stern RA, Webb SJ, Ashwal LD (2016) Early Archaean tectonics and  
17 790 mantle redox recorded in Witwatersrand diamonds. *Nature Geo* 9, 255–259  
18  
19 791 Smart KA, Tappe S, Woodland AB, Greyling DR, Harris C, Gussone N (2021a) Constraints on  
20 792 Archean crust recycling and the origin of mantle redox variability from the  $\delta^{44/40}\text{Ca} - \delta^{18}\text{O} - f\text{O}_2$   
21 793 signatures of cratonic eclogites. *Earth Planet Sci Lett* 556  
22  
23 794 Smart KA, Tappe S, Woodland AB, Harris C, Corcoran L, Simonetti A (2021b) Metasomatized  
24 795 eclogite xenoliths from the central Kaapvaal craton as probes of a seismic mid-lithospheric  
25 796 discontinuity. *Chem Geol* 578, 120286  
26  
27 797 Stachel T, Luth RW (2015) Diamond formation - Where, when and how? *Lithos* 220–223: 200–  
28 798 220  
29  
30 799 Stagno V (2019) Carbon, carbides, carbonates and carbonatitic melts in the Earth's interior *J*  
31 800 *Geol Soc* 176:375  
32  
33 801 Stagno V, Frost DJ, McCammon CA, Mohseni H, Fei Y (2015) The oxygen fugacity at which  
34 802 graphite or diamond forms from carbonate-bearing melts in eclogitic rocks. *Contrib Mineral*  
35 803 *Petrol* 169:16  
36  
37 804 Stagno V, Ojwang DO, McCammon CA, Frost DJ (2013) The oxidation state of the mantle and  
38 805 the extraction of carbon from Earth's interior. *Nature* 493:84–88  
39  
40 806 Sun SS, McDonough WF (1989) Chemical and isotopic systematics of oceanic basalts:  
41 807 implications for mantle composition and processes. *Geol Soc Lond Spec Publ* 42:313–345  
42  
43 808 Tappe S, Ngwenya NS, Stracke A, Romer RL, Glodny J, Schmitt AK (2023) Plume–lithosphere  
44 809 interactions and LIP-triggered climate crises constrained by the origin of Karoo lamproites.  
45 810 *Geochim Cosmo Acta* 350, 87–105  
46  
47 811 Tappe S, Foley SF, Kjarsgaard BA, Romer RL, Heaman LM, Stracke A, Jenner GA (2008)  
48 812 Between carbonatite and lamproite-Diamondiferous Torngat ultramafic lamprophyres formed by  
49 813 carbonate-fluxed melting of cratonic MARID-type metasomes. *Geochim Cosmo Acta*  
50 814 72(13):3258–3286  
51  
52  
53  
54  
55  
56  
57  
58  
59  
60  
61  
62  
63  
64  
65

1  
2  
3  
4 815 Tappe S, Pearson DG, Nowell G, Nielsen T, Milstead P, Muehlenbachs K (2011a) A fresh  
5 816 isotopic look at Greenland kimberlites: Cratonic mantle lithosphere imprint on deep source  
6 817 signal. *Earth Planet Sci Lett* 305(1-2):235–248  
7  
8  
9 818 Tappe S, Smart KA, Pearson DG, Steenfelt A, Simonetti A (2011b) Craton formation in Late  
10 819 Archean subduction zones revealed by first Greenland eclogites. *Geology*, 39(12):1103–1106  
11  
12 820 Tappe S, Smart K, Torsvik T, Massuyeau M, de Wit M (2018) Geodynamics of kimberlites on a  
13 821 cooling Earth: Clues to plate tectonic evolution and deep volatile cycles. *Earth Planet Sci Lett*  
14 822 484:1–14  
15  
16  
17 823 Tappe S, Massuyeau M, Smart KA, Woodland AB, Gussone N, Milne S, Stracke A (2021)  
18 824 Sheared Peridotite and Megacryst Formation Beneath the Kaapvaal Craton: a Snapshot of  
19 825 Tectonomagmatic Processes across the Lithosphere – Asthenosphere Transition. *J Petrol* 62(8),  
20 826 1–39  
21  
22  
23 827 Taylor LA, Neal CR (1989) Eclogites with oceanic crustal and mantle signatures from the  
24 828 Bellsbank kimberlite, South Africa, Part I: Mineralogy, Petrography and whole rock chemistry.  
25 829 *J Geol* 551–567  
26  
27  
28 830 Viljoen KS, Smith CB, Sharp ZD (1996) Stable and radiogenic isotope study of eclogite  
29 831 xenoliths from the Orapa kimberlite, Botswana. *Chem Geol* 131:235–255  
30  
31  
32 832 Wang J, Xiong X, Takahashi E, Zhang L, Li L, Liu X (2019) Oxidation State of Arc Mantle  
33 833 Revealed by Partitioning of V, Sc, and Ti Between Mantle Minerals and Basaltic Melts. *J*  
34 834 *Geophys Res Solid Earth* 124(5):4617–4638  
35  
36  
37 835 Woodland AB, Koch M (2003) Variation in oxygen fugacity with depth in the upper mantle  
38 836 beneath the Kaapvaal craton, Southern Africa. *Earth Planet Sci Lett* 214(1):295–310  
39  
40  
41 837 Yaxley GM, Berry AJ, Rosenthal A, Woodland AB, Paterson D (2017) Redox preconditioning  
42 838 deep cratonic lithosphere for kimberlite genesis: evidence from the central Slave Craton. *Sci*  
43 839 *Rep* 7:30  
44  
45  
46 840  
47

48 841 **Figure Captions**

49  
50 842 **Fig. 1.** Geological map of Wajrakarur Kimberlite Field (WKF) modified after Shaikh et al. (2017).  
51  
52  
53 843 This study deals with samples from the KL2, P9, and P10 kimberlite intrusions (highlighted by  
54  
55 844 yellow-filled circles).  
56  
57

58 845

1  
2  
3  
4  
5  
6  
7  
8  
9  
10  
11  
12  
13  
14  
15  
16  
17  
18  
19  
20  
21  
22  
23  
24  
25  
26  
27  
28  
29  
30  
31  
32  
33  
34  
35  
36  
37  
38  
39  
40  
41  
42  
43  
44  
45  
46  
47  
48  
49  
50  
51  
52  
53  
54  
55  
56  
57  
58  
59  
60  
61  
62  
63  
64  
65

846 **Fig. 2.** Scanned thin section images of KL2 eclogite nodules.

847  
848 **Fig. 3.** BSE images of KL2 eclogite nodules showing mineral grain relations and the extensive  
849 alteration of primary and matrix minerals. (a) Highly fractured garnet in sample KL2A1 showing  
850 alteration to hydro-garnet along margins. (b) Sample KL2B1 shows garnet altered to carbonate  
851 and chlorite along fractures and no preservation of omphacite and kyanite. (c) Highly fractured  
852 and altered omphacite in sample KL2A1. (d) Kyanite blades in sample KL2C3, with inclusions of  
853 garnet and omphacite, partially altered to celsian. (e) Kyanite blade in sample KL2G1 with  
854 inclusions of garnet and omphacite. (f) Interlocked kyanite blades in sample KL2F2 with an  
855 omphacite inclusion.

856  
857 **Fig. 4.** BSE images of KL2 eclogite nodules with corundum associated with kyanite (a) and a rutile  
858 bleb (b).

859  
860 **Fig. 5.** Major and trace element (REE) plots for garnet (a, b, c) and clinopyroxene (b, d) from KL2  
861 eclogites. The fields in figure (a) are after Aulbach and Jacob (2016) and in (b) after McCandless  
862 and Gurney (1989). The A, B, and C fields in the inset figure are after Taylor and Neal (1989).

863  
864 **Fig. 6.** Cr<sub>2</sub>O<sub>3</sub> versus CaO wt.% plot (a) and chondrite normalized REE plot (b; after (Sun and  
865 McDonough, 1989) for garnet xenocrysts from P9 and P10 intrusions of the WKF.

866  
867 **Fig. 7.** Reconstructed bulk-rock composition diagrams for classifying KL2 eclogite nodules. Fields  
868 in figures (a) and (b) are after Aulbach and Jacob (2016), and primitive mantle normalization in

1  
2  
3  
4  
5  
6  
7  
8  
9  
10  
11  
12  
13  
14  
15  
16  
17  
18  
19  
20  
21  
22  
23  
24  
25  
26  
27  
28  
29  
30  
31  
32  
33  
34  
35  
36  
37  
38  
39  
40  
41  
42  
43  
44  
45  
46  
47  
48  
49  
50  
51  
52  
53  
54  
55  
56  
57  
58  
59  
60  
61  
62  
63  
64  
65

869 (c) is after (Sun and McDonough, 1989). Published KL2 eclogite data are from Dongre et al.  
870 (2015). Symbol sizes in (a) and (b) are larger than the  $2\sigma$  uncertainties.

871  
**Fig. 8.** Trace element variations diagrams based on reconstructed bulk-rock compositions for  
872 eclogite nodules. Note that reconstructed bulk-rock compositions indicate  $fO_2$  values below FMQ-  
873 2. Figures (a) Ti vs.  $Vi/Ti \cdot 100$ , (b) Ce/Yb vs. Lu/Gd, and (c) MgO vs. V/Sc are after Wang et al.  
874 (2019) and Aulbach and Viljoen (2015). Symbol sizes are larger than the  $2\sigma$  uncertainties.

875  
876  
**Fig. 9.** Projections of equilibration temperatures calculated for KL2 eclogite nodules (a; after  
877 Krogh, 1988) and P9-P10 garnet xenocrysts (b; after Canil, 1999). Published KL2 data from Patel  
878 et al. (2006) and Dongre et al. (2015). The conductive model geotherm (after Hasterok and  
879 Chapman, 2011) for the Wajrakarur lithosphere is from Shaikh et al. (2020). The diamond-graphite  
880 transition is after Day et al. (2012).

881  
882  
**Fig. 10.**  $\Delta \log fO_2$  (FMQ) values calculated for KL2 eclogitic garnets (after Stagno et al., 2015) and  
883 P9 and P10 peridotitic garnet xenocrysts (after Stagno et al., 2013) plotted against the estimated  
884 pressure. The field for Kaapvaal peridotites is after Woodland and Koch (2003) and Creighton et  
885 al. (2009), enriched peridotites from Slave craton after Yaxley et al. (2017) and graphite-diamond-  
886 carbonate melt transition lines after Stagno et al. (2015). Updated Kaapvaal data (small open  
887 circles) are after Tappe et al. (2021).

888  
889  
**Fig. 11.**  $\Delta \log fO_2$  (FMQ) versus MgO and CaO (in wt%) for KL2 eclogitic garnets from Wajrakarur  
890 kimberlites.

1  
2  
3  
4  
5  
6  
7  
8  
9  
10  
11  
12  
13  
14  
15  
16  
17  
18  
19  
20  
21  
22  
23  
24  
25  
26  
27  
28  
29  
30  
31  
32  
33  
34  
35  
36  
37  
38  
39  
40  
41  
42  
43  
44  
45  
46  
47  
48  
49  
50  
51  
52  
53  
54  
55  
56  
57  
58  
59  
60  
61  
62  
63  
64  
65

892

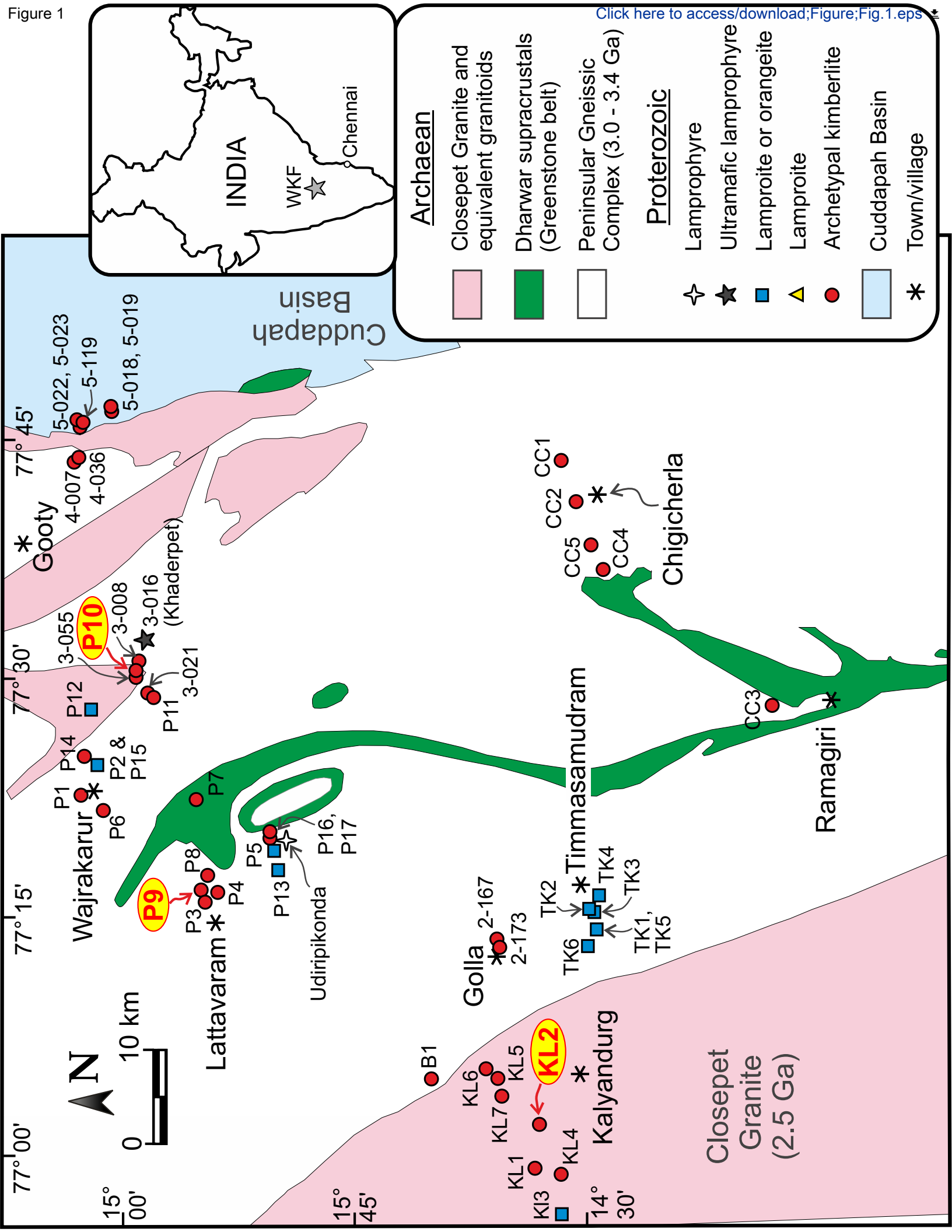
893

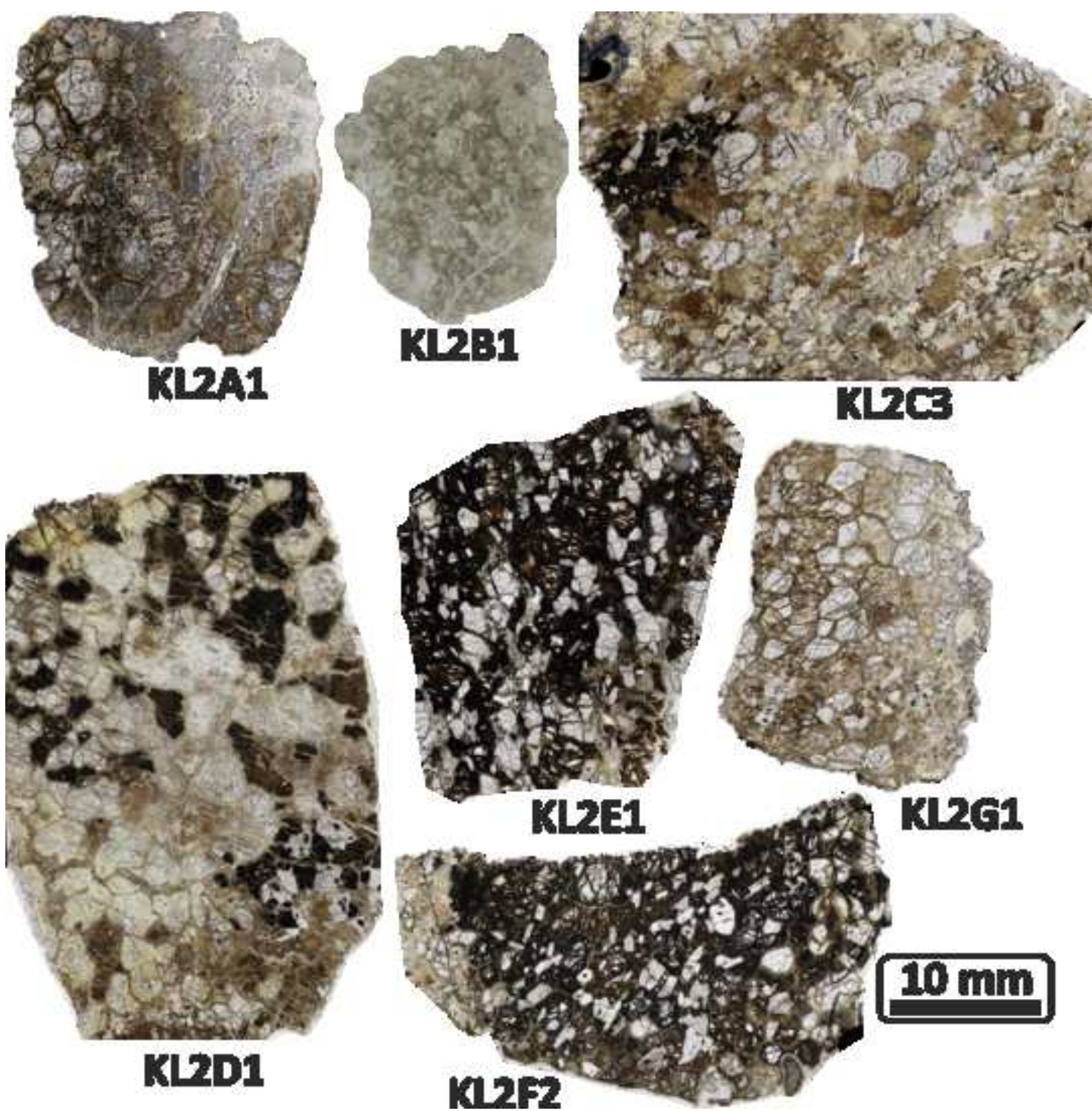
894

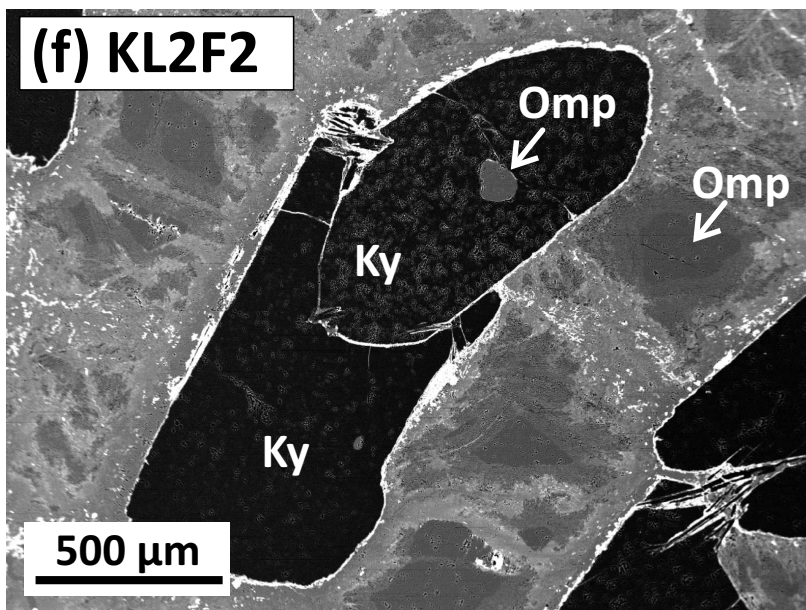
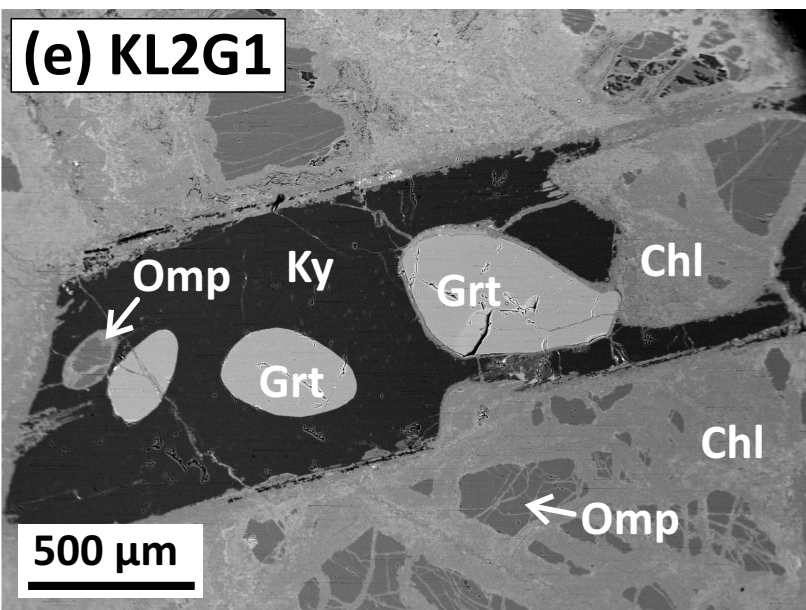
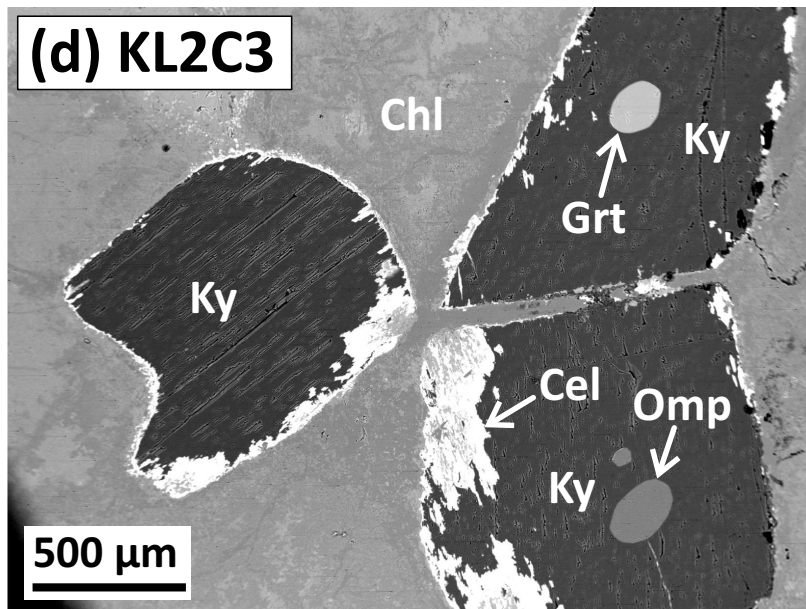
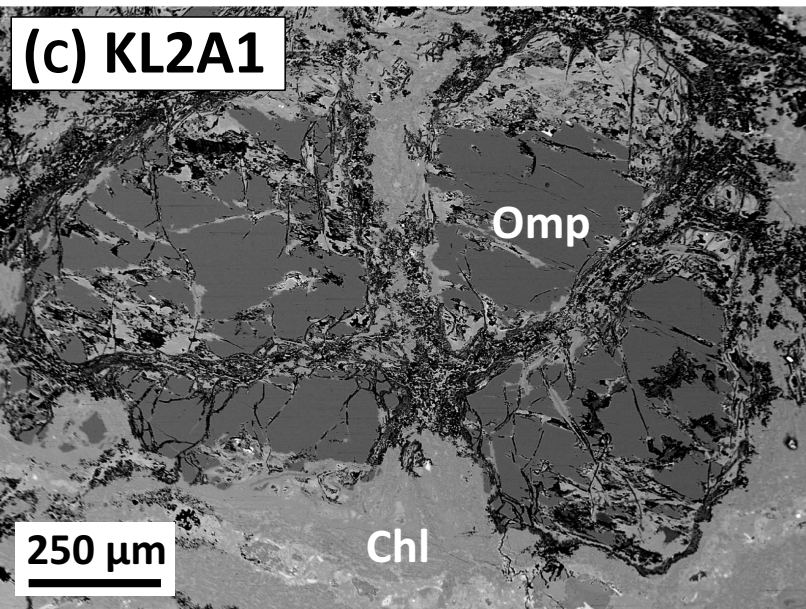
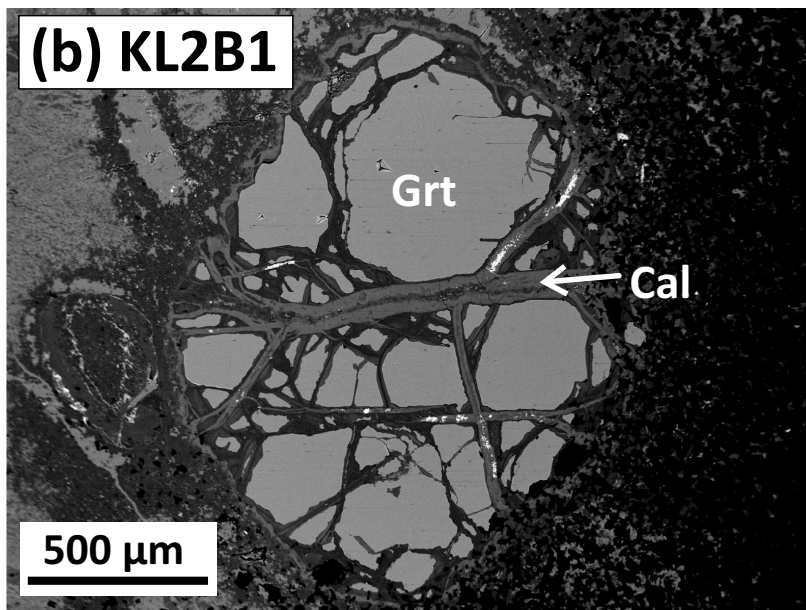
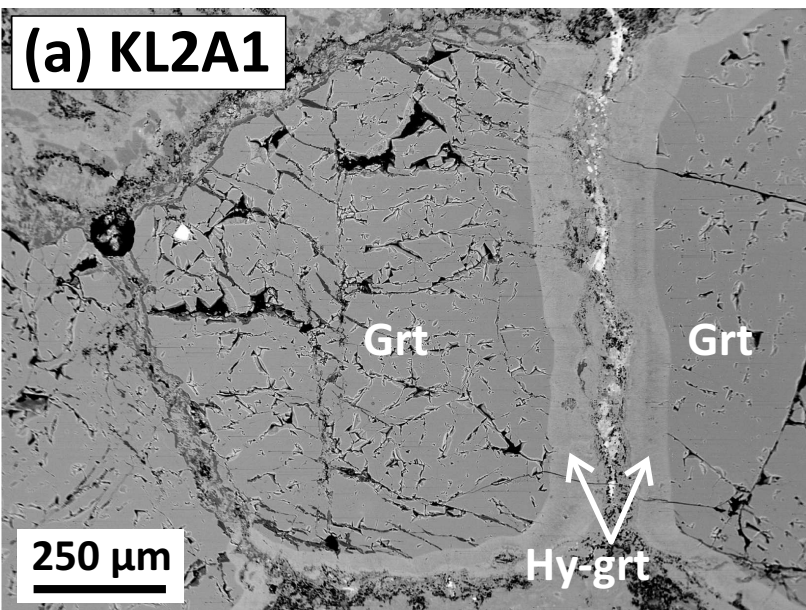
895

**Fig. 12.**  $Fe^{3+}/\Sigma Fe$  ratios plotted against  $TiO_2$  (a), Y (b), Zr (c), and V (d) for peridotitic garnet xenocrysts from the P9 and P10 kimberlite bodies at Wajrakarur. Kaapvaal craton xenolith data are taken from Creighton et al. (2009).

Figure 1







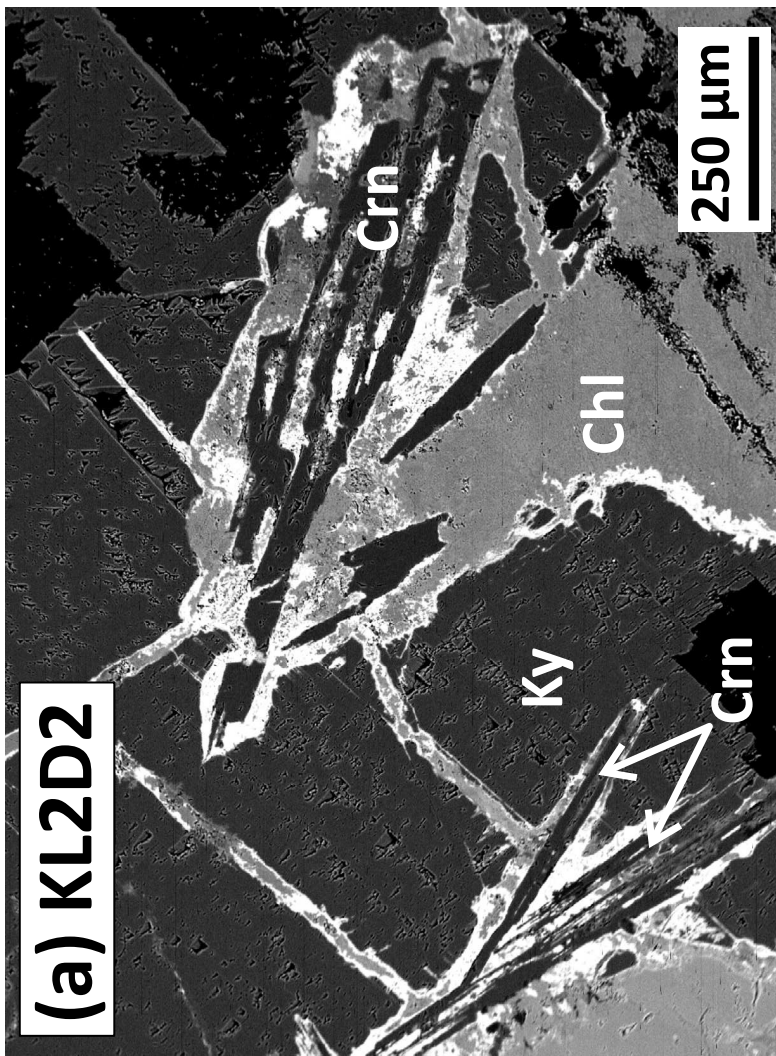
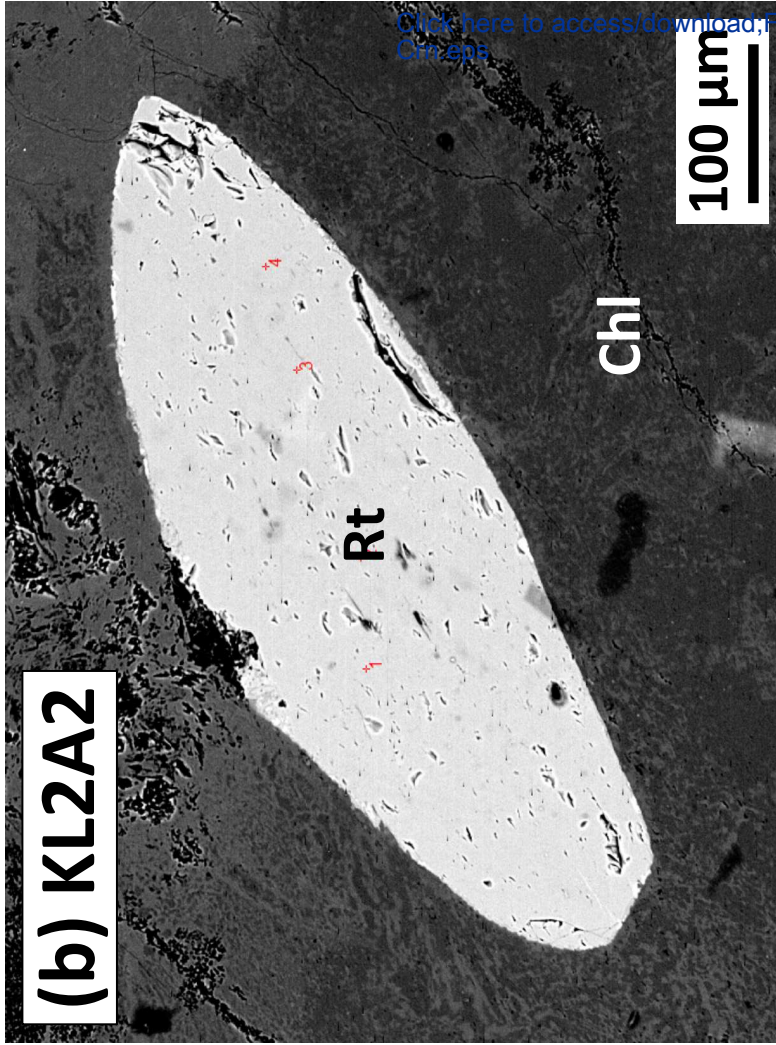
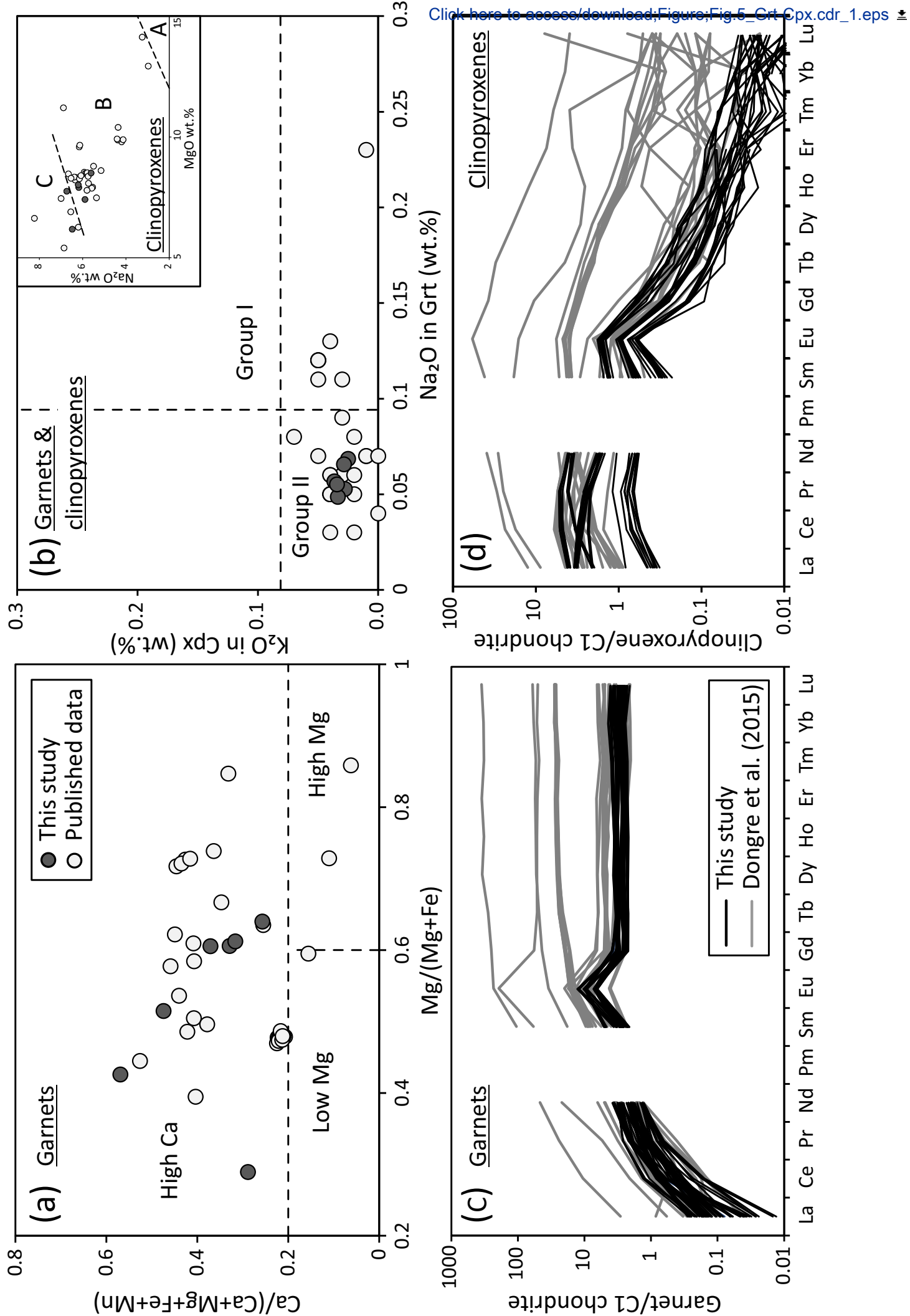


Figure 5



[Click here to access/download;Figure;Fig\\_5\\_Grt\\_Cpx.cdr\\_1.eps](#)

Figure 6

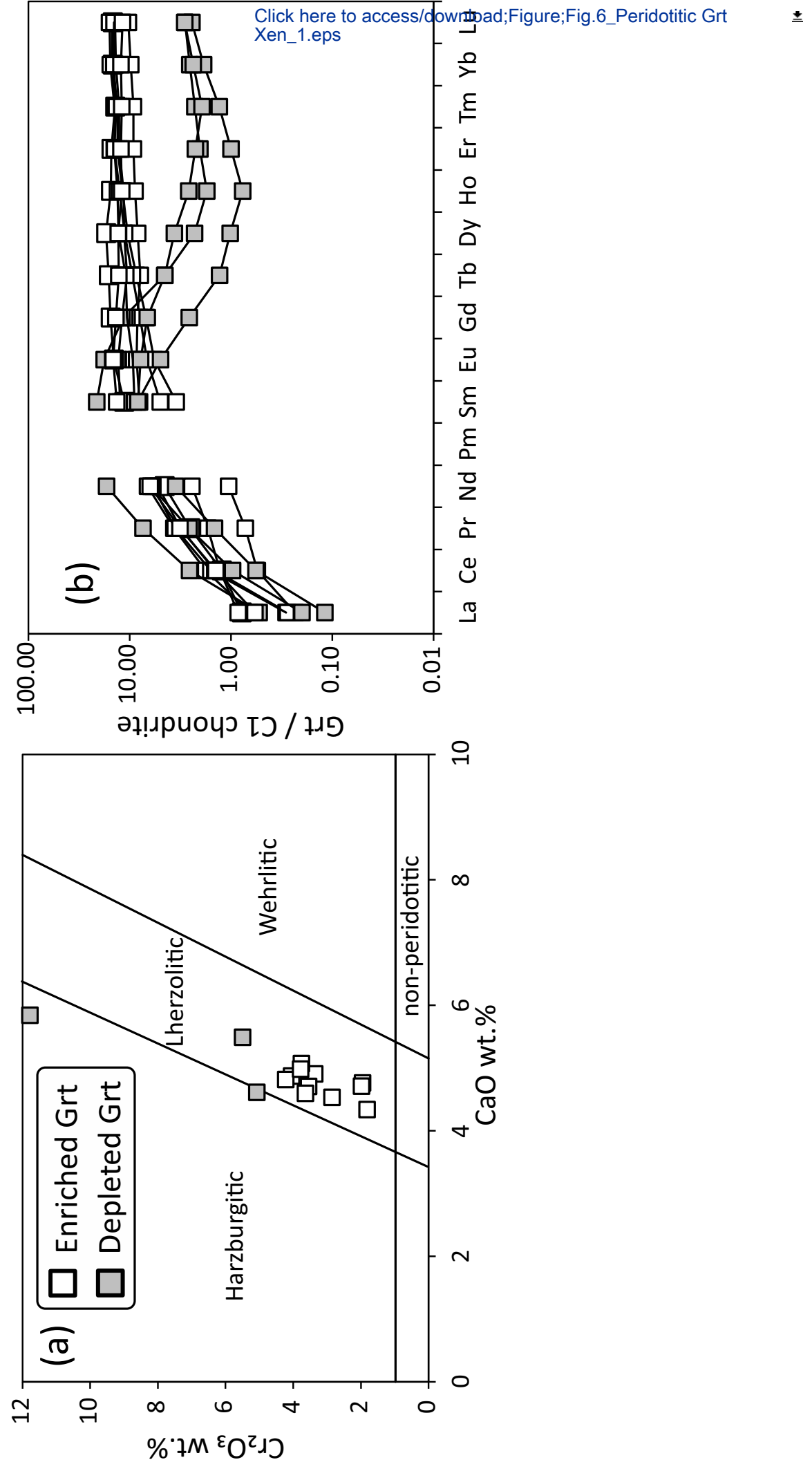


Figure 7

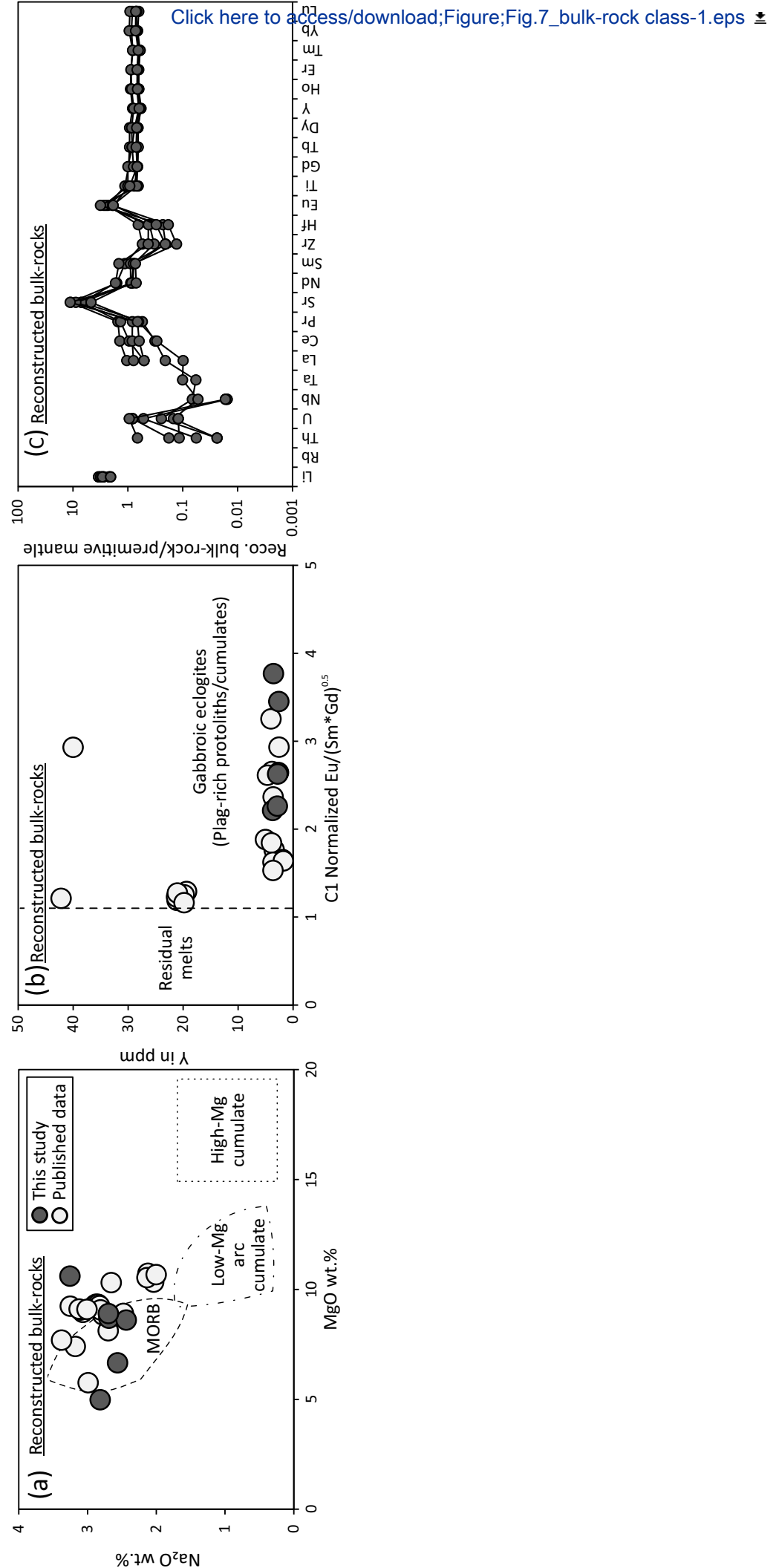


Figure 8

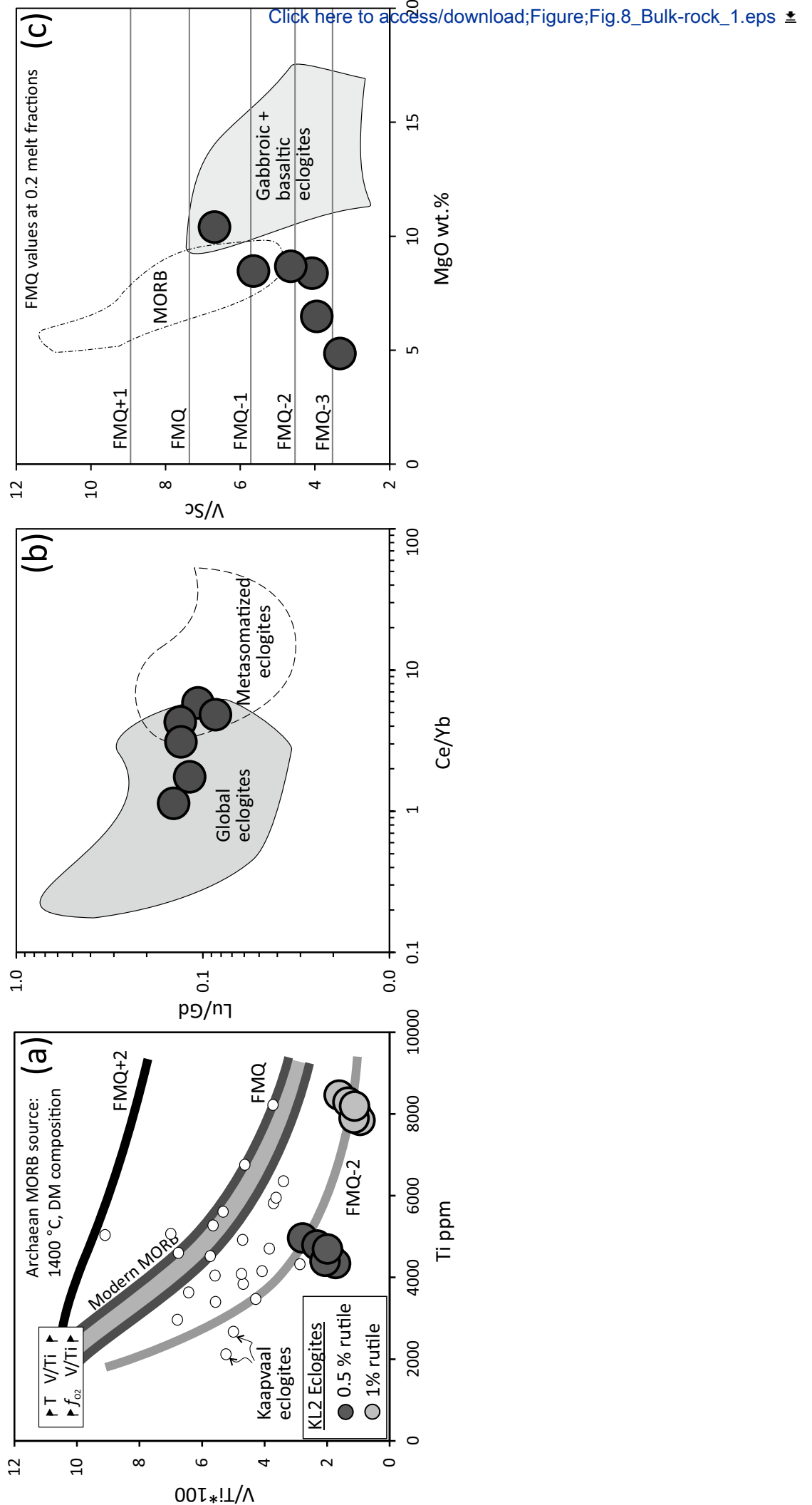


Figure 9

Krogh88 Temperature (°C)

Pressure (kbar)

20 30 40 50 60 70

1400 1200 1000 800 600

(a)

Adiabat

KL2 Eclogites  
● This study  
○ Published data

Graphite  
Diamond

$1\sigma$

(b)

Adiabat

40 mW/m<sup>2</sup>

Garnet xenocrysts

Graphite  
Diamond

$1\sigma$

Ni-in-Grt Temperature (°C)

800 1000 1200 1400

Pressure (kbar)

20 30 40 50 60 70

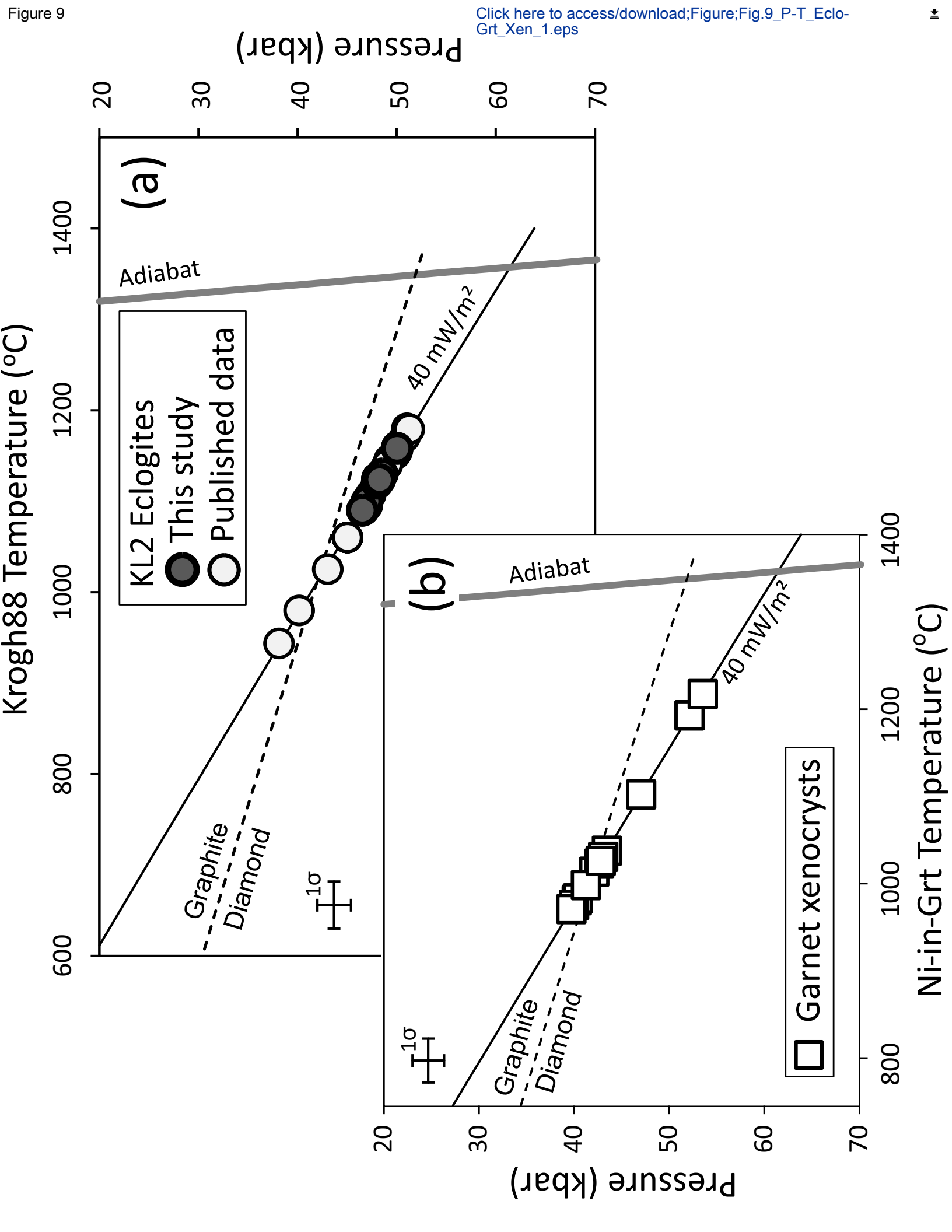
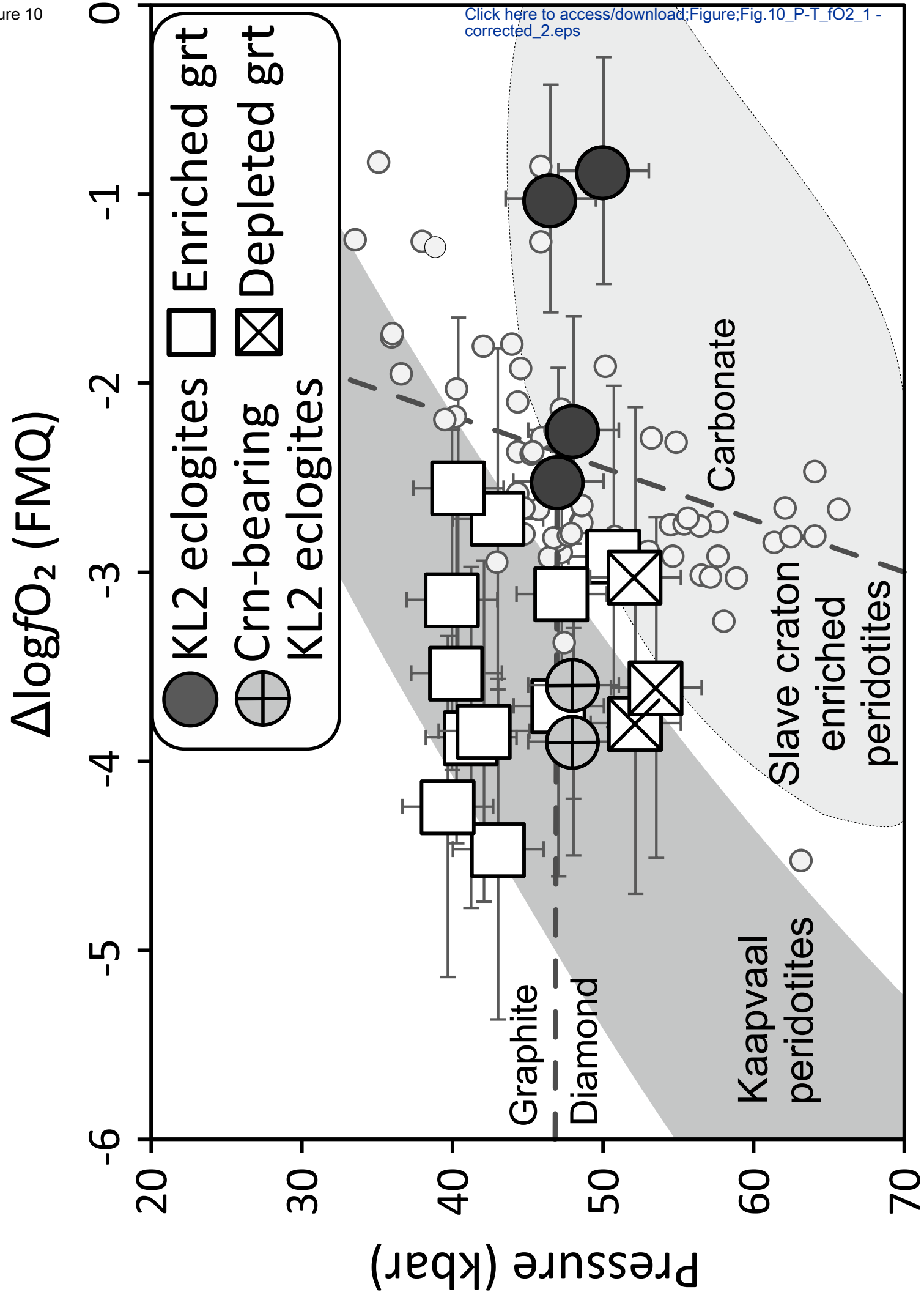


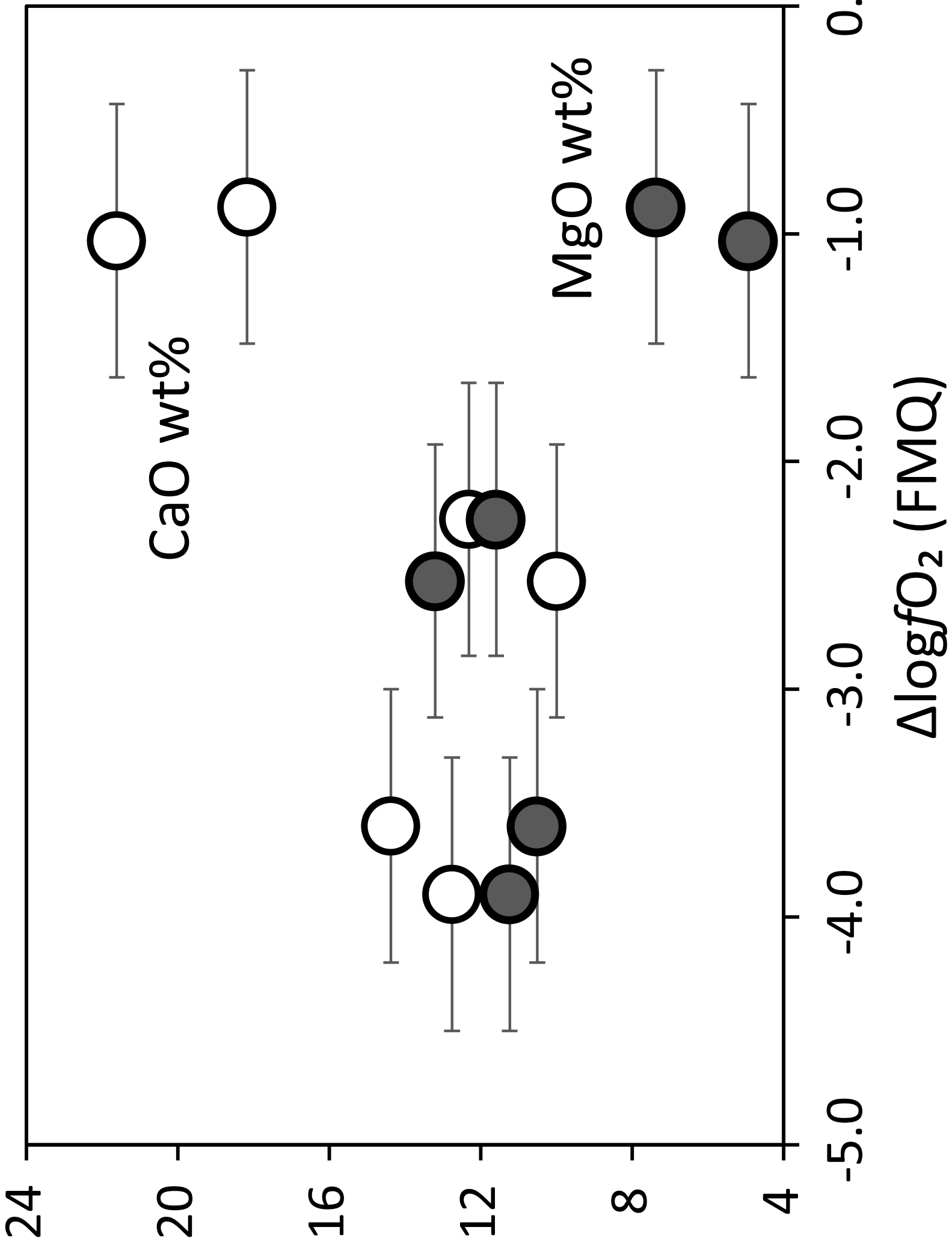
Figure 10



[Click here to access/download:Figure, Fig.10\\_P-T\\_fO2\\_1 - corrected\\_2.eps](#)



Figure 11



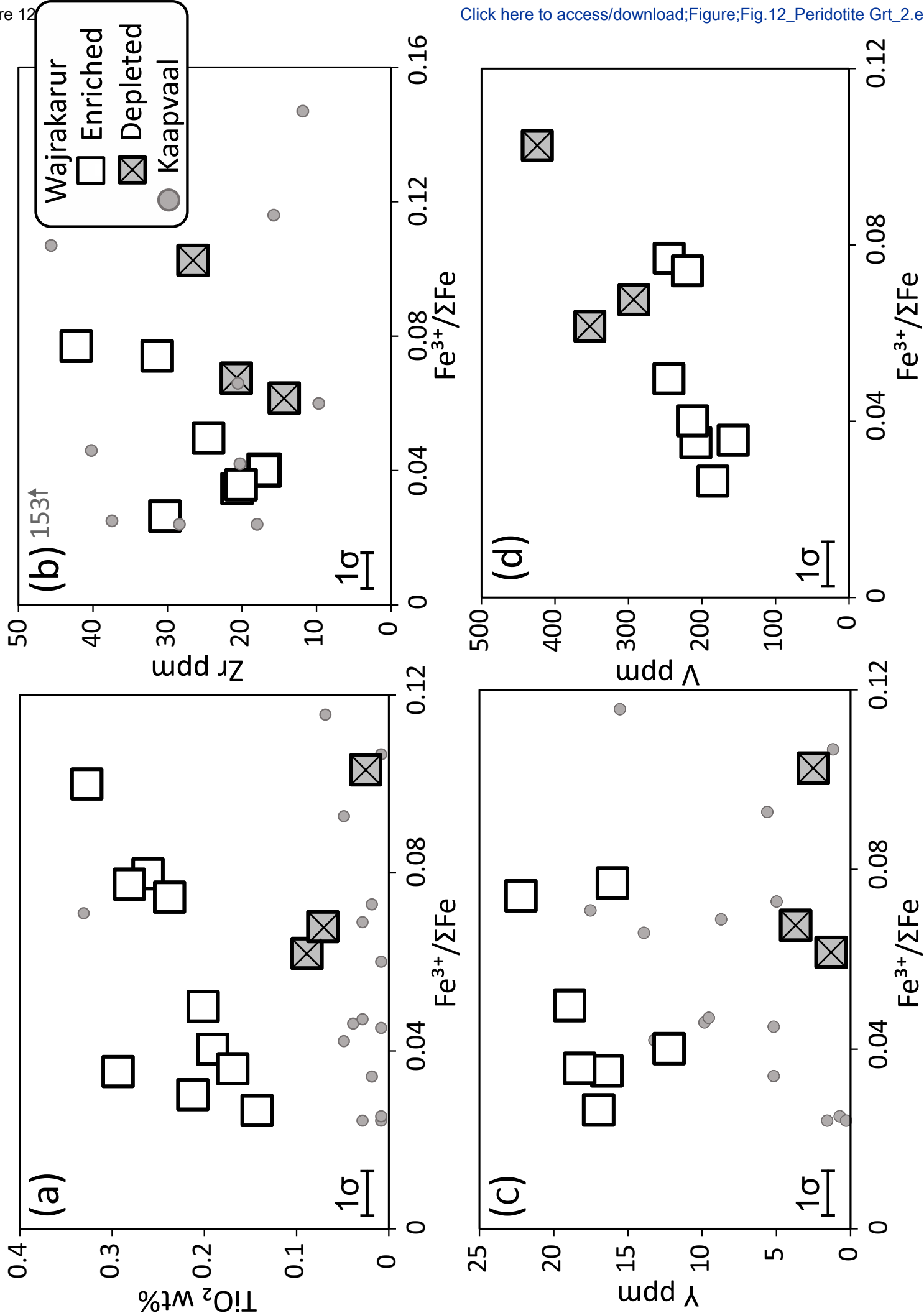


**Table 1.** Mineral assemblages, temperature, pressure, garnet  $\text{Fe}^{3+}/\Sigma\text{Fe}$ , and oxygen fugacity of the KL2 eclogites.

Sample	Minerals	$T_{\text{KR88}}$ ( $^{\circ}\text{C}$ ) <sup>s</sup>	$P_{\text{KR88}}$ (GPa) <sup>ss</sup>	Grt $\text{Fe}^{3+}/\Sigma\text{Fe}$ <sup>v</sup>	$\log\text{O}_2$ ( $\Delta\text{FMQ}$ ) <sup>vw</sup>
KL2A	grt, omp, rt	1100	4.7	0.02	-2.5
KL2C	grt, omp, ky	1160	5.0	0.05	-0.9
KL2D	grt, omp, ky, crn	1120	4.8	0.02	-3.9
KL2E	grt, omp, ky	1090	4.7	0.05	-1.0
KL2F	grt, omp, ky, crn	1130	4.8	0.02	-3.6
KL2G	grt, omp, ky	1125	4.8	0.02	-2.3

<sup>s</sup>Temperatures ( $T_{\text{KR88}}$ ) were calculated iteratively using temperatures obtained from the Krogh (1988) thermometer with pressures ( $P_{\text{HC40}}$ )<sup>ss</sup> calculated from the 40 mW/m<sup>2</sup> conductive geotherm from Hasterok and Chapman (2011). The discrepancies for  $T_{\text{KR88}}$  are mostly within  $\pm 50$   $^{\circ}\text{C}$ ; which poses an uncertainty in iteratively calculated  $P_{\text{HC40}}$  around  $\pm 0.3$  GPa.

<sup>v</sup> $\text{Fe}^{3+}/\Sigma\text{Fe}$  measured using the EPMA flank method after Höfer et al. (1994) and Höfer and Brey (2007) with an uncertainty of  $\pm 0.01$ .

<sup>vw</sup>Oxygen fugacities were calculated using the oxybarometer of Stagno et al. (2015) with  $T_{\text{KR88}}-P_{\text{HC40}}$ . The uncertainties for  $f\text{O}_2$  are mostly  $\sim 0.6$  log units.

**Table 2.** Temperature, pressure, and  $\text{Fe}^{3+}/\Sigma\text{Fe}$  in garnet,  $\text{Fe}\# \text{Opx}^{\psi} = \text{Fe}^{2+}/(\text{Fe}^{2+}+\text{Mg})$  in orthopyroxene,  $\text{Fe}\# \text{Ol}^{\psi\psi} = \text{Fe}^{2+}/(\text{Fe}^{2+}+\text{Mg})$  in olivine and oxygen fugacity of the peridotitic garnet xenocrysts from Wajrakarur.

Sample	$T_{\text{C99}}$ ( $^{\circ}\text{C}$ ) <sup>§</sup>	$P_{\text{HC40}}$ (GPa) <sup>§§</sup>	Grt $\text{Fe}^{3+}/\Sigma\text{Fe}^{\psi}$	$\text{Fe}\# \text{Opx}^{\psi\psi}$	$\text{Fe}\# \text{Ol}^{\Phi}$	$\log\text{O}_2$ ( $\Delta\text{FMQ}$ ) <sup>ΦΦ</sup>
P9G47C	1025	4.3	0.03	0.040	0.081	-4.5
P9G51A	1037	5.1	0.10	0.039	0.077	-2.9
P9G52A	1023	4.3	0.08	0.038	0.076	-2.7
P9G52C	1102	4.7	0.08	0.038	0.076	-3.1
P10G3D	1030	4.1	0.04	0.040	0.081	-3.9
P10G10B	980	4.0	0.04	0.032	0.067	-3.5
P10G10D	1192	5.2	0.10	0.035	0.068	-3.0
P10G13A	983	4.0	0.07	0.035	0.074	-2.6
P10G13B	1013	4.2	0.04	0.041	0.082	-3.8
P10G13C	975	4.0	0.05	0.032	0.067	-3.1
P10G13D	1193	5.2	0.06	0.037	0.070	-3.8
P10G19C	1217	5.3	0.07	0.038	0.070	-3.6
P10G19D	970	4.0	0.03	0.033	0.069	-4.2
P10G28D	998	4.7	0.05	0.033	0.063	-3.7

<sup>§</sup>Temperatures ( $T_{\text{C99}}$ ) calculated iteratively using temperatures obtained from the Canil (1999) thermometer with pressures ( $P_{\text{HC40}}$ )<sup>§§</sup> calculated from the 40 mW/m<sup>2</sup> conductive geotherm from Hasterok and Chapman (2011). The discrepancies for  $T_{\text{C99}}$  are mostly within  $\pm 50$   $^{\circ}\text{C}$ ; which poses an uncertainty in iteratively calculated  $P_{\text{HC40}}$  around  $\pm 0.3$  GPa.

<sup>ψ</sup> $\text{Fe}^{3+}/\Sigma\text{Fe}$  measured using the EPMA flank method after Höfer et al. (1994) and Höfer and Brey (2007). The uncertainty is  $\pm 0.01$ .

<sup>ψψ</sup> $\text{Fe}\#$  in orthopyroxene in equilibrium with garnet calculated using Equation 7 in Ryan et al. (1996) and Equation 11 in Harley (1984). The assumed uncertainty is below 5% (Gaul et al., 2000; Ryan et al., 1996).

<sup>Φ</sup>Olivine in equilibrium with garnet calculated from the garnet-olivine thermometer of O'Neill and Wood (1979) using the algorithm by Gaul et al. (2000). The assumed uncertainty is below 5% (Gaul et al., 2000; Ryan et al., 1996).

<sup>ΦΦ</sup>Oxygen fugacities calculated using the oxybarometer of Stagno et al. (2013). The uncertainty is mostly  $\sim 0.9$  log units.

[Click here to view linked References](#)

# Redox state of the Dharwar craton root as inferred from eclogite and peridotite sourced mantle cargo, with implications for kimberlite and lamproite magma formation

Azhar M. Shaikh<sup>1,2,3\*</sup>, Yannick Bussweiler<sup>4</sup>, Fanus Viljoen<sup>2</sup>, Robert Bolhar<sup>3</sup>, S. Ravi<sup>5</sup>, Dominik C. Hezel<sup>6</sup>, Henriëtte Ueckermann<sup>2</sup>, Sebastian Tappe<sup>2,7</sup>

## Appendix 1

Details of the analytical techniques, (a) EPMA and (b) LA-ICP-MS

(a) EPMA calibration settings for major elements of olivine

Major elements were measured at an acceleration voltage of 20 kV and a beam current of 20 nA with a beam diameter of 1  $\mu\text{m}$ . Data was reduced by using the X-PHI method (Merlet, 1992, 1994). The following calibration was used.

Table 1. Calibration settings microprobe measurements

Element and line	Crystal	Peak Time (sec)	Background (-ve)	Background (+ve)	Standard	Standard intensity (cps/nA)
Na $K_{\alpha}$	TAP	40	-1200	660	Jadeite	34
Mg $K_{\alpha}$	TAP	20	-1050	1000	Olivine	120
Al $K_{\alpha}$	TAP	34	-750	1000	Almandine	287
Si $K_{\alpha}$	TAP	26	-1760	2250	Diopside	287
K $K_{\alpha}$	PET	24	-1100	1000	Orthoclase	39
Ca $K_{\alpha}$	PET	20	-700	760	Wollastonite	99
Ti $K_{\alpha}$	PET	16	-500	700	TiO <sub>2</sub>	124
Cr $K_{\alpha}$	LLIF	18	-1000	900	CrO	164
Mn $K_{\alpha}$	LLIF	16	-1200	1400	Rhodonite	127

Fe <i>Ka</i>	LLIF	14	-880	800	Hematite	142
Ni <i>Ka</i>	LLIF	12	-1600	1000	NiO	130

(Pulse height analysis mode was integral. cps/nA = counts per second per nano ampere)

Counting time for the background was half of the peak time.

(b) LA-ICP-MS: trace elements in clinopyroxene and garnet

Trace elements of clinopyroxene, garnet and kyanite in eclogite nodules were measured at Spectrum, University of Johannesburg, using a 193 nm ArF RESOLUTION SE excimer laser system (Australian Scientific Instruments, Fyshwick) enabled with a Thermo Scientific iCAP RQ ICPMS. Laser sampling was done with the SE155 dual-volume ablation cell (Laurin Technic, Canberra, Australia) that delivers the ablated material in a He-Ar gas mixture. The gas settings for ICP-MS were 14 L/min cooling gas, 0.80 L/min auxiliary gas and 1.2 L/min nebulizer gas with a flow rate of He laser carrier gas at 0.35 L/min, and a minor amount of N<sub>2</sub> additional gas at a flow rate of 0.001 L/min. Laser spots were of 80 µm diameter with 6 mJ laser energy at 25% attenuation to obtain an on-sample fluence of 2 J/cm<sup>2</sup>. The repetition rate was 10 Hz. The grain surface before each spot analysis by two laser pulses. The background signal was measured for 15 seconds at the beginning of each measurement and ablation signal was measured for 50 to 60 seconds. Tuning of the LA-ICPMS system for sensitivity and interferences was done using line scans on NIST 612 glass for <sup>6</sup>Li, <sup>59</sup>Co and <sup>208</sup>Pb. Samples were measured using standard bracketing, with <sup>29</sup>Si in NIST612 used as a calibration standard. The primary standard (NIST612) was analyzed twice at the start and twice at the end of each experiment or sequence, as well as once after every 25 sample measurements. Two to four secondary standard measurements were also included at these 25 sample measurement intervals for quality control purpose. Raw data were processed using the iCAP Qtegra software version 2.10.3324.62. The following masses were measured: 7Li, 23Na, 24Mg, 25Mg, 26Mg, 27Al, 29Si, 31P, 43Ca, 45Sc, 47Ti, 48Ca, 49Ti, 51V, 53Cr, 55Mn, 57Fe, 59Co, 60Ni, 63Cu, 65Cu, 66Zn, 68Zn, 69Ga, 71Ga, 75As, 85Rb, 88Sr, 89Y, 90Zr, 93Nb, 96Mo, 118Sn, 133Cs, 137Ba, 139La, 140Ce, 141Pr, 146Nd, 147Sm, 153Eu, 157Gd, 159Tb, 163Dy, 165Ho, 166Er, 169Tm, 172Yb, 175Lu, 178Hf, 181Ta, 182W, 208Pb, 232Th, 238U. Isotope <sup>29</sup>Si was used for internal standardization. The dwell times of all isotopes are provided in Table 2 given below. The primary standard used for calibration was NIST 612 (Jochum et al., 2011) and secondary standards used to evaluate the accuracy and precision were USGS natural glasses BHVO2G, BCR-2G and GHR1 (Gao et al., 2002) and MongOl-sh11-2 (Batanova et al., 2019).

Most of the trace element measurements were comparable within 10%, while some were within 15%, compared to accepted values (Supp. Table 1). Data reduction was performed using the Glitter software version 4.4.4 (<http://www.glitter-gemoc.com/>).

Table 2. Dwell times of isotopes measured during the LA-ICPMS analysis.

Identifier	Dwell time (s)	Channels	Spacing (u)	Resolution
7Li	0.03	1	0.1	Normal
23Na	0.01	1	0.1	Normal
24Mg	0.01	1	0.1	Normal
25Mg	0.01	1	0.1	Normal
26Mg	0.01	1	0.1	Normal
27Al	0.01	1	0.1	Normal
29Si	0.01	1	0.1	Normal
31P	0.01	1	0.1	Normal
43Ca	0.01	1	0.1	Normal
45Sc	0.03	1	0.1	Normal
47Ti	0.01	1	0.1	Normal
48Ca	0.01	1	0.1	Normal
49Ti	0.01	1	0.1	Normal
51V	0.01	1	0.1	Normal
53Cr	0.01	1	0.1	Normal
55Mn	0.01	1	0.1	Normal
57Fe	0.01	1	0.1	Normal
59Co	0.01	1	0.1	Normal
60Ni	0.03	1	0.1	Normal
63Cu	0.01	1	0.1	Normal
65Cu	0.03	1	0.1	Normal
66Zn	0.03	1	0.1	Normal
68Zn	0.03	1	0.1	Normal
69Ga	0.03	1	0.1	Normal
71Ga	0.01	1	0.1	Normal
75As	0.01	1	0.1	Normal
85Rb	0.01	1	0.1	Normal
88Sr	0.03	1	0.1	Normal
89Y	0.03	1	0.1	Normal
90Zr	0.03	1	0.1	Normal
93Nb	0.03	1	0.1	Normal
96Mo	0.01	1	0.1	Normal
118Sn	0.01	1	0.1	Normal

133Cs	0.02	1	0.1	Normal
137Ba	0.01	1	0.1	Normal
139La	0.03	1	0.1	Normal
140Ce	0.03	1	0.1	Normal
141Pr	0.03	1	0.1	Normal
146Nd	0.01	1	0.1	Normal
147Sm	0.02	1	0.1	Normal
153Eu	0.03	1	0.1	Normal
157Gd	0.03	1	0.1	Normal
159Tb	0.03	1	0.1	Normal
163Dy	0.03	1	0.1	Normal
165Ho	0.03	1	0.1	Normal
166Er	0.03	1	0.1	Normal
169Tm	0.03	1	0.1	Normal
172Yb	0.03	1	0.1	Normal
175Lu	0.03	1	0.1	Normal
178Hf	0.02	1	0.1	Normal
181Ta	0.03	1	0.1	Normal
182W	0.01	1	0.1	Normal
208Pb	0.01	1	0.1	Normal
232Th	0.03	1	0.1	Normal
238U	0.03	1	0.1	Normal

## References

Batanova, V. G., Thompson, J. M., Danyushevsky, L. V., Portnyagin, M. V., Garbe-Schönberg, D., Hauri, E., Kimura, J. I., Chang, Q., Senda, R., Goemann, K., Chauvel, C., Campillo, S., Ionov, D. A., & Sobolev, A. V. (2019). New Olivine Reference Material for In Situ Microanalysis. *Geostandards and Geoanalytical Research*, 43(3), 453–473.

Gao S, Liu X, Yuan H, Hattendorf B, Günther D, Chen L, Hu S (2002) Determination of forty two major and trace elements in USGS and NIST SRM glasses by laser ablation inductively coupled plasma mass spectro-metry. *Geostand Newslet* 26(2):181-196

Jochum KP, Weis U, Stoll B, Kuzmin D, Yang Q, Raczek I, Jacob DE, Stracke A, Birbaum K, Frick DA, Günther D, Enzweiler J (2011) Determination of reference values for NIST SRM 610–617 glasses following ISO guidelines. *Geostand Geoanal Res* 35(4), 397-429

Merlet C (1992) Quantitative Electron Probe Microanalysis: New Accurate  $\Phi$  ( $\rho z$ ) Description. In: Boekstein, A., Pavićević, M.K. (Eds.), *Electron Microbeam Analysis*. Springer, Vienna pp 107–115

Merlet C (1994) An accurate computer correction program for quantitative electron probe microanalysis. *Microchim Acta* 114:363–376

[Click here to view linked References](#)

1 **Redox state of the Dharwar craton root as inferred from ~~mantle~~ eclogite**  
2 **~~xenoliths~~ and peridotite sourced mantle ~~cargoperidotitic garnet xenocrysts~~,**  
3 **with implications for kimberlite and lamproite magma formation**

Formatted: Strikethrough

4  
5 Azhar M. Shaikh<sup>1,2,3\*</sup>, Yannick Bussweiler<sup>4</sup>, Fanus Viljoen<sup>2</sup>, Robert Bolhar<sup>3</sup>, S. Ravi<sup>5</sup>, Dominik  
6 C. Hezel<sup>6</sup>, Henriëtte Ueckermann<sup>2</sup>, Sebastian Tappe<sup>2,7</sup>

7  
8  
9 <sup>1</sup> Department of Earth and Environmental Sciences, Indian Institute of Science Education and  
10 Research Berhampur, India

11 <sup>2</sup> Department of Geology, University of Johannesburg, Auckland Park, South Africa

12 <sup>3</sup> School of Geosciences, University of the Witwatersrand, Braamfontein, South Africa

13 <sup>4</sup> Institute for Geology and Mineralogy, University of Cologne, Germany

14 <sup>5</sup> Geological Survey of India, Bengaluru, India

15 <sup>6</sup> Institut für Geowissenschaften, Goethe-Universität Frankfurt, Frankfurt am Main, Germany

16 <sup>7</sup> Department of Geosciences, UiT The Arctic University of Norway, Tromsø, Norway

17  
18 \*Corresponding author: Telephone: +918879524349.

19 E-mail: [azharms@iiserbpr.ac.in](mailto:azharms@iiserbpr.ac.in), ORCID ID: [0000-0002-7327-5414](https://orcid.org/0000-0002-7327-5414)

20  
21 **ABSTRACT**

22 Despite over 400 occurrences of kimberlites and related rocks in India, mantle-derived xenoliths  
23 are known only from a few occurrences. This paucity of mantle-derived xenoliths in Indian

24 kimberlites has hampered investigations of the subcontinental lithospheric mantle (SCLM). Using  
25 a valuable selection of the rare xenolith inventory, we here report  $\text{Fe}^{3+}/\Sigma\text{Fe}$  measurements for  
26 garnets using the electron microprobe (EPMA) flank method, targeting six mantle eclogite  
27 xenoliths (KL2 pipe) and fourteen peridotitic garnet xenocrysts (P9 and P10 hypabyssal intrusions)  
28 from the Wajrakarur kimberlite field (WKF) on the Eastern Dharwar craton (EDC). These data  
29 provide some of the first direct constraints on the oxygen fugacity ( $f\text{O}_2$ ) of the lithospheric mantle  
30 beneath the Indian subcontinent.

31 The measured  $\text{Fe}^{3+}/\Sigma\text{Fe}$  ratios vary between 0.02 and 0.05 ( $\pm 0.01$ ) for the eclogite xenoliths  
32 and between 0.02 and 0.10 ( $\pm 0.01$ ) for the peridotitic garnets. Calculated  $\Delta\log f\text{O}_2$  values for the  
33 KL2 eclogites show a wide range from FMQ-3.9 to FMQ-0.9 ( $\pm 0.6$ ), straddling the boundary  
34 between the diamond and carbonate stability fields. In terms of redox compositions, it appears that  
35 the KL2 eclogites are able to host diamond, which is consistent with the diamondiferous nature of  
36 this particular WKF locality and the presence of eclogitic garnet inclusions in diamonds from the  
37 nearby TK4 kimberlite body.

38 The peridotitic garnet xenocrysts from the P9 and P10 kimberlite bodies, which were  
39 entrained between ~125 and 170 km depth, reveal  $\Delta\log f\text{O}_2$  values between FMQ-4.5 and FMQ-  
40 2.6 ( $\pm 0.9$ ). Garnet xenocrysts with 'normal' REE patterns exhibit higher  $\text{Fe}^{3+}/\Sigma\text{Fe}$  ratios compared  
41 to garnets with 'sinusoidal' REE patterns. Importantly, the  $\text{Fe}^{3+}/\Sigma\text{Fe}$  ratios of garnet xenocrysts  
42 with 'normal' REE patterns (~125–160 km depth) correlate with metasomatic Ti-Y-Zr-V  
43 enrichment, which suggests metasomatism-driven oxidation of the cratonic mantle at mid-  
44 lithospheric depths. Such melt-related mantle metasomatism was probably diamond-destructive  
45 within the otherwise diamond-fertile lithospheric keel.

46 The observed wide range of  $\Delta \log fO_2$  values for the Dharwar cratonic mantle lithosphere  
47 allows for stabilization of various metasomatic phases (e.g., amphiboles, micas, carbonates) that  
48 may have formed (or concentrated in) distinctly different metasome assemblages within the  
49 continental root that underpins Peninsular India. Changing the relative contributions from such  
50 highly diverse volatile-rich metasomes may explain the close close spatiotemporal association of  
51 kimberlites and various diamond-bearing potassic magma types such as orangeites, ultramafic  
52 lamprophyres and lamproites, a scenario that is influenced by the redox composition of the  
53 Dharwar craton root.

54  
55 *Keywords: Continental lithospheric mantle, Eclogite, Garnet, Oxygen fugacity, Mantle redox,*  
56 *Wajrakarur kimberlites, Southern India*

57

## 58 **Introduction**

59 Oxygen fugacity ( $fO_2$ ) has significant implications for the speciation of CHONS-volatiles and the  
60 stability of diamond/graphite in the Earth's mantle (Stagno, 2019). Oxygen fugacity also  
61 influences (i) melting and metasomatism of mantle rocks, thereby influencing fluxes of various  
62 magma types, and (ii) recycling of volatiles, thereby affecting global volatile cycles (Yaxley et al.,  
63 2017). Therefore, understanding  $fO_2$  in Earth's mantle is crucial for comprehending terrestrial  
64 magmatism and volatile cycles (Foley, 2011; Tappe et al., 2018). The  $fO_2$  compositions of the  
65 subcontinental lithospheric mantle (SCLM) have been shown to vary with depth and time  
66 (Woodland and Koch, 2003; Creighton et al., 2009, 2010; Yaxley et al., 2017; Tappe et al., 2021;  
67 Aulbach et al., 2022), which has the potential to shift melting regimes over geological timescales  
68 (Foley, 2011). The  $fO_2$  values can be estimated for mantle-derived peridotite (Ballhaus et al., 1991;

69 Stagno et al., 2013) and eclogite (Stagno et al., 2015) xenoliths by measuring the  $\text{Fe}^{3+}/\Sigma\text{Fe}$  ratios  
70 of their constituting garnet fractions.

71 This contribution presents the first measurements of  $\text{Fe}^{3+}/\Sigma\text{Fe}$  in garnets from six eclogite  
72 xenoliths from the KL2 hypabyssal intrusion and fourteen peridotitic garnet xenocrysts from the  
73 P9 and P10 intrusions of the Wajrakarur Kimberlite Field (WKF) located on the Eastern Dharwar  
74 craton (EDC) in southern India. We aim to constrain the redox state of the regional SCLM that  
75 underpinned Peninsular India at ca. 1.1 Ga. The KL2 intrusion forms part of the Kalyandurga  
76 cluster, which consists of seven minor kimberlite intrusions (KL1 to KL7) and is located in the  
77 southern part of the WKF (Fig. 1). The P9 and P10 minor intrusions form part of the Wajrakarur-  
78 Lattavaram cluster, situated in the north. Shaikh et al. (2020) constrained the architecture and  
79 thermal state of the regional SCLM using major and trace element compositions of garnets from  
80 P9 and P10, some of which were re-analyzed here for their  $\text{Fe}^{3+}/\Sigma\text{Fe}$  compositions. According to  
81 Shaikh et al. (2020), lithospheric thinning beneath the Dharwar craton, from ~190 km depth at 1.1  
82 Ga to ~120 km depth at present, was aided by extensive melt metasomatism at the bottom of the  
83 SCLM.

84 The ca. 1.1 Ga Kalyandurga kimberlites are special in several ways. For instance, (i) the  
85 diamondiferous KL2 minor intrusion is distinguished by an overabundance of eclogite xenoliths  
86 (>95% of the mantle xenolith population are eclogite nodules; Rao et al., 2001; Neelakantam,  
87 2001; Patel et al., 2006); (ii) the KL4 minor intrusion exhibits an exceptional abundance of mantle-  
88 derived ilmenite macrocrysts (Sastry et al., 2005); (iii) the Kalyandurga kimberlites intruded the  
89 2.6–2.5 Ga Closepet granite in close proximity to the Chitradurga Boundary Fault, which presents  
90 an important structure for the understanding of the evolution of the Dharwar craton (e.g., Chadwick  
91 et al., 2000). KL2 eclogite nodules have previously been investigated for petrography, in-situ

92 mineral major and trace element contents, and oxygen isotopic compositions to constrain their  
93 origins (Ganguly and Bhattacharya, 1987; Rao et al., 2001; Patel et al., 2006, 2009; Griffin et al.,  
94 2009; Dongre et al., 2015). Four eclogite xenoliths were examined by Ganguly and Bhattacharya  
95 (1987), while two eclogite nodules were examined by Rao et al. (2001) to determine mineral major  
96 element compositions. The first detailed petrographic observations and mineral major element data  
97 for a suite of eleven KL2 eclogite xenoliths were provided by Patel et al. (2006). In order to review  
98 the P-T conditions and origins of eclogites and pyroxenites from the WKF, Patel et al. (2009)  
99 combined published xenolith data with nine newly analyzed xenoliths and argued against the  
100 involvement of subducted ancient oceanic crust in the formation of KL2 eclogites. These authors  
101 used textural and mineral compositional evidence to support a magmatic cumulate origin for the  
102 KL2 eclogites. Babu et al. (2008) presented a much larger eclogite dataset (35 xenoliths) at the 9<sup>th</sup>  
103 International Kimberlite Conference, and Griffin et al. (2009) utilized these results to argue that  
104 this eclogite xenolith suite originated from mafic melts that ponded and crystallized at lithospheric  
105 mantle depths. Mineral major and trace element compositions, as well as the lateral distribution of  
106 mantle-derived xenoliths and xenocrysts, were used to support this interpretation (Griffin et al.,  
107 2009). In opposition to this notion, Dongre et al. (2015) examined 28 KL2 eclogite xenoliths and  
108 reported the first  $\delta^{18}\text{O}$  data (+5.3 to +7.8‰), which are best explained by a subduction-recycling  
109 model. Recently, a few more KL2 eclogite nodules were studied by Chatterjee et al. (2023)  
110 supporting the subduction model. However, no attempt has been made so far to use the eclogites  
111 and other mantle-derived materials to determine the oxidation state of the SCLM beneath southern  
112 India.

113         Herein, we apply the calibration of Stagno et al. (2015), which estimates eclogite  $f\text{O}_2$  using  
114 the major element compositions of garnet and clinopyroxene, together with  $\text{Fe}^{3+}/\Sigma\text{Fe}$  ratio

115 measurements for garnet, an approach taken in several previous eclogite xenolith studies from  
116 cratons worldwide (e.g., Smart et al., 2017, 2021a; Aulbach et al., 2019, 2022; Burness et al., 2020;  
117 Mikhailenko et al., 2020). Our garnet  $\text{Fe}^{3+}/\Sigma\text{Fe}$  measurements are complemented by in-situ major  
118 and trace element data for garnet crystals from the KL2 eclogites. For peridotitic garnet xenocrysts,  
119 we used the calibration of Stagno et al. (2013) and combined garnet  $\text{Fe}^{3+}/\Sigma\text{Fe}$  data with their  
120 modeled  $\text{Fe}^{2+}/(\text{Fe}^{2+}+\text{Mg})$  compositions, assuming equilibrium with olivine and orthopyroxene in  
121 the original peridotite host rock (O'Neil and Wood, 1979; Harley, 1984; Ryan et al., 1996; Gaul  
122 et al., 2000) at estimated equilibrium P-T conditions (Canil et al., 1999). Our results provide the  
123 first  $f\text{O}_2$  estimates for eclogites and peridotitic garnets from southern India entrained by ca. 1.1 Ga  
124 old Mesoproterozoic kimberlites that represent one of the earliest global emplacement events of  
125 diamond-bearing deep-sourced magmas (Tappe et al., 2018).

126

### 127 **Analytical techniques**

128 Seven eclogite xenoliths (KL2A to KL2G), measuring 3 to 5 cm in diameter, were collected from  
129 the KL2 kimberlite body by S. Ravi. They were cut and polished into a total of 18 standard  
130 petrographic thin sections for this study. The eclogite xenoliths are commonly rounded to  
131 subrounded (oval) nodules with medium-grained textures. Honey brown pyrope garnet crystals are  
132 embedded in a light green to white matrix formed mainly by altered omphacitic clinopyroxene.

133 A CAMECA SX100 electron microprobe housed in the Spectrum lab at the University of  
134 Johannesburg was used for quantitative in-situ mineral analyses of major and minor elements. The  
135 analyses were conducted with a nominal beam size of 1  $\mu\text{m}$ , an accelerating voltage of 20 kV, and  
136 a beam current of 20 nA. Trace elements were measured for garnet, clinopyroxene and kyanite in  
137 representative eclogite thin sections at the University of Johannesburg using a Thermo Scientific

138 iCAP RQ inductively coupled plasma mass spectrometer (ICP-MS) coupled to a 193 nm ArF  
139 RESOLUTION SE155 excimer laser. NIST SRM 612 was used as the calibration reference material,  
140 and  $^{29}\text{Si}$  was used for internal standardization. To verify accuracy of the data, various USGS  
141 basaltic glasses (BCR-2G, BHVO-2, BIR-1G) and the in-house GHR1 megacrystic garnet from  
142 the Monastery kimberlite were analyzed as secondary standards, similar to the setup reported in  
143 Tappe et al. (2023). Data quality is documented in Supp. Table 1. When compared to  
144 recommended values for the USGS glasses and the GHR1 garnet (e.g., Jochum et al., 2016; Tappe  
145 et al., 2021), the majority of trace elements analyzed reproduced with a variance of less than 10 to  
146 15%. To avoid any potential contamination from the host kimberlite during laser ablation, we  
147 rejected ICP-MS trace element measurements with  $>1$  ppm Ba (see Shaikh et al., 2020). The  
148 analytical techniques and data are described in more detail in the Appendix 1 and Supp. Table 1,  
149 respectively. The analytical techniques applied to measure the major and trace element  
150 concentrations for fourteen peridotitic garnet xenocrysts from Wajrakarur kimberlites P9 and P10  
151 are given in Shaikh et al. (2020).

152         The atomic  $\text{Fe}^{3+}/\Sigma\text{Fe}$  proportions in garnet crystals from six eclogite nodules and fourteen  
153 xenocrysts of peridotitic affinity were determined with the flank method as developed by Höfer et  
154 al. (1994) and further refined by Höfer and Brey (2007). Measurements were conducted with a  
155 JEOL JXA-8530F Plus electron microprobe at Goethe University Frankfurt, Germany. The flank  
156 method and the quantitative elemental analyses were conducted simultaneously using WDS at 15  
157 kV and 120 nA, with a beam diameter of 1  $\mu\text{m}$ . Two spectrometers with TAPL crystals for high  
158 intensities and the smallest detector slit (300  $\mu\text{m}$ ) were used, with 100 s counting time for  $\text{Fe}L_{\alpha}$   
159 and  $\text{Fe}L_{\beta}$ . The  $\text{Fe}^{3+}/\Sigma\text{Fe}$  ratios for garnets were determined by applying the correction for self-  
160 absorption using natural and synthetic garnet crystals with variable total Fe and  $\text{Fe}^{3+}/\Sigma\text{Fe}$ , as

161 independently determined by Mössbauer spectroscopy (Höfer and Brey, 2007). We used  
162 Damknolle garnet megacrysts from Nigeria (Rankenburg et al., 2004) and the McGuire almandine  
163 from the U.S.A. (McGuire et al., 1992) along with three in-house Cr-pyrope standards (UA5,  
164 UA10, UA17) as reference materials. The Cr-pyrope crystals have a wide range of total Fe, which  
165 is ideal for calibration (Supp. Table 1) to obtain fit parameters derived exclusively from these three  
166 natural garnets. The other three spectrometers, not involved in flank method measurements, carried  
167 out elemental analysis of Si, Ti, Al, Cr, Fe, Mn, Ni, Mg, Ca, Na, K and P during the same  
168 measurement cycle. Appropriate silicate minerals [pyrope (Mg, Al, Si), albite (Na), CaSiO<sub>3</sub> (Ca)]  
169 and a phosphate mineral [KTiOPO<sub>4</sub>(Ti,K,P)], as well as metals or metal oxides [iron metal (Fe),  
170 NiO (Ni), MnTiO<sub>3</sub> (Mn), Cr<sub>2</sub>O<sub>3</sub> (Cr)] were used as calibration standards. A PRZ routine was used  
171 for matrix correction. The analytical uncertainty in Fe<sup>3+</sup>/ΣFe ratio measurements by the EPMA  
172 flank method is approximately ± 0.01 (1σ), and it is noted that in general the uncertainty is  
173 inversely correlated with garnet FeO content. A recent discussion about the applicability of the  
174 flank method for determining ferric-ferrous iron ratios can be found in Rzehak et al. (2020).

175

## 176 **Results**

### 177 **Petrography**

#### 178 *KL2 Eclogites*

179 Secondary alteration is prominent in the KL2 eclogite nodules, with a general decrease in the level  
180 of alteration from omphacite to kyanite to garnet (Fig. 2, 3), which was also observed previously  
181 (Sastry et al., 2005; Patel et al., 2006; Dongre et al., 2015). Garnet crystals are least altered but  
182 show minor secondary carbonate and hydro-garnet replacement along grain boundaries and  
183 fractures. Despite the alteration of several of our KL2 eclogite samples, the secondary minerals

184 preserve the original rock textures, such as elongation texture with substantial micro-fracturing in  
185 garnet and clinopyroxene relics (e.g., Fig. 2, 3). Among the examined eclogite nodules, substantial  
186 clinopyroxene and kyanite alteration was observed in five samples (KL2C, KL2D, KL2E, KL2F,  
187 KL2G), whereas these phases were completely altered in sample KL2B. The freshest sample  
188 KL2A does not contain kyanite.

189 Subhedral to spherical garnet grains are interlocked with anhedral clinopyroxene and  
190 bladed kyanite in relatively fresh samples with minor alteration along grain boundaries. Inclusions  
191 of garnet and clinopyroxene are frequent in kyanite (Fig. 3 d, e, f). A few eclogite nodules (KL2D,  
192 KL2F) contain needles of corundum, which are generally spatially associated with kyanite (Fig.  
193 4a). Rutile is preserved as an inclusion in kyanite within the KL2A eclogite nodule (e.g., Fig. 4b).  
194 In the majority of samples analyzed, the relative modal proportions of garnet, omphacite and  
195 kyanite are ~45:45:10, and ~50:50 in bimineralic kyanite-free eclogite nodules with only very  
196 minor kyanite and corundum in a few samples. Carbonate and chlorite are the most prevalent  
197 alteration products of all primary minerals. Omphacite is typically replaced by hornblende and  
198 diopside, kyanite by celsian feldspar (along grain boundaries and fractures), and garnet by chlorite,  
199 epidote, celsian and grossular. The matrix of the eclogites contains rare sulfides (NiFeS) and pure  
200 nickel oxide (NiO). Mukherjee et al. (2021) reported native gold particles and Au-Pt alloys from  
201 KL2 eclogite xenoliths. A very detailed petrographic report for KL2 eclogites is given by Patel et  
202 al. (2006).

203

#### 204 *Peridotitic garnet xenocrysts*

205 Fourteen peridotitic garnet xenocrysts (3-7 mm in size) from the P9 and P10 minor intrusions were  
206 mounted on thin sections and polished for in-situ mineral chemical examination of major and trace

207 elements. Garnet grains exhibit micro-fracturing and host rare inclusions of Cr-diopside consistent  
208 with their peridotitic mantle origins.

209

## 210 **Major and trace element compositions of minerals**

### 211 *KL2 eclogites*

212 The five primary minerals in KL2 eclogites (garnet, clinopyroxene, kyanite, corundum, rutile)  
213 were analyzed for major and trace elements. Secondary phases such as celsian, andradite,  
214 grossular, serpentine and carbonates were also analyzed for major elements. Supp. Table 1 lists  
215 representative major, minor and trace element compositions of primary phases essential for this  
216 work, as well as the compositions of secondary phases for documentation purposes. We only  
217 address the compositions of primary phases here, and readers are referred to Patel et al. (2006) for  
218 a detailed description of secondary phases in the KL2 eclogite xenoliths.

219         Despite the secondary alteration along grain boundaries and fractures, garnets in KL2  
220 eclogites show relatively uniform compositions (Supp. Table 1). The eclogitic garnet compositions  
221 determined here vary between  $\text{Alm}_{24-27}\text{GrS}_{25-58}\text{Pyp}_{18-48}$  falling within the range of published data  
222 for KL2 (e.g., Patel et al., 2006; Dongre et al., 2015). Garnets have low  $\text{Na}_2\text{O}$  and  $\text{TiO}_2$  contents  
223 ( $<0.3$  wt.%; Supp. Table 1), which is typical for low-pressure eclogites (Gurney and Moore, 1993).  
224 Chondrite-normalized (after Sun and McDonough, 1989) REE patterns of garnets from KL2  
225 eclogites show LREE-depletion, a positive Eu anomaly, and flat MREE-HREE distributions (Fig.  
226 5c), which is characteristic for garnets from cratonic eclogites worldwide (e.g., Jacob, 2004;  
227 Aulbach and Jacob, 2016; Aulbach and Smart, 2023). Garnets show variable trace element  
228 concentrations: Sc (29–35 ppm), Ti (828–1135 ppm), V (48–71 ppm), Cr (109–518 ppm), Ni (15–

229 84 ppm), Zr (2–6 ppm), and Y (5–8 ppm). They have low Sr contents (4–10 ppm) and U-Th  
230 concentrations at sub-ppm levels.

231 Clinopyroxenes are omphacitic in nature ( $\text{Ae}_{7-10}\text{Jd}_{31-43}\text{Di}_{50-61}$ ) similar to the known  
232 compositions of KL2 eclogitic clinopyroxene ( $\text{Ae}_{3-17}\text{Jd}_{13-52}\text{Di}_{41-79}$ ). Contents of  $\text{Na}_2\text{O}$  and  $\text{Al}_2\text{O}_3$   
233 range from 2.9–8.2 wt.% and 5.8–16.2 wt.%, respectively.  $\text{Cr}_2\text{O}_3$  content is low at 0.1 wt.%, rarely  
234 approaching 1.6 wt.%. Clinopyroxene shows a clear negative correlation between  $\text{MgO}$  and  $\text{Na}_2\text{O}$   
235 (inset in Fig. 5b), typical for kimberlite-borne eclogites. Their chondrite-normalized REE patterns  
236 exhibit high LREE/HREE with a notable positive Eu anomaly (Fig. 5d).

237 Kyanite in KL2 eclogite xenoliths contains trace amounts of  $\text{FeO}$  (<0.5 wt.%) and  $\text{Cr}_2\text{O}_3$   
238 (<0.9 wt.%) (Supp. Table 1). Most trace elements have concentrations below the EPMA detection  
239 limit (<30 ppm), except for Ti (106–294 ppm), V (35–70 ppm), Cr (157–604 ppm) and Ga (7–10  
240 ppm). Corundum is a pure aluminous phase with a mean  $\text{Al}_2\text{O}_3$  content of ~99 wt.% and minor  
241 amounts of  $\text{FeO}$  (<0.5 wt.%) and  $\text{Cr}_2\text{O}_3$  (<0.16 wt.%). Rutile is a pure Ti-oxide phase (~99 wt.%  
242  $\text{TiO}_2$ ) with minor amounts of  $\text{FeO}$  (<0.12 wt.%) and  $\text{Cr}_2\text{O}_3$  (<0.18 wt.%).

243

#### 244 *Peridotitic garnet xenocrysts*

245 Major and trace element compositions of peridotitic garnet xenocrysts were discussed in detail by  
246 Shaikh et al. (2020). For this redox study, we included 11 lherzolitic G9 grains, two harzburgitic  
247 G10 grains, and a single Ti-metasomatic G11 grain (garnet classification of Grütter et al., 2004;  
248 Fig. 6a). Overall, these garnet crystals show a wide range of  $\text{Cr}_2\text{O}_3$  (1.8–11.8 wt.%), moderate  $\text{CaO}$   
249 (4.3–5.9 wt.%) and very low  $\text{TiO}_2$  contents (<0.35 wt.%). Most of these garnets show ‘normal’  
250 chondrite-normalized REE patterns, however, xenocrysts with >5 wt.%  $\text{Cr}_2\text{O}_3$  are characterized

251 by 'sinusoidal' REE patterns (Fig. 6b). Clinopyroxene inclusions in the garnet xenocrysts are Cr-  
252 diopsides (1.1–2.1 wt.% Cr<sub>2</sub>O<sub>3</sub>; En<sub>50–55</sub>Wo<sub>41–46</sub>Fs<sub>4</sub>) with consistently high Mg# values (0.92–0.94).  
253

#### 254 **Bulk eclogite reconstruction and fO<sub>2</sub> estimates based on redox-sensitive elements**

255 Due to pervasive alteration and kimberlite melt infiltration of the KL2 eclogite nodules (see Fig.  
256 3), bulk-rock compositions were reconstructed from the measured chemical compositions of the  
257 primary minerals (clinopyroxene, garnet, corundum, rutile, ± kyanite) in combination with their  
258 estimated modal mineral abundances. This method of bulk-rock reconstruction has been widely  
259 used in the past and continues to be a valuable tool in the study of xenolithic eclogites (e.g., Jacob,  
260 2004; Tappe et al., 2011; Smart et al., 2016; Aulbach and Smart, 2023). EPMA data were used for  
261 the major elements and LA-ICP-MS data for the trace elements. The calculations were performed  
262 taking into account the specific gravities (Deer et al., 2013) of the primary minerals (3.3 g/cm<sup>3</sup> for  
263 clinopyroxene, 3.6 g/cm<sup>3</sup> for garnet, 3.3 g/cm<sup>3</sup> for kyanite, 4.04 g/cm<sup>3</sup> for rutile, 4.02 g/cm<sup>3</sup> for  
264 corundum) and for bulk eclogite (3.45 g/cm<sup>3</sup>). The specific gravity was utilized to calculate the  
265 relative weight proportions. Given that the variability of the average chemical compositions of the  
266 samples studied is low (generally <10% RSD), the major source of uncertainty in the bulk-rock  
267 reconstructions stems from the estimates of the modal mineral abundances. For bimineralic  
268 kyanite-free samples, we assumed 49 vol.% for clinopyroxene and garnet each, and 1 vol.% for  
269 rutile and corundum each. For kyanite-bearing eclogite nodules, we assumed 44 vol.% for  
270 clinopyroxene and garnet each, 1 vol.% for rutile and corundum each, and 10 vol.% for kyanite.  
271 Bulk eclogite reconstruction results for the major elements (normalized to 100 wt.%) and the trace  
272 elements (in ppm) are given in Supp. Table 1. The results are plotted in Fig. 7a-c to classify the  
273 eclogites (see Discussion), which show low MgO, high Na<sub>2</sub>O, and Eu/Eu\* anomalies.

274 As shown in Figure 8a, the estimated modal abundance of rutile has a significant effect on  
275 the overall budget of Ti, which in combination with the concentration of V, provides an estimate  
276 for  $fO_2$  (e.g., Aulbach and Stachel, 2022). Based on previous analyses of mantle eclogites and our  
277 own petrographic observations, we conclude that a modal rutile abundance between 0.5 and 1  
278 vol.% is realistic. Regardless of the exact choice of rutile abundance, our KL2 eclogite samples  
279 fall just below FMQ-2 in Figure 8a. In terms of Lu/Gd versus Ce/Yb ratios, our reconstructed bulk  
280 eclogite compositions agree with mantle eclogites from cratons worldwide, partly overlapping  
281 with metasomatized eclogites (Fig. 8b). In terms of V/Sc versus MgO systematics, our  
282 reconstructed bulk eclogite compositions suggest a  $fO_2$  value of around FMQ-2 (Fig. 8c), similar  
283 to the Ti-V based estimate (Fig. 8a).

284

#### 285 **Thermobarometer choice**

286 Nimis (2022) presented an overview of geothermobarometers applicable to eclogites. Older  
287 thermometer calibrations based on garnet-clinopyroxene Fe-Mg exchange developed by Ellis and  
288 Green (1979) and Powell (1985) have been demonstrated to be unreliable because the effect of Ca  
289 was not considered (e.g., Brey and Köhler, 1990; Nimis and Grütter, 2010). Pressure estimates by  
290 Beyer et al. (2015) for eclogite xenoliths show systematically lower values (by ~10 kbar) when  
291 compared to pressures calculated using orthopyroxene-garnet assemblages at the same  
292 temperatures (Nimis, 2022). Furthermore, due to the high sensitivity of the equation to slight  
293 inaccuracies in clinopyroxene major element compositions, the Beyer et al. (2015) eclogite  
294 barometer is prone to produce significant errors.

295 In this study, temperatures were determined for six KL2 eclogite xenoliths (at an assumed  
296 pressure of 40 kbar) based on Fe-Mg exchange between garnet and clinopyroxene (Krogh, 1988;

297  $T_K$ ). Temperatures for KL2B eclogite could not be calculated due to the complete alteration of  
298 clinopyroxene. In addition, published data for 34 KL2 eclogite nodules were reprocessed with the  
299 same thermometer equation. The eclogite equilibrium pressures ( $P_{HC40}$ ) were calculated by  
300 subsequently projecting the obtained temperatures onto the regional cratonic geotherm of 40  
301  $mW/m^2$  (after Shaikh et al., 2020). Temperatures ( $T_K$ ) obtained for an assumed pressure of 40 kbar  
302 range from 945 to 1180 °C. Pressures obtained after geotherm projection range from 38 to 50 kbar  
303 (Fig. 9a), equivalent to 120-160 km depths. Alternative temperature estimates calculated after Ellis  
304 and Green ( $T_{EG}$ ; 1979), Powell ( $T_{Po}$ ; 1985), Ai ( $T_{Ai}$ ; 1994), Ganguly et al. ( $T_{Gn}$ ; 1996), Krogh  
305 Ravna ( $T_{KR}$ ; 2000), and Nakamura ( $T_{NK}$ ; 2009) yielded very similar results for the KL2 eclogite  
306 xenoliths (Supp. Table 1). Overall, our P-T results compare well to those obtained by Patel et al.  
307 (2009) and Dongre et al. (2015) (i.e., 36–54 kbar).

308 The equilibration pressures ( $P_{HC40}$ ) for peridotitic garnet xenocrysts were calculated using  
309 Ni-in-garnet temperatures (970–1217 °C) (Canil, 1999) projected onto the regional 40  $mW/m^2$   
310 geotherm (Fig. 9b). Pressure readings for two garnet xenocrysts (P9G51A, P9G52C) were  
311 corrected using a single-pyroxene thermobarometer applied to Cr-diopside inclusions (after Nimis  
312 and Taylor, 2000). The peridotitic garnet xenocrysts studied equilibrated at 40 to 53 kbar  
313 corresponding to ~125-170 km depth, similar to the depths of origin of the KL2 eclogite xenoliths.

314

#### 315 **Measured ferric iron contents in garnet, and calculated $fO_2$**

316 Table 1 and Table 2 list the  $Fe^{3+}/\Sigma Fe$  ratios for garnets from KL2 eclogite xenoliths and peridotitic  
317 garnet xenocrysts, respectively.  $Fe^{3+}/\Sigma Fe$  ratios for our eclogitic garnets vary from 0.02 to 0.05  
318 ( $\pm 0.01$ ), which is within the global range of mantle-derived eclogitic garnets (0.02–0.09; Stagno  
319 et al., 2015; Smart et al., 2017, 2021a, 2021b; Aulbach et al., 2019, 2022). The  $Fe^{3+}/\Sigma Fe$  ratios for

320 our peridotitic garnet xenocrysts range from 0.02 to 0.10 ( $\pm 0.01$ ), extending to higher values than  
321 those measured for KL2 eclogites.

322 We calculated  $\Delta \log f_{\text{O}_2}$  values (relative to the FMQ buffer) for the KL2 eclogite xenoliths  
323 using the oxybarometer of Stagno et al. (2015), which was calibrated using coesite/quartz-bearing  
324 eclogites. By applying the calculated pressure–temperature values and measured chemical  
325 compositions for garnet and clinopyroxene, the KL2 eclogites yielded  $\Delta \log f_{\text{O}_2}$  values between  
326 FMQ-2.5 and FMQ-0.9, with uncertainties of  $\pm 0.6$  log units for corundum-free eclogites (Fig. 10).  
327 These redox compositions fall closer to the carbonate stability field compared with the  $f_{\text{O}_2}$   
328 systematics of other xenolithic eclogite suites from cratons worldwide (Stagno et al., 2015;  
329 Burness et al., 2020; Smart et al., 2021a, b; Aulbach et al., 2022). The above  $f_{\text{O}_2}$  range for the KL2  
330 eclogite xenoliths is in good agreement with our less-precise reconstructed bulk eclogite  $f_{\text{O}_2}$   
331 estimate of  $< \text{FMQ}-2$  (see Fig. 8). As per Smart et al. (2021), a correction is required for the  $f_{\text{O}_2}$   
332 calculations for corundum-bearing silica-undersaturated eclogites. The correction involves the  
333 incorporation of silica activity using corundum +  $\text{SiO}_2$  (coesite) = kyanite equilibrium. Application  
334 of this correction to the KL2D and KL2F corundum-bearing silica-undersaturated eclogite  
335 xenoliths shifts their  $\Delta \log f_{\text{O}_2}$  values by 1.5 log units toward more reduced redox compositions  
336 (FMQ-3.9 and FMQ-3.6), more similar to eclogite xenoliths from the Kaapvaal craton root (Fig.  
337 10). There is a weak correlation between  $\Delta \log f_{\text{O}_2}$  values and contents of MgO and CaO for garnet,  
338 with  $\Delta \log f_{\text{O}_2}$  increasing with decreasing MgO at increasing CaO (Fig. 11). No correlation is  
339 observed between the trace element concentrations of eclogitic garnets and their  $\Delta \log f_{\text{O}_2}$  values.

340 For the peridotitic garnet xenocrysts, we used the Stagno et al. (2013) equation, which  
341 requires input for pressure and temperature (see above), as well as the Fe# values for coexisting  
342 olivine and orthopyroxene. The Fe# values for orthopyroxene in equilibrium with garnet were

343 calculated using Equation 7 in Ryan et al. (1996) and Equation 11 in Harley (1984). The Fe# values  
344 for olivine in equilibrium with garnet were calculated by inverting the garnet-olivine thermometer  
345 of O'Neill and Wood (1979), as demonstrated by Gaul et al. (2000). The obtained Fe# values range  
346 from 0.06 to 0.08 for olivine and 0.03 to 0.04 for orthopyroxene (variance is <1%; Gaul et al.,  
347 2000; Ryan et al., 1996), corresponding to Mg# values of 0.92-0.94 and 0.96-0.97, respectively.  
348 These inferred values are similar to the Mg# values reported for olivine and orthopyroxene from  
349 rare peridotite xenoliths from the Dharwar craton root (0.90-0.94 for olivine; 0.90-0.95 for  
350 orthopyroxene; Ganguly and Bhattacharya, 1987; Nehru and Reddy, 1989; Pattnaik et al., 2020),  
351 and also overlap with the compositions of mantle-derived olivine xenocrysts from Wajrakarur  
352 kimberlites (0.90-0.94 Mg#; Shaikh et al., 2019, 2018). This complex procedure enabled us to  
353 calculate  $\Delta\log fO_2$  values between FMQ-4.5 and FMQ-2.6 ( $\pm 0.9$ ) for the peridotitic garnet  
354 xenocrysts (Fig. 10).

355

## 356 **Discussion**

### 357 **Nomenclature and origin of the KL2 eclogites**

358 Mantle-derived eclogite xenoliths are generally thought to be formed by either (i) subduction of  
359 gabbroic or basaltic oceanic crust (e.g., Taylor and Neal, 1989; Barth et al., 2001; Jacob, 2004),  
360 (ii) emplacement of basaltic melt at depths within cratonic mantle lithosphere with high-pressure  
361 cumulate formation (e.g., Viljoen et al., 1996; Barth et al., 2002), or (iii) extraction of tonalitic  
362 melt from basaltic oceanic crust during subduction leaving behind an eclogitic residue (e.g., Jacob  
363 and Foley, 1999; Barth et al., 2002; Tappe et al., 2011a). Each of these genetic types of cratonic  
364 eclogites is supported by textural, mineralogical, geochemical, and isotopic evidence (Aulbach and  
365 Smart, 2023). Accordingly, mantle-derived eclogites have been classified into several types based

366 on major and trace element compositions of garnet and clinopyroxene (McCandless and Gurney,  
367 1989; Taylor and Neal, 1989; Jacob et al., 2009) and reconstructed bulk compositions (e.g.,  
368 Aulbach and Jacob, 2016; Smart et al., 2017).

369 The KL2 eclogites studied here contain clinopyroxene that is enriched in Na<sub>2</sub>O (typically  
370 4-7 wt.%) and has moderate MgO contents (typically 6-11 wt.%). These clinopyroxene  
371 compositions are characteristic for Type B and Type C eclogites of Taylor and Neal (1989; Fig.  
372 5a, b), interpreted to originate from subducted ancient oceanic crust protoliths. The relatively low  
373 K<sub>2</sub>O contents of clinopyroxene (<0.1 wt.%, or below detection limit), together with the low Na<sub>2</sub>O  
374 (0.15 wt.%) and TiO<sub>2</sub> (0.5 wt.%) contents in garnets (Supp. Table 1), are similar to the mineral  
375 compositions of Group II non-metasomatized eclogite xenoliths described by McCandless and  
376 Gurney (1989). KL2 eclogites contain garnets with moderate Mg# values (typically between 0.4-  
377 0.7) and high Ca# values (0.2-0.6) (Fig. 5; 7), similar to the high-Ca eclogites as defined by  
378 Aulbach and Jacob (2016). KL2 eclogitic garnets and clinopyroxenes exhibit Eu anomalies in their  
379 REE patterns, which are also mirrored in the reconstructed bulk eclogite compositions (Fig. 5c, d;  
380 7c). The reconstructed bulk eclogite compositions are relatively high in Na<sub>2</sub>O (2-3.5 wt.%; Fig.  
381 7a). These geochemical features indicate that the protolith of the KL2 eclogite xenoliths was a  
382 plagioclase-rich gabbroic lithology as part of ancient oceanic crust. This finding is consistent with  
383 the model by Dongre et al. (2015), who presented evidence for low-temperature alteration of the  
384 eclogite protolith near the Earth's surface based on significantly elevated δ<sup>18</sup>O values for garnet  
385 (up to +7.8‰) from some KL2 eclogite xenoliths. However, features such as interlocking garnet-  
386 clinopyroxene textures, rutile blebs in clinopyroxene and garnet, the presence of corundum and  
387 Na<sub>2</sub>O-poor garnet and K<sub>2</sub>O-poor clinopyroxene, and Eu-anomalies are more similar to Type II<sub>L</sub>  
388 eclogite xenoliths from the Roberts Victor orangeite in South Africa (Hardman et al., 2021). These

389 eclogite nodules are considered to represent cumulates of magmas sourced from a depleted mantle  
390 reservoir that had undergone prior extraction of MORB-like melts (Hardman et al., 2021), but  
391 subducted oceanic crustal origins have also been put forward for the classic Roberts Victor eclogite  
392 xenolith suite (e.g., Jacob et al., 2005). For KL2 eclogites, Patel et al. (2009) proposed a high-  
393 pressure cumulate origin, which is supported by textural features such as graded layering and  
394 garnet necklaces as well as garnet-kyanite clusters, plus evidence from mineral compositions such  
395 as similar clinopyroxene geochemistry in the eclogite xenoliths and cumulate pyroxenites. In  
396 contrast, Griffin et al. (2009) suggested KL2 eclogite formation by solidification of mafic melts  
397 near the base of the SCLM. Clearly, there are ‘eclogites and eclogites’, and considering the scope  
398 of our study (mantle redox), we refrain from further speculations as to the nature and origin of the  
399 KL2 eclogite protolith.

400

#### 401 **Redox state of KL2 eclogite xenoliths**

402 Using compositions of eclogitic garnets from the southern region of the WKF (Kalyandurga  
403 kimberlite cluster), we calculated  $\Delta\log f_{O_2}$  values between FMQ-2.5 and FMQ-0.9 ( $\pm 0.6$ ), with  
404 two eclogite nodules (KL2C and KL2E) recording more reduced oxidation states (FMQ-3.9 and  
405 FMQ-3.6). On the basis of these  $\Delta\log f_{O_2}$  values and their depth distribution, the KL2 eclogites  
406 straddle the boundary between diamond and carbonate stability fields in terms of carbon speciation  
407 (Fig. 10). The peridotitic garnet xenocrysts from the P9 and P10 kimberlite bodies of the northern  
408 region of the WKF (Wajrakarur-Lattavaram kimberlite cluster) yielded  $\Delta\log f_{O_2}$  values ranging  
409 from FMQ-4.5 to FMQ-2.6 ( $\pm 0.9$ ), at the low end of eclogitic  $\Delta\log f_{O_2}$  values determined here. This  
410 observation suggests that the majority of KL2 mantle eclogites have experienced more oxidizing  
411 conditions compared to cratonic peridotites at similar depths prior to entrainment into erupting

412 kimberlite magmas at ca. 1.1 Ga. The KL2 eclogite xenoliths studied have  $\Delta\log fO_2$  values that  
413 overlap with those of many kimberlite-borne eclogite nodules from cratons worldwide (FMQ-1 to  
414 FMQ-5; Stagno et al., 2015; Burness et al., 2020; Smart et al., 2021a, b; Aulbach et al., 2022).

415 Depth related redox heterogeneity has been observed for eclogites from different intervals  
416 within cratonic SCLM worldwide (e.g., Burness et al., 2020). For example, Kaapvaal cratonic  
417 eclogites from mid-lithospheric depths show more reducing redox conditions ( $\Delta\log fO_2 = \text{FMQ-}$   
418  $5.3$  to  $\text{FMQ-3.3}$ ) compared to eclogites from the lowermost lithosphere ( $\text{FMQ-3.9}$  to  $\text{FMQ-1.5}$ )  
419 (Burness et al., 2020). However, this apparent relationship was not observed in the data produced  
420 for other localities on the Kaapvaal craton or elsewhere (Smart et al., 2017, 2021a, b; Aulbach et  
421 al., 2022). Based on our data for KL2 eclogites, we observe notable variations in their oxidation  
422 state over a relatively narrow depth interval, but large-scale redox variations with depths cannot  
423 be discerned. Further work is required to explore such a potential relationship. We can conclude,  
424 however, that the KL2 eclogites present a suitable diamond host rock given their P-T- $fO_2$   
425 systematics (Fig. 10). This conclusion is supported by the diamondiferous nature of the KL2  
426 kimberlite body and mineral inclusion data from the WKF (Ravi et al., 2013).

427

#### 428 **Redox state of mantle peridotites and metasomatism of the Dharwar craton root**

429 Garnet xenocrysts of peridotitic affinity from the P9 and P10 kimberlites revealed a wide range of  
430  $\Delta\log fO_2$  values between FMQ-4.5 and FMQ-2.6 ( $\pm 0.9$  log units). Griffin et al. (2009) and Shaikh  
431 et al. (2020) presented extensive trace element data for garnet and clinopyroxene xenocrysts from  
432 Wajrakarur kimberlites, which allows us to explore any possible relationship between melt  
433 metasomatism of the SCLM and its redox composition. Shaikh et al. (2020) proposed the presence  
434 of a mid-lithospheric discontinuity between ~145 and 160 km depth.

435 The Dharwar craton root is strongly metasomatized at the very bottom, a trend known from  
436 many lithospheric mantle profiles beneath cratons worldwide (e.g., Griffin et al., 1999b; Kopylova  
437 et al., 1999; Kargin et al., 2016; Smart et al., 2017; Aulbach et al., 2007, 2013, 2017; Tappe et al.,  
438 2021). However, unlike the Kaapvaal craton, the Dharwar SCLM shows concomitant enrichment  
439 in Zr and Y in garnet (Shaikh et al., 2020). This feature has been interpreted to result from high-  
440 temperature mantle metasomatism by mixed silicate-carbonate melts (Shaikh et al., 2020) or by  
441 basaltic melts (Griffin et al., 2009). Although, the Ti/Eu versus Zr/Hf systematics of peridotitic  
442 garnets, suggest a kimberlitic to carbonatitic nature of the metasomatic agents (Shaikh et al., 2020).

443 According to global datasets, the oxidation state of mantle peridotite varies laterally and  
444 vertically across the SCLM (e.g., Woodland and Koch, 2003; Creighton et al., 2009; Yaxley et al.,  
445 2017; Stagno et al., 2013; Tappe et al., 2021). For example, in the garnet stability field, the  
446 Kaapvaal SCLM shows a progressively more reducing trend with increasing depth ( $\Delta\log fO_2$  FMQ-  
447 2 at 110 km to FMQ-4 at 210 km; Luth, 1990; Woodland and Koch, 2003; Creighton et al., 2009,  
448 2010; Tappe et al., 2021). This crystal chemistry-controlled depth- $fO_2$  trend has been masked by  
449 oxidative metasomatism beneath the Kimberley area on the Kaapvaal craton, where many  
450 peridotite xenoliths are offset to higher-than-expected  $fO_2$  values (Creighton et al., 2009; Hanger  
451 et al., 2015). This is also consistent with observed  $Fe^{3+}$  variations in metasomatic growth zones on  
452 mantle-derived garnet crystals (McCammon et al., 2001). The peridotitic garnet xenocrysts from  
453 the WKF studied here show variations in  $\Delta\log fO_2$  and they fall within the Kaapvaal peridotite P-  
454  $fO_2$  array, with a few samples showing slightly higher  $\Delta\log fO_2$  values approaching the carbonate  
455 stability field (Fig. 10). The  $Fe^{3+}/\Sigma Fe$  ratios measured for trace element enriched garnet xenocrysts  
456 with normal REE patterns show a remarkable positive correlation with incompatible trace element  
457 concentrations (Ti, Zr, Y, V; Fig. 12), possibly indicating a metasomatic control on cratonic mantle

Formatted: Not Highlight

458 redox (Creighton et al., 2009). These garnet xenocrysts were sampled from ~125–160 km depths,  
459 an SCLM interval that was identified as a modally metasomatized mid-lithospheric discontinuity  
460 by Shaikh et al. (2020). Overall, the link between carbonated silicate melt metasomatism and  
461 mantle redox in the Dharwar craton root may be responsible for local diamond destruction, as  
462 reported for other cratons worldwide (Creighton et al., 2009; Fedortchouk et al., 2019).

463

#### 464 **Linking mantle redox and the diversity of 1.1 Ga kimberlitic magmatism in-southern India**

465 The WKF comprises a diverse range of diamondiferous magma types, including archetypal  
466 kimberlites, lamproites, orangeites, and ultramafic lamprophyres (see compilation in Shaikh et al.,  
467 2017; Pandey and Chalapathi Rao, 2020). To date, 48 minor intrusions of exclusively  
468 Mesoproterozoic age (ca. 1.1 Ga) are known to occur within a relatively small area that is 80 × 70  
469 km in size. The coeval emplacement of diverse volatile-rich ultramafic magma types reflects  
470 prominent mineralogical heterogeneity in the Dharwar craton root (e.g., Sarkar et al., 2021), as  
471 was also demonstrated for cratonic regions and their primitive potassic magmatism on either side  
472 of the North Atlantic (Tappe et al., 2008, 2011b; Dalton et al., 2019).

473 The correlation between metasomatic overprint and redox state of the Dharwar craton root,  
474 as demonstrated in this study, appears to have important implications for the petrogeneses of  
475 kimberlites, lamproites and closely related primitive potassic rocks. Progressive oxidative  
476 metasomatism along conduits in the SCLM was caused by infiltrating carbonated silicate melts  
477 that probably originated from low-degree partial melting of the underlying convecting mantle  
478 including its recycled crustal components (e.g., Nowell et al., 2004; Malkovets et al., 2007). The  
479 resultant  $fO_2$  heterogeneities in the SCLM allowed for stabilization of distinctly different  
480 metasomatic assemblages that may be dominated by either amphiboles, micas, or carbonates

481 (Foley et al., 1986; Foley, 2011; Tappe et al., 2008; Yaxley et al., 2017). The highly variable nature  
482 of SCLM metasomes, and also local lack of metasomes, may explain the close spatiotemporal  
483 association of diverse types of primitive K-rich magmas (lamproites, orangeites, ultramafic  
484 lamprophyres) and kimberlites in the WKF.

485 Shaikh et al. (2017) suggested a model for the origin of various types of diamond-bearing  
486 magmas in the WKF, following concepts developed in Tappe et al. (2008, 2011b), where  
487 carbonated silicate melts from the asthenosphere interacted with variably metasomatized  
488 lithologies of the SCLM to produce the diversity of ca. 1.1 Ga old volatile-rich ultramafic rocks  
489 known from southern India. According to this model, metasomatic phlogopite–carbonate  
490 dominated veins were reactivated by infiltrating asthenosphere-derived melts (proto-kimberlitic  
491 melts), which gave rise to ultramafic lamprophyre, orangeite and lamproite magmas as a function  
492 of increasingly higher proportions of micas in the cratonic mantle source (Shaikh et al., 2017).  
493 Sarkar et al. (2021) compared the compositions of magmatic and xenocrystic olivine populations  
494 from Wajrakarur kimberlites and lamproites. These authors suggested that both magma types have  
495 a common asthenospheric mantle source, with lamproites revealing a larger extent of assimilation  
496 of Fe-rich lithospheric metasomes.

497

#### 498 **On the ‘overabundance’ of eclogite xenoliths in the KL2 kimberlite**

499 Despite the general xenolith deficiency, the WKF minor intrusions reveal contrasting mantle  
500 sampling patterns. For example, the KL2 kimberlite is marked by an overabundance of eclogite  
501 xenoliths, whereas kimberlites and related rocks from the Wajrakarur-Lattavaram cluster contain  
502 more peridotite xenoliths (Rao et al., 2001; Patel et al., 2006). This apparent bias is also mirrored

503 by the diamond occurrences (Ravi et al., 2013) and distributions of eclogitic versus peridotitic  
504 garnet xenocrysts (Griffin et al., 2009; Shaikh et al., 2020).

505         Although kimberlites and related rocks with an overabundance of eclogite xenoliths are  
506 very rare, they occur on most cratons worldwide such as the Kaapvaal craton (e.g., Roberts Victor,  
507 Bellsbank), the Slave craton (e.g., Jericho, Voyageur), the North Atlantic craton (e.g., Nunatak  
508 1390) and the Siberian craton (e.g., Zagadochnaya) (Schulze, 1989; Jacob, 2004; Smart et al.,  
509 2009, 2017, 2021a; Tappe et al., 2011a; Kopylova et al., 2016; Hardman et al., 2021; Aulbach and  
510 Smart, 2023). Eclogite xenolith overabundance has been linked to localized enrichment of the  
511 peridotite-dominated cratonic mantle column with eclogite components (e.g., Nixon and Davies,  
512 1987) or biased preservation of xenoliths during entrainment into kimberlitic magmas (e.g.,  
513 Schulze, 1989). Kopylova et al. (2016) inferred lateral continuity of eclogites within the Slave  
514 craton SCLM, where an eclogite-rich layer may represent the remnant of an imbricated oceanic  
515 [lithosphere](#) slab. The abundance of eclogite components has great economic significance because  
516 they contribute up to 30% of lithospheric diamonds in global statistics (Stachel and Luth, 2015),  
517 which can be even higher on a regional scale. The overall abundance of eclogitic components in  
518 peridotite-dominated SCLM has been estimated at <1 vol.% (Schulze, 1989); however, higher  
519 abundances of up to 4-10 vol.% have been suggested for the Slave craton (Griffin et al., 1999;  
520 Kopylova et al., 2016). The combined petrological-geophysical approach by Garber et al. (2018)  
521 devised an even higher eclogite abundance within the SCLM beneath cratons (up to 20 vol.%).  
522 Regardless of the [exact](#) precise amount of eclogites within the cratonic mantle lithosphere, the  
523 KL2 occurrence on the Eastern Dharwar craton adds to the kimberlite localities that have a  
524 somewhat inexplicable abundance of xenolithic eclogites, which may influence the redox

525 distribution within the local SCLM and, by inference, also its volatile element and diamond  
526 inventory.

527

## 528 **Summary and Conclusions**

529 The  $\text{Fe}^{3+}/\Sigma\text{Fe}$  compositions of garnets were determined by the EPMA flank method for six eclogite  
530 xenoliths from the KL2 kimberlite and fourteen peridotite-derived xenocrysts from the P9 and P10  
531 kimberlites on the Eastern Dharwar craton in southern India. KL2 eclogites are characterized by  
532 low  $\Delta\log f_{\text{O}_2}$  values between FMQ-3.9 and FMQ-0.9 ( $\pm 0.6$ ), which suggests that they could have  
533 acted as diamond host rocks within the deeper Dharwar craton root. The peridotite-derived garnet  
534 xenocrysts reveal a wide range of  $\Delta\log f_{\text{O}_2}$  values between FMQ-4.5 and FMQ-2.6 ( $\pm 0.9$ ), firmly  
535 within the well-studied Kaapvaal lithospheric mantle array. At mid-lithospheric depths beneath  
536 the Dharwar craton, redox compositions of the garnet xenocrysts correlate with geochemical  
537 proxies for melt-rock interactions, which provides evidence for the operation of oxidative mantle  
538 metasomatism that was likely diamond-destructive. Strong redox variability at relatively confined  
539 SCLM intervals would promote stability of diverse volatile-rich metasomatic mineral assemblages  
540 (e.g., roles of carbonates versus phlogopite and amphibole), which helps to explain the  
541 spatiotemporal association of ca. 1.1 Ga kimberlites, lamproites, orangeites and ultramafic  
542 lamprophyres in southern India.

543

## 544 **Acknowledgments**

545 AMS and ST acknowledge financial support from CIMERA and the UJ Faculty of Science for the  
546 research presented here. The research presented in this paper was also supported by funds provided  
547 to FV under the South African Department of Science and Innovation Research Chairs Initiative

548 (SARChI), as administered by the National Research Foundation (grant number 64779). The  
549 RESOLUTION laser instrumentation at the University of Johannesburg was funded by NRF-NEP  
550 grant #93208, and its up-keeping is supported by DSI-NRF CIMERA. We warmly thank Christian  
551 Reinke for assisting with the EPMA data collection at UJ. Bill Griffin is thanked for his guidance  
552 in modeling the Mg-numbers of ‘ghost’ olivine in equilibrium with peridotitic garnet xenocrysts.  
553 [Sonja Aulbach is thanked for the interesting discussions.](#) We are grateful to Vincenzo Stagno and  
554 Katie Smart for their helpful comments on this manuscript. Othmar Müntener is gratefully  
555 acknowledged for consummate editorial handling.

## 557 **References**

- 558 Ai Y (1994) A revision of the garnet-clinopyroxene  $\text{Fe}^{2+}$ -Mg exchange geothermometer.  
559 *Contrib Mineral Petrol*, 115:467–473
- 560 Aulbach S, Stachel T (2022) Evidence for oxygen-conserving diamond formation in redox-  
561 buffered subducted oceanic crust sampled as eclogite. *Nature Commun* 13:1924
- 562 Aulbach S, Jacob DE (2016) Major- and trace-elements in cratonic mantle eclogites and  
563 pyroxenites reveal heterogeneous sources and metamorphic processing of low-pressure  
564 protoliths. *Lithos* 262:586–605
- 565 Aulbach S, Viljoen KS (2015) Eclogite xenoliths from the Lace kimberlite, Kaapvaal craton:  
566 From convecting mantle source to palaeo-ocean floor and back. *Earth Planet Sci Lett* 431:274–  
567 286
- 568 Aulbach S, Griffin WL, Pearson NJ, O’Reilly SY (2013) Nature and timing of metasomatism in  
569 the stratified mantle lithosphere beneath the central Slave craton (Canada). *Chem Geol*  
570 352:153–169
- 571 Aulbach S, Griffin WL, Pearson NJ, O’Reilly SY, Doyle BJ (2007) Lithosphere formation in the  
572 Central Slave Craton (Canada): plume accretion or lithosphere accretion. *Contrib Mineral Petrol*  
573 154:409–428
- 574 Aulbach S, Sun J, Tappe S, Höfer HE, Gerdes A (2017) Volatile-rich metasomatism in the  
575 cratonic mantle beneath SW Greenland: Link to kimberlites and mid-lithospheric  
576 discontinuities. *J Petrol* 58(12):2311–2338

577 Aulbach S, Woodland AB, Stagno V, Korsakov AV, Mikhailenko D, Golovin A (2022) Fe<sup>3+</sup>  
578 Distribution and Fe<sup>3+</sup>/ΣFe-Oxygen Fugacity Variations in Kimberlite-Borne Eclogite Xenoliths,  
579 with Comments on Clinopyroxene-Garnet Oxy-Thermobarometry. *J Petrol* 63(8): egac076

580 Aulbach S, Woodland AB, Stern RA, Vasilyev P, Heaman LM, Viljoen KS (2019) Evidence for  
581 a dominantly reducing Archean ambient mantle from two redox proxies, and low oxygen  
582 fugacity of deeply subducted oceanic crust. *Sci Reports*, 9(1):1–11

583 Babu EVSSK, Griffin WL, Panda S, O'Reilly SY (2008) Eclogite xenoliths from the kimberlites  
584 of the Eastern Dharwar Craton, south India: material representing ancient crust of the Western  
585 Dharwar Craton? 9th International Kimberlite Conference, Frankfurt, Extended Abstract 9IKC-  
586 A-00161

587 Ballhaus C, Berry RF, Green DH (1991) High pressure experimental calibration of the olivine-  
588 orthopyroxene-spinel oxygen geobarometer: implications for the oxidation state of the upper  
589 mantle. *Contrib Miner Petrol* 107:27–40

590 Barth MG, Rudnick RL, Horn I, McDonough WF, Spicuzza M, Valley JR, Haggerty SE (2001)  
591 Geochemistry of xenolithic eclogites from West Africa: Part I. A link between low MgO  
592 eclogites and Archean crust formation. *Geochim Cosmochim Acta* 65:1499–1527

593 Barth MG, Rudnick RL, Horn I, McDonough WF, Spicuzza M, Valley JR, Haggerty SE (2002)  
594 Geochemistry of xenolithic eclogites from West Africa: Part II. Origins of the high MgO  
595 eclogites. *Geochim Cosmochim Acta* 66, 4325–4345

596 Beyer C, Frost DJ, Miyajima N (2015) Experimental calibration of a garnet–clinopyroxene  
597 geobarometer for mantle eclogites. *Contrib Mineral Petrol* 169(2)

598 Brey GP, Kohler T (1990) Geothermobarometry in four-phase lherzolites II. New  
599 thermobarometers, and practical assessment of existing thermometers. *J Petrol* 31:1353–1378

600 Burness S, Smart KA, Tappe S, Stevens G, Woodland AB, Cano E (2020) Sulphur-rich mantle  
601 metasomatism of Kaapvaal craton eclogites and its role in redox-controlled platinum group  
602 element mobility. *Chem Geol* 542:119476

603 Canil D (1999) The Ni-in-garnet geothermometer: Calibration at natural abundances. *Contrib*  
604 *Mineral Petrol* 136(3):240–246

605 Chadwick B, Vasudev VN, Hegde GV (2000) The Dharwar craton, southern India, interpreted  
606 as the result of Late Archean oblique convergence. *Precambri Res* 99:91–111

607 Chatterjee A, Chalapathi Rao N, Pandey R, Pandey A (2023) Mantle transition zone-derived  
608 eclogite xenolith entrained in a diamondiferous Mesoproterozoic (~1.1 Ga) kimberlite from the  
609 Eastern Dharwar Craton, India: Evidence from a coesite, K-omphacite, and majoritic garnet  
610 assemblage. *Geol Mag* 1–14

611 Creighton S, Stachel T, Eichenberg D, Luth RW (2010) Oxidation state of the lithospheric  
612 mantle beneath Diavik diamond mine, central Slave craton, NWT, Canada. *Contrib Mineral*  
613 *Petrol* 159:645–657

614 Creighton S, Stachel T, Matveev S, Höfer H, McCammon C, Luth RW (2009) Oxidation of the  
615 Kaapvaal lithospheric mantle driven by metasomatism. *Contrib Mineral Petrol* 157, 491–504

616 Dalton H, Giuliani A, O'Brien H, Phillips D, Hergt J, Maas R (2019) Petrogenesis of a hybrid  
617 cluster of evolved kimberlites and ultramafic lamprophyres in the Kuusamo area, Finland. *J Pet*  
618 60, 2025–2050

619 Day HW (2012) A revised diamond-graphite transition curve. *American Mineralogist*, 97(1),  
620 52–62

621 Deer WA, Howie FRS, Zussman J (2013) *An Introduction to the Rock-Forming Minerals*.  
622 Mineralogical Society of Great Britain and Ireland, doi:10.1180/DHZ

623 Dongre AN, Jacob DE, Stern RA (2015) Subduction related origin of eclogite xenoliths from the  
624 Wajrakarur kimberlite field, Eastern Dharwar craton, Southern India: Constraints from  
625 petrology and geochemistry. *Geochim Cosmochim Acta* 166:165–188

626 Ellis DJ, Green DH (1979) An experimental study of the effect of Ca upon garnet clinopyroxene  
627 Fe–Mg exchange equilibria. *Contrib Mineral Petrol* 71:13–22

628 Fedortchouk Y, Liebske C, McCammon C (2019) Diamond destruction and growth during  
629 mantle metasomatism: an experimental study of diamond resorption features. *Earth Planet Sci*  
630 *Lett*, 506, 493–506

631 Foley SF (2011) A reappraisal of redox melting in the Earth's mantle as a function of tectonic  
632 setting and time. *J Pet* 52, 1363–1391

633 Foley SF, Taylor WR, Green DH (1986) The role of fluorine and oxygen fugacity in the genesis  
634 of the ultrapotassic rocks. *Contrib Mineral Petrol* 94, 183–192

635 Ganguly J, Bhattacharya PK (1987) Xenoliths in Proterozoic Kimberlites from Southern India:  
636 petrology and Geophysical Implications. In: Nixon, P. H. (ed.) *Mantle Xenoliths*. John Wiley  
637 and Sons, pp 249–265

638 Ganguly J, Cheng W, Tirone M (1996) Thermodynamics of aluminosilicate garnet solid  
639 solution: new experimental data, an optimized model, and thermometric applications. *Contrib*  
640 *Mineral Petrol* 126:137–151

641 Garber JM, Maurya S, Hernandez JA, Duncan MS, Zeng L, Zhang HL, Faul U, McCammon C,  
642 Montagner JP, Moresi L, Romanowicz BA, Rudnick RL, Stixrude L (2018) Multidisciplinary  
643 Constraints on the Abundance of Diamond and Eclogite in the Cratonic Lithosphere. *Geochem*  
644 *Geophys Geosys* 19(7):2062–2086

645 Gaul OF, Griffin WL, O'Reilly SY, Pearson NJ (2000) Mapping olivine composition in the  
646 lithospheric mantle. *Earth Planet Sci Lett* 182(3–4):223–235

647 Griffin WL, Doyle BJ, Ryan CG, Pearson NJ, Suzanne YO, Davies R, Kivi K, Van Achterbergh  
648 E, Natapov LM (1999). Layered mantle lithosphere in the Lac de Gras area, Slave craton:  
649 composition, structure and origin. *J Petrol* 40:705–727

650 Griffin WL, Kobussen AF, Babu EVSSK, O'Reilly SY, Norris R, Sengupta P (2009) A  
651 translithospheric suture in the vanished 1-Ga lithospheric root of South India: evidence from  
652 contrasting lithosphere sections in the Dharwar Craton. *Lithos* 112:1109–1119

653 Grütter HS, Gurney JJ, Menzies AH, Winter F (2004) An updated classification scheme for  
654 mantle-derived garnet, for use by diamond explorers. *Lithos* 77:841–857

655 Gurney JJ, Moore RO (1993) Geochemical correlations between kimberlitic indicator minerals  
656 and diamonds. In: *Diamonds: Exploration, Sampling and Evaluation. Proceedings of PDAC*  
657 *Short Course*, 147:149–171

658 Hanger BJ, Yaxley GM, Berry AJ, Kamenetsky VS (2015) Relationships between oxygen  
659 fugacity and metasomatism in the Kaapvaal subcratonic mantle, represented by garnet peridotite  
660 xenoliths in the Wesselton kimberlite, South Africa. *Lithos* 212, 443–452

661 Hardman MF, Stachel T, Pearson DG, Cano EJ, Stern RA, Sharp ZD (2021) Characterising the  
662 Distinct Crustal Protoliths of Roberts Victor Type I and II Eclogites. *J Petrol* 62(12):1–19

663 Harley SL (1984) An experimental study of the partitioning of Fe and Mg between garnet and  
664 orthopyroxene. *Contrib Mineral Petrol* 86:359–373

665 Höfer HE, Brey GP (2007) The iron oxidation state of garnet by electron microprobe: its  
666 determination with the flank method combined with major-element analysis. *Am Mineral*  
667 92:873–885

668 Höfer HE, Brey GP, Schulz-Dobrick B, Oberhänsli R (1994) The determination of the oxidation  
669 state of iron by the electron microprobe. *Eur J Mineral* 6:407–418

670 Jacob DE (2004) Nature and origin of eclogite xenoliths from kimberlites. *Lithos*, 77:295–316

671 Jacob DE, Bizimis M, Salters VJM (2005) Lu-Hf and geochemical systematics of recycled  
672 ancient oceanic crust: Evidence from Roberts Victor eclogites. *Contributions to Mineral Petrol*  
673 148, 707–720

674 Jacob DE, Foley SF (1999) Evidence for Archean ocean crust with low high field strength  
675 element signature from diamondiferous eclogite xenolith. *Lithos* 48:317–336

676 Jacob DE, Viljoen KS, Grassineau NV (2009) Eclogite xenoliths from Kimberley, South Africa  
677 - A case study of mantle metasomatism in eclogites. *Lithos* 112:1002–1013

678 Jochum KP, Weis U, Schwager B, Stoll B, Wilson SA, Haug GH, Andreae MO, Enzweiler J  
679 (2016) Reference values following ISO guidelines for frequently requested rock reference  
680 materials. *Geostanda Geoana Res* 40, 333–350

681 Kargin AV, Sazonova LV, Nosova AA, Tretyachenko VV (2016) Composition of garnet and  
682 clinopyroxene in peridotite xenoliths from the Grib kimberlite pipe, Arkhangelsk diamond  
683 province, Russia: Evidence for mantle metasomatism associated with kimberlite melts. *Lithos*  
684 262:442–455

685 Kopylova MG, Beausoleil Y, Goncharov A, Burgess J, Strand P (2016) Spatial distribution of  
686 eclogite in the Slave cratonic mantle: The role of subduction. *Tectonophy* 672–673:87–103

687 Kopylova MG, Russell JK, Cookenboo H (1999) Petrology of peridotite and pyroxenite  
688 xenoliths from the Jericho kimberlite: implications for the thermal state of the mantle beneath  
689 the Slave craton, Northern Canada. *J Petrol* 40:79–104

690 Krogh Ravna E (2000) The garnet-clinopyroxene Fe<sup>2+</sup>–Mg geothermometer: an updated  
691 calibration. *Journal of Metamorphic Geology* 18, 211–219

692 Krogh, EJ (1988) The garnet-clinopyroxene Fe–Mg geothermometer – a reinterpretation of  
693 existing experimental data. *Contrib Mineral Petrol* 99:44–48

694 Luth RW, Virgo D, Boyd FR, Wood BJ (1990) Ferric iron in mantle derived garnets:  
695 implications for thermobarometry and for the oxidation state of the mantle. *Contrib Mineral*  
696 *Petrol* 104:56–72

697 McCammon CA, Griffin WL, Shee SR, O’Neill HSC (2001) Oxidation during metasomatism in  
698 ultramafic xenoliths from the Wesselton kimberlite, South Africa: implications for the survival  
699 of diamond. *Contrib Mineral Petrol* 141:287–296

700 McCandless T, Gurney J (1989) Sodium in garnet and potassium in clinopyroxene: criteria for  
701 classifying mantle eclogites. In: Ross J, Jaques AL, Ferguson J, Green DH, O’Reilly SY,  
702 Danchin RV, Janse AJA (eds) *Kimberlite and related rocks*. Special publication—Geological  
703 Society of Australia, Perth

704 McGuire AV, Francis CA, Dyar MD (1992) Mineral standards for microprobe analysis of  
705 oxygen. *Am Mineral*, 77, 1087–1091

706 Mikhailenko DS, Stagno V, Korsakov AV, Andreozzi GB, Marras G, Cerantola V, Malygina  
707 EV (2020) Redox state determination of eclogite xenoliths from Udachnaya kimberlite pipe  
708 (Siberian craton), with some implications for the graphite/diamond formation. *Contrib Mineral*  
709 *Petrol* 175(11):1–17

710 Mukherjee A, Tiwari P, Verma CB, Babu EVSSK, Sarathi JP (2021) Native Gold and Au-Pt  
711 Alloy in Eclogite Xenoliths of Kalyandurg KL-2 Kimberlite, Anantapur District, South India. *J*  
712 *Geol Soc India* 97(6):567–570

- 713 Nakamura D (2009) A new formulation of garnet–clinopyroxene geothermometer based on  
714 accumulation and statistical analysis of a large experimental data set. *Journal of Metamorphic*  
715 *Geology* 27(7):495–508
- 716 Neelakantam S (2001) Exploration for diamonds in southern India. *Geol Surv India Spec Publ*  
717 58:521–555
- 718 Nimis P (2022) Pressure and Temperature Data for Diamonds. *Rev Mineral Geochem*  
719 88(1):533–565
- 720 Nimis P, Grütter H (2010) Internally consistent geothermometers for garnet peridotites and  
721 pyroxenites. *Contrib Mineral Petrol* 159(3):411–427
- 722 [Nimis P, Taylor WR \(2000\) Single clinopyroxene thermobarometry for garnet peridotites. Part](#)  
723 [I. Calibration and testing of a Cr-in-Cpx barometer and an enstatite-in-Cpx thermometer.](#)  
724 [Contrib Mineral Petrol 139:541–554](#)
- 725 Nixon PH, Davies GR (1987) Mantle xenolith perspectives. In: Nixon PH (ed) *Mantle xenoliths*.  
726 Wiley, New York, pp 742–756
- 727 Nowell GM, Pearson DG, Bell DR, Carlson RW, Smith CB, Kempton PD, Noble SR (2004) Hf  
728 isotope systematics of kimberlites and their megacrysts: New constraints on their source  
729 regions. *J Petrol* 45(8):1583–1612
- 730 O’Neill HSC, Wood BJ (1979) An experimental study of Fe-Mg partitioning between garnet  
731 and olivine and its calibration as a geothermometer. *Contrib Mineral Petrol* 70:59–70
- 732 Pandey A, Chalapathi Rao NV (2020) Supercontinent transition as a trigger for ~1.1 Gyr  
733 diamondiferous kimberlites and related magmatism in India. *Lithos* 370–371
- 734 Patel SC, Ravi S, Anil Kumar Y, Naik A, Thakur SS, Pati JK, Nayak SS (2009) Mafic xenoliths  
735 in proterozoic kimberlites from Eastern Dharwar Craton, India: mineralogy and P–T regime. *J*  
736 *Asian Earth Sci* 34:336–346
- 737 Patel SC, Ravi S, Thakur SS, Rao TK, Subbarao KV (2006) Eclogite xenoliths from Wajrakarur  
738 kimberlites, southern India. *Mineral Petrol* 88(1–2):363–380
- 739 Pattnaik J, Ghosh S, Dongre A (2020) Plume activity and carbonated silicate melt  
740 metasomatism in Dharwar cratonic lithosphere: Evidence from peridotite xenoliths in  
741 Wajrakarur kimberlites. *Lithos* 376–377
- 742 Powell R (1985) Regression diagnostics and robust regression in geothermometer/ geobarometer  
743 calibration: the garnet-clinopyroxene geothermometer revisited. *J Metamor Geol* 3:231–243
- 744 Rao KRP, Nayak SS, Reddy TAK, Dhakate MV, Chowdary VS, Ravi S, Suresh G, Rao KS B  
745 (2001) Geology, petrology, geochemistry and mineral chemistry of new kimberlite finds in the

746 Wajrakarur Kimberlite Field, Anantapur district, Andhra Pradesh. Geological Survey of India  
747 Special Publication 58:593–602

748 Rankenburg K, Lassiter JC, Brey GP (2004) Origin of megacrysts in volcanic rocks of the  
749 Cameroon volcanic chain—constraints on magma genesis and crustal contamination. *Contrib*  
750 *Mineral Petrol*, 147, 129–144

751 Ravi S, Sufija MV, Patel SC, Sheikh JM, Sridhar M, Kaminsky FV, Khachatryan GK, Nayak  
752 SS, Bhaskara Rao KS (2013) Diamond potential of the Eastern Dharwar Craton, Southern India,  
753 and a reconnaissance study of physical and infrared characteristics of the diamonds. In: Pearson,  
754 DG (eds) *Proceedings of 10th International Kimberlite Conference. Special Issue J Geol Soc*  
755 *India* 1:335–348

756 Ryan CG, Griffin WL, Pearson NJ (1996) Garnet geotherms: pressure-temperature data from  
757 Cr-pyrope garnet xenocrysts in volcanic rocks. *J Geophys Res: Solid Earth* 101:5611–5625

758 Rzehak LJ, Rohrbach A, Vollmer C, Höfer HE, Berndt J, Klemme S (2020) Ferric-ferrous iron  
759 ratios of experimental majoritic garnet and clinopyroxene as a function of oxygen fugacity.  
760 *American Mineralogist: J Earth Planet Mater* 105(12):1866–1874

761 Sarkar S, Giuliani A, Ghosh S, Phillips D (2021) Petrogenesis of coeval lamproites and  
762 kimberlites from the Wajrakarur field, Southern India: New insights from olivine compositions.  
763 *Lithos* 406–407:106524

764 Sastry CA, Rao GR, Prasad GJS, Reddy VA (2005) Electron probe microanalysis of indicator  
765 minerals from kimberlites of Andhra Pradesh and Karnataka – basic data. *Geol Surve India*  
766 *Bullet* 6:282

767 Schulze DJ (1989) Constraints on the abundance of eclogite in the upper mantle. *J Geophys Res*  
768 94:4205–4212

769 Shaikh AM, Patel SC, Ravi S, Behera D, Pruseth KL (2017) Mineralogy of the TK1 and TK4  
770 ‘kimberlites’ in the Timmasamudram cluster, Wajrakarur Kimberlite Field, India: Implications  
771 for lamproite magmatism in a field of kimberlites and ultramafic lamprophyres. *Chem Geol*  
772 455:208–230

773 Shaikh AM, Kumar SP, Patel SC, Thakur SS, Ravi S, Behera D (2018) The P3 kimberlite and  
774 P4 lamproite, Wajrakarur kimberlite field, India: mineralogy, and major and minor element  
775 compositions of olivines as records of their phenocrystic vs xenocrystic origin. *Mineral Petrol*  
776 112:609–624

777 Shaikh AM, Patel SC, Bussweiler Y, Kumar SP, Tappe S, Ravi S, Mainkar D (2019) Olivine  
778 trace element compositions in diamondiferous lamproites from India: Proxies for magma origins  
779 and the nature of the lithospheric mantle beneath the Bastar and Dharwar cratons. *Lithos* 324–  
780 325:501–518

781 Shaikh AM, Tappe S, Bussweiler Y, Patel SC, Ravi S, Bolhar R, Viljoen F (2020)  
782 Clinopyroxene and Garnet Mantle Cargo in Kimberlites as Probes of Dharwar Craton  
783 Architecture and Geotherms, with Implications for Post-1·1 Ga Lithosphere Thinning Events  
784 Beneath Southern India. *J Petrol* 61(9)

785 Smart KA, Heaman LM, Chacko T, Simonetti A, Kopylova M, Mah D, Daniels D (2009) The  
786 origin of high-MgO diamond eclogites from the Jericho kimberlite, Canada. *Earth Planet Sci*  
787 *Lett* 284, 527–537

788 Smart KA, Tappe S, Simonetti A, Simonetti SS, Woodland AB, Harris C (2017) Tectonic  
789 significance and redox state of Paleoproterozoic eclogite and pyroxenite components in the  
790 Slave cratonic mantle lithosphere, Voyageur kimberlite, Arctic Canada. *Chem Geol* 455:98–119

791 Smart KA, Tappe S, Stern RA, Webb SJ, Ashwal LD (2016) Early Archaean tectonics and  
792 mantle redox recorded in Witwatersrand diamonds. *Nature Geo* 9, 255–259

793 Smart KA, Tappe S, Woodland AB, Greyling DR, Harris C, Gussone N (2021a) Constraints on  
794 Archean crust recycling and the origin of mantle redox variability from the  $\delta^{44/40}\text{Ca} - \delta^{18}\text{O} - f\text{O}_2$   
795 signatures of cratonic eclogites. *Earth Planet Sci Lett* 556

796 Smart KA, Tappe S, Woodland AB, Harris C, Corcoran L, Simonetti A (2021b) Metasomatized  
797 eclogite xenoliths from the central Kaapvaal craton as probes of a seismic mid-lithospheric  
798 discontinuity. *Chem Geol* 578, 120286

799 Stachel T, Luth RW (2015) Diamond formation - Where, when and how? *Lithos* 220–223: 200–  
800 220

801 Stagno V (2019) Carbon, carbides, carbonates and carbonatitic melts in the Earth's interior *J*  
802 *Geol Soc* 176:375

803 Stagno V, Frost DJ, McCammon CA, Mohseni H, Fei Y (2015) The oxygen fugacity at which  
804 graphite or diamond forms from carbonate-bearing melts in eclogitic rocks. *Contrib Mineral*  
805 *Petrol* 169:16

806 Stagno V, Ojwang DO, McCammon CA, Frost DJ (2013) The oxidation state of the mantle and  
807 the extraction of carbon from Earth's interior. *Nature* 493:84–88

808 Sun SS, McDonough WF (1989) Chemical and isotopic systematics of oceanic basalts:  
809 implications for mantle composition and processes. *Geol Soc Lond Spec Publ* 42:313–345

810 Tappe S, Ngwenya NS, Stracke A, Romer RL, Glodny J, Schmitt AK (2023) Plume–lithosphere  
811 interactions and LIP-triggered climate crises constrained by the origin of Karoo lamproites.  
812 *Geochim Cosmo Acta* 350, 87–105

813 Tappe S, Foley SF, Kjarsgaard BA, Romer RL, Heaman LM, Stracke A, Jenner GA (2008)  
814 Between carbonatite and lamproite-Diamondiferous Torngat ultramafic lamprophyres formed by

815 carbonate-fluxed melting of cratonic MARID-type metasomes. *Geochim Cosmo Acta*  
816 72(13):3258–3286

817 Tappe S, Pearson DG, Nowell G, Nielsen T, Milstead P, Muehlenbachs K (2011a) A fresh  
818 isotopic look at Greenland kimberlites: Cratonic mantle lithosphere imprint on deep source  
819 signal. *Earth Planet Sci Lett* 305(1-2):235–248

820 Tappe S, Smart KA, Pearson DG, Steinfeld A, Simonetti A (2011b) Craton formation in Late  
821 Archean subduction zones revealed by first Greenland eclogites. *Geology*, 39(12):1103–1106

822 Tappe S, Smart K, Torsvik T, Massuyeau M, de Wit M (2018) Geodynamics of kimberlites on a  
823 cooling Earth: Clues to plate tectonic evolution and deep volatile cycles. *Earth Planet Sci Lett*  
824 484:1–14

825 Tappe S, Massuyeau M, Smart KA, Woodland AB, Gussone N, Milne S, Stracke A (2021)  
826 Sheared Peridotite and Megacryst Formation Beneath the Kaapvaal Craton: a Snapshot of  
827 Tectonomagmatic Processes across the Lithosphere – Asthenosphere Transition. *J Petrol* 62(8),  
828 1–39

829 Taylor LA, Neal CR (1989) Eclogites with oceanic crustal and mantle signatures from the  
830 Bellsbank kimberlite, South Africa, Part I: Mineralogy, Petrography and whole rock chemistry.  
831 *J Geol* 551–567

832 Viljoen KS, Smith CB, Sharp ZD (1996) Stable and radiogenic isotope study of eclogite  
833 xenoliths from the Orapa kimberlite, Botswana. *Chem Geol* 131:235–255

834 Wang J, Xiong X, Takahashi E, Zhang L, Li L, Liu X (2019) Oxidation State of Arc Mantle  
835 Revealed by Partitioning of V, Sc, and Ti Between Mantle Minerals and Basaltic Melts. *J*  
836 *Geophys Res Solid Earth* 124(5):4617–4638

837 Woodland AB, Koch M (2003) Variation in oxygen fugacity with depth in the upper mantle  
838 beneath the Kaapvaal craton, Southern Africa. *Earth Planet Sci Lett* 214(1):295–310

839 Yaxley GM, Berry AJ, Rosenthal A, Woodland AB, Paterson D (2017) Redox preconditioning  
840 deep cratonic lithosphere for kimberlite genesis: evidence from the central Slave Craton. *Sci*  
841 *Rep* 7:30

842

#### 843 **Figure Captions**

844 **Fig. 1.** Geological map of Wajrakarur Kimberlite Field (WKF) modified after Shaikh et al. (2017).

845 This study deals with samples from the KL2, P9, and P10 kimberlite intrusions (highlighted by  
846 yellow-filled circles).

847

848 **Fig. 2.** Scanned thin section images of KL2 eclogite nodules.

849

850 **Fig. 3.** BSE images of KL2 eclogite nodules showing mineral grain relations and the extensive  
851 alteration of primary and matrix minerals. (a) Highly fractured garnet in sample KL2A1 showing  
852 alteration to hydro-garnet along margins. (b) Sample KL2B1 shows garnet altered to carbonate  
853 and chlorite along fractures and no preservation of omphacite and kyanite. (c) Highly fractured  
854 and altered omphacite in sample KL2A1. (d) Kyanite blades in sample KL2C3, with inclusions of  
855 garnet and omphacite, partially altered to celsian. (e) Kyanite blade in sample KL2G1 with  
856 inclusions of garnet and omphacite. (f) Interlocked kyanite blades in sample KL2F2 with an  
857 omphacite inclusion.

858

859 **Fig. 4.** BSE images of KL2 eclogite nodules with corundum associated with kyanite (a) and a rutile  
860 bleb (b).

861

862 **Fig. 5.** Major and trace element (REE) plots for garnet (a, b, c) and clinopyroxene (b, d) from KL2  
863 eclogites. The fields in figure (a) are after Aulbach and Jacob (2016) and in (b) after McCandless  
864 and Gurney (1989). The A, B, and C fields in the inset figure are after Taylor and Neal (1989).

865

866 **Fig. 6.** Cr<sub>2</sub>O<sub>3</sub> versus CaO wt.% plot (a) and chondrite normalized REE plot (b; after (Sun and  
867 McDonough, 1989) for garnet xenocrysts from P9 and P10 intrusions of the WKF.

868

869 **Fig. 7.** Reconstructed bulk-rock composition diagrams for classifying KL2 eclogite nodules. Fields  
870 in figures (a) and (b) are after Aulbach and Jacob (2016), and primitive mantle normalization in  
871 (c) is after (Sun and McDonough, 1989). Published KL2 eclogite data are from Dongre et al.  
872 (2015). Symbol sizes in (a) and (b) are larger than the  $2\sigma$  uncertainties.

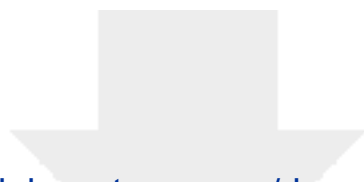
874 **Fig. 8.** Trace element variations diagrams based on reconstructed bulk-rock compositions for  
875 eclogite nodules. Note that reconstructed bulk-rock compositions indicate  $fO_2$  values below FMQ-  
876 2. Figures (a) Ti vs. Vi/Ti\*100, (b) Ce/Yb vs. Lu/Gd, and (c) MgO vs. V/Sc are after Wang et al.  
877 (2019) and Aulbach and Viljoen (2015). Symbol sizes in (a) and (b) are larger than the  $2\sigma$   
878 uncertainties.

880 **Fig. 9.** Projections of equilibration temperatures calculated for KL2 eclogite nodules (a; after  
881 Krogh, 1988) and P9-P10 garnet xenocrysts (b; after Canil, 1999). Published KL2 data from Patel  
882 et al. (2006) and Dongre et al. (2015). The conductive model geotherm (after Hasterok and  
883 Chapman, 2011) for the Wajrakarur lithosphere is from Shaikh et al. (2020). The diamond-graphite  
884 transition is after Day et al. (2012).

885  
886 **Fig. 10.**  $\Delta\log fO_2$  (FMQ) values calculated for KL2 eclogitic garnets (after Stagno et al., 2015) and  
887 P9 and P10 peridotitic garnet xenocrysts (after Stagno et al., 2013) plotted against the estimated  
888 pressure. The field for Kaapvaal peridotites is after Woodland and Koch (2003) and Creighton et  
889 al. (2009), enriched peridotites from Slave craton after Yaxley et al. (2017) and graphite-diamond-  
890 carbonate melt transition lines after Stagno et al. (2015). Updated Kaapvaal data (small open  
891 circles) are after Tappe et al. (2021).

892  
893 **Fig. 11.**  $\Delta\log f_{O_2}$  (FMQ) versus MgO and CaO (in wt%) for KL2 eclogitic garnets from Wajrakarur  
894 kimberlites.

895  
896 **Fig. 12.**  $Fe^{3+}/\Sigma Fe$  ratios plotted against ~~respective~~ TiO<sub>2</sub> (a), Y (b), Zr (c), and V (d) ~~for in~~ peridotitic  
897 garnet xenocrysts from the P9 and P10 kimberlite bodies at intrusions of the Wajrakarur. Kaapvaal  
898 craton xenolith data are taken from Creighton et al. (2009).



Click here to access/download

**Electronic supplementary material**  
Supp. Table 1.xlsx

